Spring 2007

The Computation of Exact Green's Functions in Acoustic Analogy By a Spectral Collocation Boundary Element Method

Andrea D. Jones
Old Dominion University

Recommended Citation

Jones, Andrea D.. "The Computation of Exact Green's Functions in Acoustic Analogy By a Spectral Collocation Boundary Element Method" (2007). Doctor of Philosophy (PhD), dissertation, Mathematics and Statistics, Old Dominion University, DOI: 10.25777/cnsp-7b74
https://digitalcommons.odu.edu/mathstat_etds/27

THE COMPUTATION OF EXACT GREEN'S FUNCTIONS IN ACOUSTIC ANALOGY BY A SPECTRAL COLLOCATION BOUNDARY ELEMENT METHOD

by

Andrea D. Jones
B.S. December 1996, Virginia Polytechnic Institute & State University
M.S. December 2006, Old Dominion University

A Dissertation Submitted to the Faculty of
Old Dominion University in Partial Fulfillment of the
Requirement for the Degree of

DOCTOR OF PHILOSOPHY

COMPUTATIONAL AND APPLIED MATHEMATICS

OLD DOMINION UNIVERSITY
May 2007

Approved by:

Fang Q. Hu (Director)

Mehdi R. Khorrami (Member)

Hideaki Kaneko (Member)

Richard Noren (Member)

Ruhai Zhou (Member)

ABSTRACT

THE COMPUTATION OF EXACT GREEN'S FUNCTIONS IN ACOUSTIC ANALOGY BY A SPECTRAL COLLOCATION BOUNDARY ELEMENT METHOD

Andrea D. Jones
Old Dominion University, 2007
Director: Dr. Fang Q. Hu

Aircraft airframe noise pollution resulting from the take-off and landing of airplanes is a growing concern. Because of advances in numerical analysis and computer technology, most of the current noise prediction methods are computationally efficient. However, the ability to effectively apply an approach to complex airframe geometries continues to challenge researchers. The objective of this research is to develop and analyze a robust noise prediction method for dealing with geometrical modifications. This new approach for determining sound pressure involves computing exact, or tailored, Green's functions for use in acoustic analogy. The effects of sound propagation and scattering by solid surfaces are included in the exact Green's function, which is tailored for a specific geometry. The exact Green's function is computed using a spectral collocation boundary element method that can easily accommodate complex geometries. A frequency-domain spectral collocation method is applied to both smooth and non-smooth boundaries, resulting in exponential convergence on smooth boundaries. Solution singularities at boundary corners are dealt with via an exponential grading element refinement. With proper refinement, exponential convergence is also obtained for non-smooth boundaries. The formulation and application of a three-dimensional time-domain BEM allows computation of exact Green's functions for all frequencies in a single calculation. Long-time instabilities in the time-marching numerical solutions are corrected via a Burton-Miller modified integral equation. Two examples provide validation of the acoustic analogy involving the exact Green's function.

ACKNOWLEDGMENTS

First, I would like to thank Professor Fang Q. Hu for offering me this amazing research opportunity. His wisdom, patience and encouragement have helped me maintain my sanity through countless hours of formulating, programming and compiling results. I am also grateful to Dr. Hu for involving me in publications and conferences.

I would like to thank my committee members for taking the time to review my work and offering suggestions for improvement. I enjoyed attending classes taught by Dr. Fang Hu, Dr. Richard Noren and Dr. Ruhai Zhou. I thank Dr. Hideaki Kaneko for his guidance as my Graduate Program Director. I also thank Dr. Mehdi Khorrami for making the trip from NASA Langley to ODU for each of my presentations.

The first three years of this research was supported by a grant from NASA Langley Research Center. I would specifically like to thank NASA's Dr. Mehdi Khorrami for overseeing the project and providing helpful comments and suggestions.

Funding for the final year of this research came in the form of an ODU College of Sciences Dissertation Fellowship. I sincerely thank Professor Hideaki Kaneko for encouraging me to apply for the fellowship. As a bonus, I will be attending a conference in Rome, Italy, to present my research after graduation, which would not have been possible without this award.

I thank my family and friends for their love and support over the past five years. A special thank you goes to my parents, Joseph and Janny DiPaola, and my sister, Jaclyn DiPaola, for always believing in me. I also thank my true friends Brandy Blow and Lee Land for making sure I took time out for girls' nights.

Finally, I would like to express my eternal gratitude to my husband, Eric Jones, for supporting me through every step of this long journey. I am truly spoiled by you every day.

TABLE OF CONTENTS

CHAPTERS

APPENDICES

LIST OF TABLES

LIST OF FIGURES

CHAPTER I

INTRODUCTION

Noise pollution resulting from the take-off and landing of airplanes has been and continues to be a growing concern. This noise affects communities surrounding airports and will only worsen as the number of commercial flights increases. Presently, the noise generated by the propulsion system during landing has been effectively reduced such that it is of the same order of magnitude as the airframe noise [18]. Thus, devising a successful airframe noise prediction method has become the focus of many aircraft engineers.

Some characteristics of a good noise prediction method include: determining changes in the noise spectrum due to modifications in the geometry of the airframe, predicting noise levels for an observer in an arbitrary position, and designing a model that is computationally efficient when compared with current prediction methods [18]. Because of advances in numerical analysis and computer technology, most of the current approaches used to predict airframe noise are computationally efficient. However, the ability to effectively apply an approach to complex aircraft airframe geometries continues to challenge researchers. The primary objective of this thesis is to develop and analyze a robust noise prediction method for dealing with geometrical modifications.

Many published works contain analytical techniques for predicting acoustic radiation and scattering in the absence of a flow field [3, 4, 20]. However, only numerical methods can accurately predict airframe noise when flow is present [13]. Therefore, numerical simulations are quickly becoming an integral part of aeroacoustic research [26]. The most common method used in airframe noise prediction combines computational fluid dynamics with the theory of acoustic analogy using the Ffowcs Williams-Hawkings (FWH) equation [18, 19]. In the FWH equation, the far-field noise is expressed as the sum of surface integrals of unsteady pressure and a volume integral of turbulent sources using the free-space Green's function [19]. Numerical methods are used to evaluate the surface and volume integrals in the FWH equation to obtain the far-field sound pressure.

A new approach for determining sound pressure involves computing exact, or

---

This disertation follows the style of Engineering Analysis with Boundary Elements.

tailored, Green's functions for use in acoustic analogy. The exact Green's function satisfies the wall boundary conditions on all solid surfaces while also automatically satisfying the Sommerfeld radiation condition at infinity. Two advantages of using the exact Green's function are:

- The far-field pressure fluctuation can be expressed as a single volume integral over the sound-producing region. The elimination of the unsteady surface pressure integrals when using an exact Green's function over the free-space Green's function allows development of noise prediction strategies based on steady CFD calculations, which take less time to compute than unsteady CFD calculations.
- The effects of sound propagation to the far-field and scattering by solid surfaces are included in the exact Green's function, which is tailored for a specific geometry.

In this thesis, exact Green's functions will first be computed using a two-dimensional frequency-domain spectral collocation boundary element method, a mesh-free method that can easily accommodate complex geometries. Most commonly used boundary element methods limit the boundary elements to constant or linear functions. Because the spatial double divergence of the exact Green's function is needed for the acoustic analogy, constant and linear elements are not always sufficient, especially in flow regions close to the boundary. The spectral collocation method uses discontinuous boundary elements so that the order of the scheme can be increased without reformulation of the problem. To ensure spectral accuracy on smooth boundaries, Chebyshev polynomials will be used as basis functions, along with interior Gauss-Chebyshev collocation points. For problematic field points close to the boundary, the double divergence of the exact Green's function will be computed by direct differentiation and by finite difference schemes. A comparative study will determine the best method for calculating the double divergence.

As stated previously, one characteristic of a successful airframe noise prediction method is its ability to calculate changes in sound pressure due to modifications in geometry. Unfortunately, accurate airframe noise prediction is difficult for non-smooth boundaries because of solution singularities that occur in the vicinity of corners or edges. Two techniques for dealing with corner singularities will be implemented. First, an exponential grading element refinement strategy will be developed and applied to corner elements. Next, Sinc functions and corresponding collocation points will be used in place of Chebyshev polynomials on corner elements. The two revised techniques will then be compared with the unrefined spectral collocation method and with each other to determine their success in handling corner singularities.

Next, a time-domain BEM will be formulated for the computation of exact Green's functions for general three-dimensional surfaces that involves a March-On-Time (MOT) approach. Long-time stability problems will be discussed and overcome using a Burton-Miller formulation. Exact Green's functions at all frequencies will be obtained in a simple calculation through the Fast Fourier Transform (FFT) of the time-domain solution. The accuracy and efficiency of the time-domain BEM will be demonstrated by comparisons with known solutions.

In order to validate the acoustic analogy formulation involving the exact Green's function, two applications in sound prediction will be performed. First, the predicted sound field from acoustic analogy will be computed for a vortex passing over a circular cylinder. The results will then be compared with those of a direct numerical simulation. Second, the acoustic analogy will be used to compute the sound generated by a turbulent flow over a circular cylinder. The radiation pattern at the fundamental and first harmonic frequencies will be illustrated and compared with Lighthill's theory.

CHAPTER II

FORMULATION

II.1 ACOUSTIC ANALOGY AND EXACT GREEN'S FUNCTIONS

Acoustic analogy is used to model physical problems by predicting noise generated by unsteady flows without total knowledge of the flow behavior. Formulation of the acoustic analogy involves combining the conservation equations of fluid dynamics with a source term involving the Lighthill stress tensor in order to obtain a generalized wave equation.

II.1.1 Governing Equations

In tensor form, the conservation of mass and momentum equations are [34]

$$\frac{\partial \rho}{\partial t} + \frac{\partial}{\partial x_i}(\rho u_i) = 0 \tag{1}$$

$$\frac{\partial}{\partial t}(\rho u_i) + \frac{\partial}{\partial x_j}(\rho u_i u_j + p_{ij}) = 0 \tag{2}$$

where ρ is the fluid density, u_i is the velocity in the direction of x_i and p_{ij} is the compressive stress tensor. Equations (1) and (2) are the governing equations of sound propagation in an arbitrary continuous medium without external forces [28].

II.1.2 Lighthill's Theory

Sound waves are small disturbances in the pressure and density of a fluid. In basic acoustics, these disturbances are so small that the conservation equations of mass and momentum can be linearized. In 1952, Sir James Lighthill introduced an acoustic analogy that has become an integral part of present-day computational aeroacoustics [28]. Lighthill's acoustic theory draws an analogy between the full non-linear flow problem and the linear theory of classical acoustics. It assumes that the fluid contains only a finite region in which the flow is non-steady and fluctuating. Outside that region, the fluid is assumed to be uniform and at rest apart from small motions due to the sound waves of the unsteady flow [12, 28]. Taking the partial derivative with respect to t of equation (1) and the partial derivative with respect to x_i of equation

(2) and subtracting results in the following equation [12, 28]

$$\frac{\partial^2 \rho}{\partial t^2} - \frac{\partial^2}{\partial x_i \partial x_j} \left(\rho u_i u_j + p_{ij} \right) = 0 \tag{3}$$

Equation (3) can be written as,

$$\frac{\partial^2 \rho}{\partial t^2} - c_0^2 \frac{\partial^2 \rho}{\partial x_i^2} = \frac{\partial^2}{\partial x_i \partial x_j} \left(\rho u_i u_j + p_{ij} \right) - c_0^2 \frac{\partial^2 \rho}{\partial x_i^2}$$

which is a wave equation with a source term on the right-hand side. This source term can be combined to get

$$\frac{\partial^2 \rho}{\partial t^2} - c_0^2 \frac{\partial^2 \rho}{\partial x_i^2} = \frac{\partial^2}{\partial x_i \partial x_j} \left(\rho u_i u_j + p_{ij} - c_0^2 \rho \delta_{ij} \right) \equiv \frac{\partial^2 T_{ij}}{\partial x_i \partial x_j} \tag{4}$$

where c_0 is the speed of sound and T_{ij} is defined as the Lighthill stress tensor, so that

$$T_{ij} = \rho u_i u_j + p_{ij} - c_0^2 \rho \delta_{ij}$$

For a viscous Newtonian fluid, the compressive stress tensor is

$$p_{ij} = p \delta_{ij} - \tau_{ij}$$

where p is the pressure and τ_{ij} is the viscous stress tensor. The viscous stress term is due entirely to the existence of motion of the fluid, and is defined as

$$\tau_{ij} = 2\mu \left(e_{ij} - \frac{1}{3} e_{kk} \delta_{ij} \right)$$

where μ is the viscosity and e_{ij} is the rate-of-strain tensor,

$$e_{ij} = \frac{1}{2} \left[\frac{\partial u_i}{\partial x_j} - \frac{\partial u_j}{\partial x_i} \right]$$

The fluctuations in density and pressure can be defined by denoting

$$\rho' = \rho - \rho_0, \quad p' = p - p_0$$

where ρ_0 and p_0 are the constant mean values of density and pressure, respectively. These fluctuations can then be substituted into equation (4) to get

$$\frac{\partial^2 \rho'}{\partial t^2} - c_0^2 \frac{\partial^2 \rho'}{\partial x_i^2} = \frac{\partial^2}{\partial x_i \partial x_j} \left[\rho u_i u_j + (p - p_0) \delta_{ij} - c_0^2 (\rho - \rho_0) \delta_{ij} - \tau_{ij} \right] \tag{5}$$

In the theory of basic acoustics, it can be assumed that the fluid is Newtonian and all molecular relaxation and diffusion effects can be neglected. This implies that the entropy of any fluid element will be constant, i.e., the pressure is a function of density alone [12]. As a result, the pressure can be written as

$$p' = c_0^2 \rho' \tag{6}$$

Within the flow region, viscous contributions to T_{ij} are small and can be neglected. Therefore, equation (5) reduces to

$$\frac{\partial^2 \rho'}{\partial t^2} - c_0^2 \frac{\partial^2 \rho'}{\partial x_i^2} = \frac{\partial^2}{\partial x_i \partial x_j} (\rho u_i u_j)$$

The quantity $\rho u_i u_j$ is known as the Reynolds stress tensor. Since the typical flow Mach number related to aircraft airframe during take-off and landing is about 0.2 [19], the density, ρ, can be replaced by the mean density, ρ_0, giving

$$\frac{\partial^2 \rho'}{\partial t^2} - c_0^2 \frac{\partial^2 \rho'}{\partial x_i^2} = \frac{\partial^2 T_{ij}}{\partial x_i \partial x_j} \tag{7}$$

where the Lighthill tensor is approximated by

$$T_{ij} \approx \rho_0 u_i u_j \tag{8}$$

Using the assumption of (6), the flow-generated sound represented by the fluctuating pressure, p', can be written as

$$\frac{1}{c_0^2} \frac{\partial^2 p'}{\partial t^2} - \nabla^2 p' = \frac{\partial^2 T_{ij}}{\partial x_i \partial x_j} \tag{9}$$

where

$$\nabla^2 \equiv \frac{\partial^2}{\partial x_i^2}$$

Equation (9) is called Lighthill's inhomogeneous wave equation. This equation represents Lighthill's theory that a "fictitious" acoustic medium, in which small disturbances occur, acted upon by an external stress produces the same pressure fluctuations as a fluid in which highly non-linear motions may occur [12].

II.1.3 Solution of Lighthill's Wave Equation in the Frequency Domain

It is beneficial to express Lighthill's wave equation in the frequency domain. One advantage of a frequency-domain calculation over a time-domain calculation is that the Green's functions for most wave problems take essentially the same form in the frequency domain. A Fourier transform in time

$$\tilde{p}(\mathbf{x}, \omega) = \frac{1}{2\pi} \int_{-\infty}^{\infty} p'(\mathbf{x}, t) e^{i\omega t} dt$$

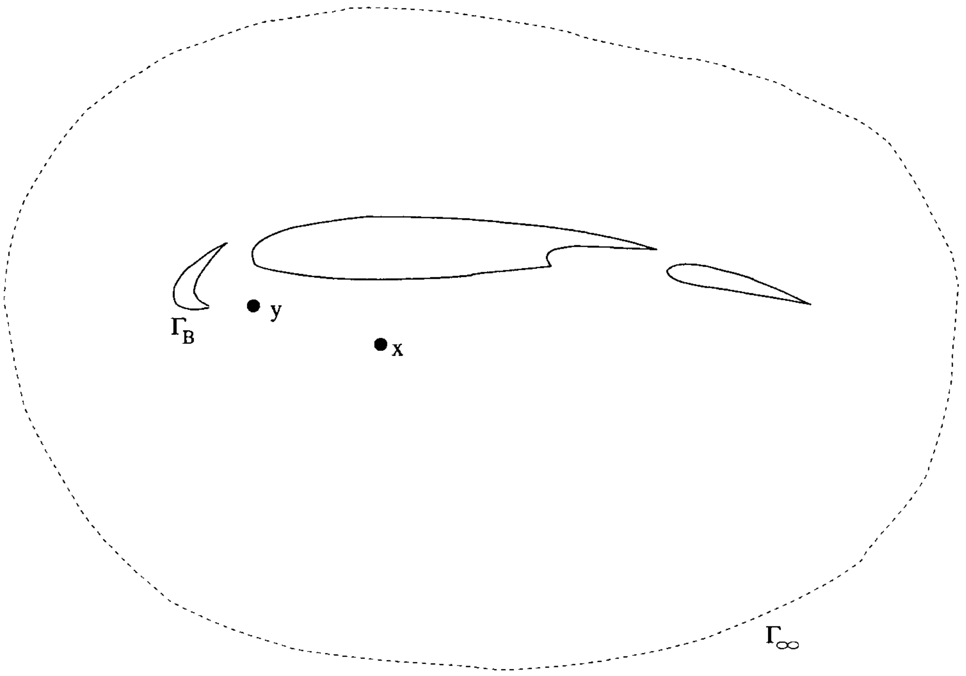

Fig. 1: A schematic of a high-lift wing. Γ_B denotes solid surfaces and Γ_∞ is the far-field boundary toward infinity.

with inverse

$$p'(\mathbf{x},t) = \int_{-\infty}^{\infty} \widetilde{p}(\mathbf{x},\omega)e^{-i\omega t}d\omega$$

is used to transform the variables into the frequency domain and then later back into the time domain. In the above equations and throughout this paper, bold-faced letters indicate vectors or matrices. Applying this transform to equation (9) gives

$$-\frac{\omega^2}{c_0^2}\widetilde{p} - \nabla^2\widetilde{p} = \frac{\partial^2 \widetilde{T}_{ij}}{\partial x_i \partial x_j}$$

where

$$\widetilde{T}_{ij}(\mathbf{x},\omega) = \frac{1}{2\pi}\int_{-\infty}^{\infty} T_{ij}(\mathbf{x},t)e^{i\omega t}dt = \frac{1}{2\pi}\int_{-\infty}^{\infty} \rho_0 u_i(\mathbf{x},t)u_j(\mathbf{x},t)e^{i\omega t}dt$$

This transformed equation is in the form of an inhomogeneous Helmholtz equation. An integral equation can now be derived using an exact Green's function.

Consider a spatial domain Ω with boundary consisting of the far-field contour Γ_∞ and the solid boundary Γ_B as shown in Fig. 1. An exact Green's function in the frequency domain, $\widetilde{g}(\mathbf{x},\mathbf{y},\omega)$, is defined as

$$-\frac{\omega^2}{c_0^2}\widetilde{g} - \nabla^2\widetilde{g} = \delta\left(\mathbf{x}-\mathbf{y}\right) \tag{10}$$

with boundary condition

$$\frac{\partial \tilde{g}}{\partial n} = 0 \text{ on } \Gamma_{\mathrm{B}}$$

Physically, the exact Green's function represents the effect observed at point $\mathbf{x}$ of a unit source located at point $\mathbf{y}$. The desired integral equation can now be derived by applying Green's identity,

$$\int_{\Omega} \left[\tilde{g}\nabla^2\tilde{p} - \tilde{p}\nabla^2\tilde{g}\right] d\mathbf{x} = \int_{\Gamma_\infty + \Gamma_B} \left(\tilde{g}\frac{\partial \tilde{p}}{\partial n} - \tilde{p}\frac{\partial \tilde{g}}{\partial n}\right) dS$$

where the integral on the right-hand-side is a surface, or boundary, integral and the left-hand-side is an integral over the entire domain Ω. The normal direction is inward from Ω indicating solutions will be found in the external domain. The use of Green's identity results in the integral equation

$$\int_{\Omega} \left[\tilde{g}\left(-\frac{\omega^2}{c_0^2}\tilde{p} - \frac{\partial^2 \tilde{T}_{ij}}{\partial x_i \partial x_j}\right) - \tilde{p}\left(-\frac{\omega^2}{c_0^2}\tilde{g} - \delta\left(\mathbf{x} - \mathbf{y}\right)\right)\right] d\mathbf{x}$$

$$= \int_{\Gamma_\infty + \Gamma_B} \left(\tilde{g}\frac{\partial \tilde{p}}{\partial n} - \tilde{p}\frac{\partial \tilde{g}}{\partial n}\right) dS \qquad (11)$$

The exact Green's function is required to obey the Sommerfeld radiation condition,

$$\tilde{g} \to 0, \tilde{p} \to 0 \text{ for the limit on } \Gamma_\infty$$

Combining the radiation condition with the boundary conditions on Γ_B, equation (11) becomes

$$\tilde{p}\left(\mathbf{y}, \omega\right) = \int_{\Omega} \tilde{g}\frac{\partial^2 \tilde{T}_{ij}}{\partial x_i \partial x_j} d\mathbf{x} \qquad (12)$$

Equation (12) shows one advantage of using the exact Green's function: the pressure is determined solely by a volume integral and not by both volume and surface integrals.

The derivative of the Lighthill tensor in the integrand of equation (12) can sometimes be difficult to determine. However, equation (12) can be manipulated to create a more manageable equation. Note that

$$\tilde{g}\frac{\partial^2 \tilde{T}_{ij}}{\partial x_i \partial x_j} = \frac{\partial}{\partial x_i}\left(\tilde{g}\frac{\partial \tilde{T}_{ij}}{\partial x_j}\right) - \frac{\partial \tilde{g}}{\partial x_i}\frac{\partial \tilde{T}_{ij}}{\partial x_j}$$

Combining the above with the divergence theorem,

$$\int_{\Omega} \frac{\partial F_i}{\partial x_i} d\mathbf{x} = \int_{\Gamma_\infty + \Gamma_B} n_i F_i dS$$

equation (12) becomes

$$
\begin{aligned}
\tilde{p}(\mathbf{y},\omega) &= \int_{\Omega}\left[\frac{\partial}{\partial x_i}\left(\tilde{g}\frac{\partial \tilde{T}_{ij}}{\partial x_j}\right) - \frac{\partial \tilde{g}}{\partial x_i}\frac{\partial \tilde{T}_{ij}}{\partial x_j}\right] d\mathbf{x} \\
&= \int_{\Gamma_\infty + \Gamma_B} n_i \tilde{g}\frac{\partial \tilde{T}_{ij}}{\partial x_j} dS - \int_{\Omega}\frac{\partial \tilde{g}}{\partial x_i}\frac{\partial \tilde{T}_{ij}}{\partial x_j} d\mathbf{x} \\
&= -\int_{\Omega}\left[\frac{\partial}{\partial x_j}\left(\frac{\partial \tilde{g}}{\partial x_i}\tilde{T}_{ij}\right) - \frac{\partial^2 \tilde{g}}{\partial x_j \partial x_i}\tilde{T}_{ij}\right] d\mathbf{x} \\
&= -\int_{\Gamma_\infty + \Gamma_B} n_j \frac{\partial \tilde{g}}{\partial x_i}\tilde{T}_{ij} dS + \int_{\Omega}\frac{\partial^2 \tilde{g}}{\partial x_j \partial x_i}\tilde{T}_{ij} d\mathbf{x} \\
&= \int_{\Omega}\frac{\partial^2 \tilde{g}}{\partial x_j \partial x_i}\tilde{T}_{ij} d\mathbf{x}
\end{aligned}
$$

The normal velocity of the fluid is zero on all solid surfaces, i.e., $n_i u_i = 0$, which implies $n_j \tilde{T}_{ij} = 0$ and $n_i \frac{\partial \tilde{T}_{ij}}{\partial x_j} = \frac{\partial (n_i \tilde{T}_{ij})}{\partial x_j} = 0$. Therefore, equation (12) can finally be rewritten as

$$
\tilde{p}(\mathbf{y},\omega) = \int_{\Omega} \tilde{T}_{ij}(\mathbf{x},\omega)\frac{\partial^2 \tilde{g}}{\partial x_j \partial x_i}(\mathbf{x},\mathbf{y},\omega)\, d\mathbf{x} \tag{13}
$$

Equation (13) is the solution to Lighthill's equation in the frequency domain [12, 28]. The term $\frac{\partial^2 \tilde{g}}{\partial x_j \partial x_i}(\mathbf{x},\mathbf{y},\omega)$ in equation (13) is known as the double divergence of the exact Green's function. By the inverse Fourier transform of $\tilde{p}$, the pressure at any far-field point $\mathbf{y}$ is

$$
p'(\mathbf{y},t) = \int_{-\infty}^{\infty}\tilde{p}(\mathbf{y},\omega)e^{-i\omega t}d\omega = \int_{-\infty}^{\infty}\int_{\Omega}\tilde{T}_{ij}(\mathbf{x},\omega)\frac{\partial^2 \tilde{g}}{\partial x_j \partial x_i}(\mathbf{x},\mathbf{y},\omega)e^{-i\omega t}d\mathbf{x}d\omega \tag{14}
$$

II.2 BOUNDARY INTEGRAL EQUATION FOR THE EXACT GREEN'S FUNCTION

In this section, a three-dimensional integral equation is formulated for the exact Green's function. The integral equation is subsequently modified to a two-dimensional boundary integral equation (BIE) by considering cylindrical bodies with constant cross-sections.

II.2.1 Formulation of the Boundary Integral Equation

The boundary integral equation is formulated from a partial differential equation (PDE) using an exact Green's function, which is defined as the solution, in the time domain, to the convective wave equation

$$
(\frac{\partial}{\partial t} + \mathbf{U}\cdot\nabla)^2 g(\mathbf{x},\mathbf{y},t,s) - \nabla^2 g(\mathbf{x},\mathbf{y},t,s) = \delta(t-s)\delta(\mathbf{x}-\mathbf{y}) \tag{15}
$$

with boundary condition for its normal derivative

$$\frac{\partial g}{\partial n} = 0 \tag{16}$$

on all solid surfaces where

$$\nabla \equiv \left(\frac{\partial}{\partial x_1}, \frac{\partial}{\partial x_2}, \frac{\partial}{\partial x_3} \right)$$

In equation (15), $\mathbf{y}$ is a fixed source point and $\mathbf{x} = (x_1, x_2, x_3)$ is a near-field point where the solution is desired. The source point, $\mathbf{y}$, can also represent a far-field observation point by replacing $\mathbf{U}$ with $-\mathbf{U}$. Without loss of generality, the uniform mean flow is assumed to be in the direction of x_1 only, and is defined as $\mathbf{U} = (M, 0, 0)$ where M is the Mach number. The exact, or "tailored", Green's function, $g(\mathbf{x}, \mathbf{y}, t, s)$, is exclusive to the geometry of the problem [22]. The source term, $\delta(t-s)\delta(\mathbf{x}-\mathbf{y})$, is equivalent to an initial velocity of magnitude $\delta(\mathbf{x}-\mathbf{y})$ at time s [38]. A solution of the convective wave equation is sought in the frequency domain. After applying a Fourier transform in time, as described in section II.1.3, equation (15) becomes

$$(-i\omega + \mathbf{U} \cdot \nabla)^2 \tilde{g}(\mathbf{x}, \mathbf{y}, \omega, s) - \nabla^2 \tilde{g}(\mathbf{x}, \mathbf{y}, \omega, s) = e^{i\omega s} \delta(\mathbf{x} - \mathbf{y}) \tag{17}$$

with boundary condition

$$\frac{\partial \tilde{g}}{\partial n} = 0 \tag{18}$$

where $\tilde{g}(\mathbf{x}, \mathbf{y}, \omega, s)$ is the exact Green's function in the frequency domain.

The solution of a differential equation over an unbounded region, with a point source of unit strength, is called the free-space Green's function of the equation. A direct formulation, i.e., obtaining the exact Green's function by solving the adjoint of the convective wave equation, will be used to transform equation (15) into a boundary integral equation [13, 45]. Consider the free-space Green's function for the adjoint problem,

$$(-i\omega - \mathbf{U} \cdot \nabla)^2 \tilde{g}_0(\mathbf{x}, \mathbf{z}, \omega) - \nabla^2 \tilde{g}_0(\mathbf{x}, \mathbf{z}, \omega) = \delta(\mathbf{x} - \mathbf{z}) \tag{19}$$

In the above equation, $\tilde{g}_0(\mathbf{x}, \mathbf{z}, \omega)$ satisfies only the Sommerfeld radiation condition. The free-space Green's function that satisfies equation (19) is established and takes the form [15, 30]

$$\tilde{g}_0(\mathbf{x}, \mathbf{z}, \omega) = e^{i\omega M (x_1 - z_1)/\beta^2} \frac{e^{i\frac{\omega}{\beta}\sqrt{(x_1-z_1)^2/\beta^2 + (x_2-z_2)^2 + (x_3-z_3)^2}}}{4\pi\beta\sqrt{(x_1-z_1)^2/\beta^2 + (x_2-z_2)^2 + (x_3-z_3)^2}} \tag{20}$$

where

$$\beta = \sqrt{1 - M^2}$$

Now, equation (17) is multiplied by $\tilde{g}_0(\mathbf{x}, \mathbf{z}, \omega)$ and equation (19) is multiplied by $\tilde{g}(\mathbf{x}, \mathbf{y}, \omega, s)$ and the two are subtracted to get

$$-2i\omega[\tilde{g}_0 \mathbf{U} \cdot \nabla \tilde{g} + \tilde{g} \mathbf{U} \cdot \nabla \tilde{g}_0] + \tilde{g}_0 (\mathbf{U} \cdot \nabla)^2 \tilde{g} - \tilde{g} (\mathbf{U} \cdot \nabla)^2 \tilde{g}_0 - \left[\tilde{g}_0 \nabla^2 \tilde{g} - \tilde{g} \nabla^2 \tilde{g}_0\right]$$
$$= \tilde{g}_0 e^{i\omega s} \delta(\mathbf{x} - \mathbf{y}) - \tilde{g} \delta(\mathbf{x} - \mathbf{z}) \tag{21}$$

Applying the properties

$$\tilde{g}_0 \mathbf{U} \cdot \nabla \tilde{g} + \tilde{g} \mathbf{U} \cdot \nabla \tilde{g}_0 = \mathbf{U} \cdot \nabla \left(\tilde{g}_0 \tilde{g}\right)$$

and

$$\tilde{g}_0 \nabla^2 \tilde{g} - \tilde{g} \nabla^2 \tilde{g}_0 = \nabla \left(\tilde{g}_0 \nabla \tilde{g} - \tilde{g} \nabla \tilde{g}_0\right)$$

to equation (21) gives

$$\nabla[-2i\omega \tilde{g}_0 \tilde{g} \mathbf{U} + \left(\tilde{g}_0 \mathbf{U} \cdot \nabla \tilde{g} - \tilde{g} \mathbf{U} \cdot \nabla \tilde{g}_0\right) \mathbf{U} - \left(\tilde{g}_0 \nabla \tilde{g} - \tilde{g} \nabla \tilde{g}_0\right)]$$
$$= \tilde{g}_0(\mathbf{x}, \mathbf{z}, \omega) e^{i\omega s} \delta(\mathbf{x} - \mathbf{y}) - \tilde{g}(\mathbf{x}, \mathbf{y}, \omega, s) \delta(\mathbf{x} - \mathbf{z}) \tag{22}$$

Denote Ω the body of fluids external to all solid bodies. Integrate equation (22) over Ω and utilize the divergence theorem to get

$$\int_S \mathbf{n} \cdot \left[-2i\omega \tilde{g}_0 \tilde{g} \mathbf{U} + \left(\tilde{g}_0 \mathbf{U} \cdot \nabla \tilde{g} - \tilde{g} \mathbf{U} \cdot \nabla \tilde{g}_0\right) \mathbf{U} - \left(\tilde{g}_0 \nabla \tilde{g} - \tilde{g} \nabla \tilde{g}_0\right)\right] d\mathbf{x}_s$$
$$= e^{i\omega s} \tilde{g}_0(\mathbf{y}, \mathbf{z}, \omega) - \tilde{g}(\mathbf{z}, \mathbf{y}, \omega, s) \tag{23}$$

where S represents all solid boundaries and $\mathbf{x}_s$ symbolizes a point on S. The normal vector, $\mathbf{n}$, is directed out of the fluid and into any solid bodies. The last term in the integral above becomes

$$\int_S \mathbf{n} \cdot \left(\widetilde{g_0} \nabla \tilde{g} - \tilde{g} \nabla \widetilde{g_0}\right) d\mathbf{x}_s = \int_\Omega \left(\widetilde{g_0} \nabla^2 \tilde{g} - \tilde{g} \nabla^2 \widetilde{g_0}\right) d\mathbf{x}$$
$$= - \int_S \left(\tilde{g} \frac{\partial \widetilde{g_0}}{\partial n} - \widetilde{g_0} \frac{\partial \tilde{g}}{\partial n}\right) d\mathbf{x}_s$$
$$= - \int_S \tilde{g} \frac{\partial \widetilde{g_0}}{\partial n} d\mathbf{x}_s$$

after applying the divergence theorem, Green's identity and boundary condition (18). Then, the integral relation for the exact Green's function in three-dimensional space is

$$\tilde{g}(\mathbf{z}, \mathbf{y}, \omega, s) = e^{i\omega s} \tilde{g}_0(\mathbf{y}, \mathbf{z}, \omega) + \int_S [2i\omega U_n \tilde{g}_0(\mathbf{x}_s, \mathbf{z}, \omega) \tilde{g}(\mathbf{x}_s, \mathbf{y}, \omega, s)$$

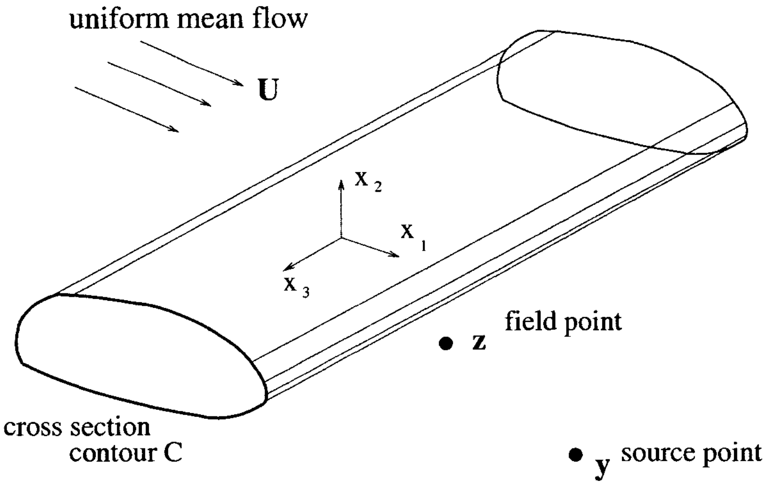

Fig. 2: Schematic of a cylindrical body in a uniform flow.

$$+U_n\left[\mathbf{U}\cdot\nabla\tilde{g}_0(\mathbf{x}_s,\mathbf{z},\omega)\right]\tilde{g}(\mathbf{x}_s,\mathbf{y},\omega,s)-\frac{\partial\tilde{g}_0}{\partial n}(\mathbf{x}_s,\mathbf{z},\omega)\,\tilde{g}(\mathbf{x}_s,\mathbf{y},\omega,s)$$

$$-U_n\tilde{g}_0(\mathbf{x}_s,\mathbf{z},\omega)\left[\mathbf{U}\cdot\nabla\tilde{g}(\mathbf{x}_s,\mathbf{y},\omega,s)\right]\Big]\,d\mathbf{x}_s \tag{24}$$

where

$$U_n\equiv\mathbf{n}\cdot\mathbf{U}$$

The power of formulation (24) lies in the fact that it relates the exact Green's function and its derivative on the boundary alone; no volume integral is contained in the equation. A boundary integral equation is obtained by taking the limit as the external point, $\mathbf{z}$, tends to a boundary point, $\mathbf{z}_s$.

II.2.2 Boundary Integral Equation for a Cylindrical Body

Frequently, a two-dimensional formulation can be used to approximate an acoustical problem that arises from an engineering application. One example is the sound that the leading-edge slats of aircraft high-lift systems generate. A large part of the slats' solid surfaces spans two dimensions, so that the problem can be reduced to a two-dimensional problem [19]. Consider a cylindrical body of constant cross-section in the x_1-x_2 plane as shown in Fig. 2. Since the cross-section is uniform throughout the cylinder, the equation for the solid surface is independent of the third variable, x_3. In this case, it is convenient to introduce a Fourier transform of $\tilde{g}(\mathbf{z},\mathbf{y},\omega,s)$ in z_3 as

$$\hat{g}\left(\bar{\mathbf{z}},k_3,\mathbf{y},\omega,s\right)=\frac{1}{2\pi}\int_{-\infty}^{\infty}\tilde{g}(\mathbf{z},\mathbf{y},\omega,s)e^{ik_3z_3}dz_3 \tag{25}$$

and its inverse

$$\widetilde{g}(\mathbf{z},\mathbf{y},\omega,s)=\int_{-\infty}^{\infty}\widehat{g}\left(\overline{\mathbf{z}},k_3,\mathbf{y},\omega,s\right)e^{-ik_3z_3}dk_3 \tag{26}$$

where $\widehat{g}$ is the transformed function and $\overline{\mathbf{z}}=(z_1,z_2)$. Applying the Fourier transform to (24) gives

$$\begin{aligned}\widehat{g}\left(\overline{\mathbf{z}},k_3,\mathbf{y},\omega,s\right)=e^{i\omega s}\widehat{g}_0\left(\mathbf{y},\overline{\mathbf{z}},k_3,\omega\right)+\int_S&\left[2i\omega U_n\widehat{g}_0(\mathbf{x}_s,\overline{\mathbf{z}},k_3,\omega)\widetilde{g}(\mathbf{x}_s,\mathbf{y},\omega,s)\right.\\ +U_n\left[\mathbf{U}\cdot\nabla\widehat{g}_0(\mathbf{x}_s,\overline{\mathbf{z}},k_3,\omega)\right]\widetilde{g}(\mathbf{x}_s,\mathbf{y},\omega,s)&-\frac{\partial\widehat{g}_0}{\partial n}\left(\mathbf{x}_s,\overline{\mathbf{z}},k_3,\omega\right)\widetilde{g}(\mathbf{x}_s,\mathbf{y},\omega,s)\\ &\left.-U_n\widehat{g}_0(\mathbf{x}_s,\overline{\mathbf{z}},k_3,\omega)\left[\mathbf{U}\cdot\nabla\widetilde{g}(\mathbf{x}_s,\mathbf{y},\omega,s)\right]\right]d\mathbf{x}_s\end{aligned} \tag{27}$$

where $\widehat{g}_0(\mathbf{y},\overline{\mathbf{z}},k_3,\omega)$ represents the Fourier transform of the free-space Green's function, which is

$$\begin{aligned}\widehat{g}_0\left(\mathbf{y},\overline{\mathbf{z}},k_3,\omega\right)=\int_{-\infty}^{\infty}e^{i\omega M(y_1-z_1)/\beta^2}&\frac{e^{i\omega/\beta\sqrt{(y_1-z_1)^2/\beta^2+(y_2-z_2)^2+(y_3-z_3)^2}}}{4\pi\beta\sqrt{(y_1-z_1)^2/\beta^2+(y_2-z_2)^2+(y_3-z_3)^2}}\\ &\times e^{ik_3z_3}dz_3=e^{ik_3y_3}G_0(\overline{\mathbf{y}},\overline{\mathbf{z}},\overline{\omega})\end{aligned} \tag{28}$$

In equation (28), a barred variable denotes two-dimensions, such as

$$\overline{\mathbf{y}}=(y_1,y_2),\quad \overline{r}=\sqrt{(y_1-z_1)^2/\beta^2+(y_2-z_2)^2},\quad \overline{\omega}=\sqrt{\omega^2/\beta^2-k_3^2}$$

and

$$G_0(\overline{\mathbf{y}},\overline{\mathbf{z}},\overline{\omega})=\frac{i}{4\beta}e^{i\omega M(y_1-z_1)/\beta^2}H_0^{(1)}\left(\overline{\omega}\overline{r}\right) \tag{29}$$

where $H_0^{(1)}\left(\overline{\omega}\overline{r}\right)$ is the zeroth-order Hankel function of the first kind (Appendix A). Note that because the cross-section is independent of z_3,

$$\int_S ...d\mathbf{x}_s=\int_C\int_{-\infty}^{\infty}...dx_3d\overline{\mathbf{x}}_s$$

and therefore, equation (27) can be rewritten as

$$\begin{aligned}\widehat{g}\left(\overline{\mathbf{z}},k_3,\mathbf{y},\omega,s\right)=e^{ik_3y_3}e^{i\omega s}G_0\left(\overline{\mathbf{y}},\overline{\mathbf{z}},\overline{\omega}\right)+\int_C\int_{-\infty}^{\infty}&\left[2i\omega U_ne^{ik_3x_3}G_0(\overline{\mathbf{x}}_s,\overline{\mathbf{z}},\overline{\omega})\widetilde{g}(\mathbf{x}_s,\mathbf{y},\omega,s)\right.\\ +U_n\left[\mathbf{U}\cdot\nabla e^{ik_3x_3}G_0(\overline{\mathbf{x}}_s,\overline{\mathbf{z}},\overline{\omega})\right]\widetilde{g}(\mathbf{x}_s,\mathbf{y},\omega,s)&-e^{ik_3x_3}\frac{\partial G_0}{\partial n}\left(\overline{\mathbf{x}}_s,\overline{\mathbf{z}},\overline{\omega}\right)\widetilde{g}(\mathbf{x}_s,\mathbf{y},\omega,s)\\ &\left.-U_ne^{ik_3x_3}G_0(\overline{\mathbf{x}}_s,\overline{\mathbf{z}},\overline{\omega})\left[\mathbf{U}\cdot\nabla\widetilde{g}(\mathbf{x}_s,\mathbf{y},\omega,s)\right]\right]dx_3d\overline{\mathbf{x}}_s\end{aligned} \tag{30}$$

where C signifies the contour of the solid surface cross-section. Integrating equation (30) with respect to x_3 results in

$$\widehat{g}\left(\overline{\mathbf{z}},k_3,\mathbf{y},\omega,s\right)=e^{ik_3y_3}e^{i\omega s}G_0\left(\overline{\mathbf{y}},\overline{\mathbf{z}},\overline{\omega}\right)+\int_C\left[2i\omega U_nG_0(\overline{\mathbf{x}}_s,\overline{\mathbf{z}},\overline{\omega})\widehat{g}(\overline{\mathbf{x}}_s,k_3,\mathbf{y},\omega,s)\right.$$

$$+U_n\left[\mathbf{U}\cdot\nabla G_0(\overline{\mathbf{x}}_s,\overline{\mathbf{z}},\overline{\omega})\right]\widehat{g}(\overline{\mathbf{x}}_s,k_3,\mathbf{y},\omega,s)-\frac{\partial G_0}{\partial n}(\overline{\mathbf{x}}_s,\overline{\mathbf{z}},\overline{\omega})\,\widehat{g}(\overline{\mathbf{x}}_s,k_3,\mathbf{y},\omega,s)$$
$$-U_nG_0(\overline{\mathbf{x}}_s,\overline{\mathbf{z}},\overline{\omega})\left[\mathbf{U}\cdot\nabla\widehat{g}(\overline{\mathbf{x}}_s,k_3,\mathbf{y},\omega,s)\right]]\,d\overline{\mathbf{x}}_s \tag{31}$$

In order to simplify equation (31), it is convenient to express $\widehat{g}(\overline{\mathbf{z}},k_3,\mathbf{y},\omega,s)$ as

$$\widehat{g}(\overline{\mathbf{z}},k_3,\mathbf{y},\omega,s)=e^{i\omega s}e^{ik_3y_3}G_B(\overline{\mathbf{z}},\overline{\mathbf{y}},\overline{\omega}) \tag{32}$$

Note that for two-dimensional surfaces, $U_3=0$ and $n_3=0$. Since $\mathbf{U}=(M,0,0)$,

$$\mathbf{U}\cdot\nabla G_0\left(\overline{\mathbf{x}}_s,\overline{\mathbf{z}},\overline{\omega}\right)=M\frac{\partial G_0}{\partial x_1}\left(\overline{\mathbf{x}}_s,\overline{\mathbf{z}},\overline{\omega}\right)$$

and

$$U_n\equiv\mathbf{n}\cdot\mathbf{U}=(n_1,n_2,0)\cdot(M,0,0)=Mn_1$$

As a result,

$$U_n\left[\mathbf{U}\cdot\nabla G_0\left(\overline{\mathbf{x}}_s,\overline{\mathbf{z}},\overline{\omega}\right)\right]-\frac{\partial G_0}{\partial n}\left(\overline{\mathbf{x}}_s,\overline{\mathbf{z}},\overline{\omega}\right)$$
$$=M^2n_1\frac{\partial G_0}{\partial x_1}\left(\overline{\mathbf{x}}_s,\overline{\mathbf{z}},\overline{\omega}\right)-n_1\frac{\partial G_0}{\partial x_1}\left(\overline{\mathbf{x}}_s,\overline{\mathbf{z}},\overline{\omega}\right)-n_2\frac{\partial G_0}{\partial x_2}\left(\overline{\mathbf{x}}_s,\overline{\mathbf{z}},\overline{\omega}\right)$$
$$=-\beta^2n_1\frac{\partial G_0}{\partial x_1}\left(\overline{\mathbf{x}}_s,\overline{\mathbf{z}},\overline{\omega}\right)-n_2\frac{\partial G_0}{\partial x_2}\left(\overline{\mathbf{x}}_s,\overline{\mathbf{z}},\overline{\omega}\right)$$

Further,

$$U_n\left[\mathbf{U}\cdot\nabla\widehat{g}\left(\overline{\mathbf{x}}_s,k_3,\mathbf{y},\omega,s\right)\right]=U_n\left[\left(U_n\mathbf{n}+U_t\mathbf{t}\right)\cdot\nabla\widehat{g}\left(\overline{\mathbf{x}}_s,k_3,\mathbf{y},\omega,s\right)\right]$$
$$=U_nU_t\mathbf{t}\cdot\nabla\widehat{g}\left(\overline{\mathbf{x}}_s,k_3,\mathbf{y},\omega,s\right)=U_nU_t\frac{\partial\widehat{g}\left(\overline{\mathbf{x}}_s,k_3,\mathbf{y},\omega,s\right)}{\partial\overline{x}_s}$$

where $\frac{\partial\widehat{g}(\overline{\mathbf{x}}_s,k_3,\mathbf{y},\omega,s)}{\partial\overline{x}_s}$ is the tangential derivative of $\widehat{g}$ and $\mathbf{t}$ is the unit vector tangent to the surface. Because a solution in the exterior domain is sought, contour integration will be performed in the clockwise direction, so that $\mathbf{t}=(-n_2,n_1,0)$. Utilizing (32) and the above equations, (31) becomes

$$G_B(\overline{\mathbf{z}},\overline{\mathbf{y}},\overline{\omega})=G_0\left(\overline{\mathbf{y}},\overline{\mathbf{z}},\overline{\omega}\right)+\int_C\left[i\omega U_nG_0(\overline{\mathbf{x}}_s,\overline{\mathbf{z}},\overline{\omega})G_B(\overline{\mathbf{x}}_s,\overline{\mathbf{y}},\overline{\omega})\right.$$
$$\left.-G_1(\overline{\mathbf{x}}_s,\overline{\mathbf{z}},\overline{\omega})G_B(\overline{\mathbf{x}}_s,\overline{\mathbf{y}},\overline{\omega})-U_nU_tG_0(\overline{\mathbf{x}}_s,\overline{\mathbf{z}},\overline{\omega})\frac{\partial G_B(\overline{\mathbf{x}}_s,\overline{\mathbf{y}},\overline{\omega})}{\partial\overline{x}_s}\right]d\overline{\mathbf{x}}_s \tag{33}$$

where

$$G_1(\overline{\mathbf{x}},\overline{\mathbf{z}},\overline{\omega})=-\frac{i\overline{\omega}}{4\beta}e^{i\frac{\omega M(x_1-z_1)}{\beta^2}}\frac{\left(\overline{\mathbf{x}}-\overline{\mathbf{z}}\right)\cdot\mathbf{n}}{\overline{r}}H_1^{(1)}\left(\overline{\omega}\overline{r}\right) \tag{34}$$

and

$$U_t\equiv\mathbf{t}\cdot\mathbf{U}=(-n_2,n_1,0)\cdot(M,0,0)=-Mn_2$$

Equation (33) is equivalent to the integral relation for the two-dimensional convective Helmholtz equation when $k_3 = 0$. In (34), $H_1^{(1)}(\overline{\omega} r)$ is the first-order Hankel function of the first kind (Appendix A).

To solve equation (33), the unknown, $G_B(\overline{\mathbf{x}}_s, \overline{\mathbf{y}}, \overline{\omega})$, needs to be determined. This is accomplished by taking the limit of (33) as $\overline{\mathbf{z}}$ approaches $\overline{\mathbf{z}}_s$, where $\overline{\mathbf{z}}_s$ is a point on the contour C. This results in

$$C_s G_B(\overline{\mathbf{z}}_s, \overline{\mathbf{y}}, \overline{\omega}) = G_0\left(\overline{\mathbf{y}}, \overline{\mathbf{z}}_s, \overline{\omega}\right) + \int_C i\omega U_n G_0(\overline{\mathbf{x}}_s, \overline{\mathbf{z}}_s, \overline{\omega}) G_B(\overline{\mathbf{x}}_s, \overline{\mathbf{y}}, \overline{\omega}) d\overline{\mathbf{x}}_s$$
$$- \int_C G_1(\overline{\mathbf{x}}_s, \overline{\mathbf{z}}_s, \overline{\omega}) G_B(\overline{\mathbf{x}}_s, \overline{\mathbf{y}}, \overline{\omega}) d\overline{\mathbf{x}}_s - \int_C U_n U_t G_0(\overline{\mathbf{x}}_s, \overline{\mathbf{z}}_s, \overline{\omega}) \frac{\partial G_B(\overline{\mathbf{x}}_s, \overline{\mathbf{y}}, \overline{\omega})}{\partial \overline{x}_s} d\overline{\mathbf{x}}_s \qquad (35)$$

The constant C_s appears in equation (35) due to the singularity of $G_1(\overline{\mathbf{x}}_s, \overline{\mathbf{z}}_s, \overline{\omega})$. The derivation of C_s can be found in [13]. For smooth boundary points, the value of C_s is 0.5 [2, 13]. Once equation (35) is used to calculate G_B on the surface, equation (33) can be solved for G_B at any field point $\overline{\mathbf{z}}$ for a source located at $\overline{\mathbf{y}}$. Then, the double divergence needed for the acoustic analogy can be obtained by direct computation of the spatial derivatives of (33) as follows,

$$\frac{\partial^2}{\partial z_i \partial z_j} G_B(\overline{\mathbf{z}}, \overline{\mathbf{y}}, \overline{\omega}) = \frac{\partial^2}{\partial z_i \partial z_j} G_0\left(\overline{\mathbf{y}}, \overline{\mathbf{z}}, \overline{\omega}\right) + \int_C \left[i\omega U_n \left(\frac{\partial^2}{\partial z_i \partial z_j} G_0(\overline{\mathbf{x}}_s, \overline{\mathbf{z}}, \overline{\omega}) \right) G_B(\overline{\mathbf{x}}_s, \overline{\mathbf{y}}, \overline{\omega}) \right.$$
$$- \left(\frac{\partial^2}{\partial z_i \partial z_j} G_1(\overline{\mathbf{x}}_s, \overline{\mathbf{z}}, \overline{\omega}) \right) G_B(\overline{\mathbf{x}}_s, \overline{\mathbf{y}}, \overline{\omega})$$
$$\left. - U_n U_t \left(\frac{\partial^2}{\partial z_i \partial z_j} G_0(\overline{\mathbf{x}}_s, \overline{\mathbf{z}}, \overline{\omega}) \right) \frac{\partial G_B(\overline{\mathbf{x}}_s, \overline{\mathbf{y}}, \overline{\omega})}{\partial \overline{x}_s} \right] d\overline{\mathbf{x}}_s \qquad (36)$$

CHAPTER III

APPLICATION OF SPECTRAL COLLOCATION BEM TO SMOOTH BOUNDARIES

III.1 SPECTRAL COLLOCATION BOUNDARY ELEMENT METHOD

III.1.1 General Discussion of the Boundary Element Method

The Boundary Element Method (BEM) begins with the re-formulation of a partial differential equation (PDE), such as the two-dimensional Helmholtz equation, into an integral equation that is mathematically equivalent to the original PDE. Only certain PDEs can be converted into integral equations, hence the BEM is not as widely applicable as the Finite Difference Method (FDM) or the Finite Element Method (FEM) [27]. However, when appropriate, the BEM has several advantages over the FDM and FEM. First, the BEM requires only the boundary of the domain to be discretized, as opposed to the FDM and FEM, which involve the generation of a mesh over the entire domain. This effectively reduces the dimension of the problem by one. As a result, the BEM leads to smaller systems of linear equations, less computation time and less computer memory requirements [11]. Another advantage of the BEM arises when dealing with an unbounded domain, such as in acoustical wave problems. In FDM and FEM schemes, the domain needs to be truncated and approximated at some finite "fictitious" external boundary, which produces errors in the solution [14]. This truncation also necessitates the introduction of special techniques to satisfy the Sommerfeld radiation condition at infinity. In the BEM, the radiation condition is automatically satisfied by the choice of boundary conditions.

After obtaining the boundary integral equation, the next step in the BEM is to discretize the boundary into "elements". Then, a geometrical approximation is made concerning the shape of the element. This approach allows complex geometries to be represented using simple geometrical shapes. A second approximation required for each element involves the dependent variable. Even though the boundary has been reduced to a summation of integrals over each element, the behavior of the exact Green's function and its normal derivative is not known within each element. To determine this functional behavior, the BIE is required to be satisfied at fixed points, called nodes, along each element. This last approximation leads to a system of linear equations, which are then written in matrix form in order to solve the BIE for the exact Green's function numerically. In this paper, a spectral collocation boundary element method is used to solve the BIE.

III.1.2 Formulation of the Spectral Collocation Boundary Element Method

Consider the cylindrical cross-section contour C in Fig. 2. Let the contour be divided into N elements Γ_j as

$$C = \bigcup_{j=1}^{N} \Gamma_j$$

Let the boundary of each element be parameterized as

$$\overline{\mathbf{x}}_s = \mathbf{r}_j(\bar{t}), \bar{t} \in [0,1] \tag{37}$$

where $\bar{t}$ is the local parameterization variable (one-dimensional) and $\mathbf{r}_j(\bar{t})$ is the shape function for the jth element. The most commonly used shape function for two-dimensional problems is a straight line [34]. However, polynomials of higher orders, circular arcs or splines can be used to discretize the geometry. A cubic spline was chosen for $\mathbf{r}_j(\bar{t})$. The exact Green's function on each Γ_j is approximated by an expansion in a set of basis functions, $\{\phi_n(\bar{t}), n = 0, 1, 2, \ldots, P\}$, giving

$$G_B(\overline{\mathbf{x}}_s, \overline{\mathbf{y}}, \overline{\omega}) = G_B(\mathbf{r}_j(\bar{t}), \overline{\mathbf{y}}, \overline{\omega}) = \sum_{n=0}^{P} u_j^{(n)} \phi_n(\bar{t}) \tag{38}$$

where $u_j^{(n)}$ signifies the expansion coefficients and P represents the highest order of the expansion polynomials. Substituting the summation in equation (38) into the right-hand-side of equation (35) and using the property

$$\frac{\partial G_B(\overline{\mathbf{x}}_s, \overline{\mathbf{y}}, \overline{\omega})}{\partial \overline{x}_s} = \nabla G_B \cdot \frac{\mathbf{r}'(\bar{t})}{|\mathbf{r}'(\bar{t})|} = \frac{1}{|\mathbf{r}'(\bar{t})|} \frac{\partial G_B}{\partial \bar{t}}$$

results in

$$\frac{1}{2} G_B(\overline{\mathbf{z}}_s, \overline{\mathbf{y}}, \overline{\omega}) = G_0\left(\overline{\mathbf{y}}, \overline{\mathbf{z}}_s, \overline{\omega}\right) + \sum_{j=1}^{N} \int_0^1 i\overline{\omega} U_n G_0(\mathbf{r}_j(\bar{t}), \overline{\mathbf{z}}_s, \overline{\omega}) \left[\sum_{n=0}^{P} u_j^{(n)} \phi_n(\bar{t})\right] \left|\mathbf{r}_j'(\bar{t})\right| d\bar{t}$$

$$- \sum_{j=1}^{N} \int_0^1 G_1(\mathbf{r}_j(\bar{t}), \overline{\mathbf{z}}_s, \overline{\omega}) \left[\sum_{n=0}^{P} u_j^{(n)} \phi_n(\bar{t})\right] \left|\mathbf{r}_j'(\bar{t})\right| d\bar{t}$$

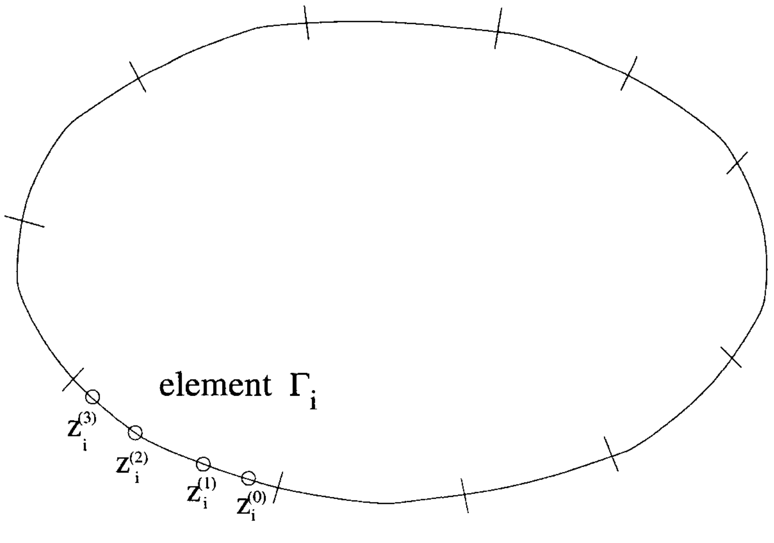

Fig. 3: Schematic diagram showing boundary elements and collocation points.

$$-\sum_{j=1}^{N}\int_0^1 U_n U_t G_0(\mathbf{r}_j(\bar{t}),\bar{\mathbf{z}}_s,\bar{\omega})\left[\sum_{n=0}^{P} u_j^{(n)}\phi_n'(\bar{t})\right]d\bar{t} \tag{39}$$

In equation (39), a prime designates the derivative of a function with respect to $\bar{t}$.

The basis of the spectral collocation method is to try to minimize the residual function that is expressed when the basis function series approximation is substituted into the BIE. This is done by choosing the expansion coefficients so that the residual is zero at a set of points equal in number to the undetermined coefficients. For a finite interval, Chebyshev polynomials (Appendix B) are optimal for the basis set, since any finite interval can be mapped to $[-1,1]$. After selecting the basis set, a good choice for collocation points is the set of Gauss-Chebyshev points (Appendix B) [7]. Let the set of collocation points be defined as

$$\bar{\mathbf{z}}_s = \bar{\mathbf{z}}_i^{(\ell)} \text{ on element } \Gamma_i \text{ where } \bar{\mathbf{z}}_i^{(\ell)} = \mathbf{r}_i(\bar{t}_\ell), \ell = 0, 1, ..., P$$

as shown in Fig. 3. Then, expanding the left-hand-side of equation (39) in the set of Chebyshev basis functions yields

$$\frac{1}{2}\sum_{n=0}^{P} u_i^{(n)}\phi_n(\bar{t}_\ell) = G_0\left(\bar{\mathbf{y}},\bar{\mathbf{z}}_i^{(\ell)},\bar{\omega}\right)+\sum_{j=1}^{N}\int_0^1 i\omega U_n G_0(\mathbf{r}_j(\bar{t}),\bar{\mathbf{z}}_i^{(\ell)},\bar{\omega})\left[\sum_{n=0}^{P} u_j^{(n)}\phi_n(\bar{t})\right]\left|\mathbf{r}_j'(\bar{t})\right|d\bar{t}$$

$$-\sum_{j=1}^{N}\int_0^1 G_1(\mathbf{r}_j(\bar{t}),\bar{\mathbf{z}}_i^{(\ell)},\bar{\omega})\left[\sum_{n=0}^{P} u_j^{(n)}\phi_n(\bar{t})\right]\left|\mathbf{r}_j'(\bar{t})\right|d\bar{t}$$

$$-\sum_{j=1}^{N}\int_0^1 U_n U_t G_0(\mathbf{r}_j(\bar{t}),\bar{\mathbf{z}}_i^{(\ell)},\bar{\omega})\left[\sum_{n=0}^{P} u_j^{(n)}\phi_n'(\bar{t})\right]d\bar{t} \tag{40}$$

for $\ell = 0, 1, \ldots, P$ and $i = 1, \ldots, N$. This is a linear system of equations that can be written in matrix form as

$$\mathbf{H}\mathbf{u} = \mathbf{g} \tag{41}$$

where $\mathbf{u}$ is a vector made up of the expansion coefficients, $u_j^{(n)}$, shown below.

$$\mathbf{u} = \begin{bmatrix} u_1^{(0)} \\ u_1^{(1)} \\ \cdot \\ \cdot \\ u_N^{(P)} \end{bmatrix}_{N(P+1)\times 1}$$

The matrix $\mathbf{H}$ and the vector $\mathbf{g}$ contain entries

$$\begin{aligned}\{\mathbf{H}\}_{IJ} = {} & \frac{1}{2}\phi_n(\bar{t}_\ell)\delta_{ij} + \int_0^1 G_1(\mathbf{r}_j(\bar{t}),\bar{\mathbf{z}}_i^{(\ell)},\bar{\omega})\phi_n(\bar{t})\left|\mathbf{r}_j'(\bar{t})\right| d\bar{t} \\ & - \int_0^1 i\omega U_n G_0(\mathbf{r}_j(\bar{t}),\bar{\mathbf{z}}_i^{(\ell)},\bar{\omega})\phi_n(\bar{t})\left|\mathbf{r}_j'(\bar{t})\right| d\bar{t} \\ & + \int_0^1 U_n U_t G_0(\mathbf{r}_j(\bar{t}),\bar{\mathbf{z}}_i^{(\ell)},\bar{\omega})\phi_n'(\bar{t})d\bar{t} \end{aligned} \tag{42}$$

$$\{\mathbf{g}\}_I = G_0\left(\bar{\mathbf{y}},\bar{\mathbf{z}}_i^{(\ell)},\bar{\omega}\right) \tag{43}$$

for $I = (i-1)(P+1)+\ell$, $J = (j-1)(P+1)+n$ and $\ell, n = 0, 1, 2, \ldots, P$. The integrals in matrix $\mathbf{H}$ are to be evaluated by numerical quadrature.

III.1.3 Treatment of Kernel Singularities

The goal in using the spectral collocation boundary element method is to achieve spectral accuracy. This cannot be accomplished unless the singularities contained in the integral kernels of matrix $\mathbf{H}$ are carefully removed [21]. Specifically, the free-space Green's function and its normal derivative both have a logarithmic singularity when $j = i$, i.e., when the collocation point is on the element being integrated. In equation (29), denote $E = e^{i\omega M\left[\mathbf{r}_i(\bar{t})-\bar{\mathbf{z}}_i^{(\ell)}\right]_1/\beta^2}$ to get

$$G_0(\mathbf{r}_j(\bar{t}),\bar{\mathbf{z}}_i^{(\ell)},\bar{\omega}) = \frac{iE}{4\beta}H_0^{(1)}\left(\bar{\omega}\bar{r}\right) \tag{44}$$

Also note that

$$\bar{r} = \sqrt{\left[\mathbf{r}_i(\bar{t}) - \bar{\mathbf{z}}_i^{(\ell)}\right]_1^2/\beta^2 + \left[\mathbf{r}_i(\bar{t}) - \bar{\mathbf{z}}_i^{(\ell)}\right]_2^2} = \sqrt{\left[\mathbf{r}_i(\bar{t}) - \mathbf{r}_i(\bar{t}_\ell)\right]_1^2/\beta^2 + \left[\mathbf{r}_i(\bar{t}) - \mathbf{r}_i(\bar{t}_\ell)\right]_2^2}$$

$$\approx |\bar{t} - \bar{t}_\ell| \sqrt{[\mathbf{r}_i'(\bar{t}_\ell)]_1^2 / \beta^2 + [\mathbf{r}_i'(\bar{t}_\ell)]_2^2} \tag{45}$$

where $[\cdot]_1$ and $[\cdot]_2$ are the first and second vector components, respectively, of the term within the brackets. For small x, the asymptotic expansion for the zeroth-order Hankel function of the first kind gives

$$H_0^{(1)}(x) = J_0(x) + iY_0(x) = \frac{2i}{\pi} \ln(x)\, J_0(x) + \text{ smooth terms} \tag{46}$$

The "smooth terms" in equation (46) represent functions that are both analytic and infinitely differentiable (Appendix A). By (45), there is a logarithmic singularity present in (44) when $\bar{t} = \bar{t}_\ell$. To take care of this singularity, equation (44) can be rewritten as

$$\begin{aligned} G_0(\mathbf{r}_i(\bar{t}), \overline{\mathbf{z}}_i^{(\ell)}, \overline{\omega}) &= \frac{iE}{4\beta} \left[H_0^{(1)}(\overline{\omega}\overline{r}) - \frac{2i}{\pi} \ln(|\bar{t} - \bar{t}_\ell|)\, J_0(\overline{\omega}\overline{r}) \right] + \frac{iE}{4\beta} \frac{2i}{\pi} \ln(|\bar{t} - \bar{t}_\ell|)\, J_0(\overline{\omega}\overline{r}) \\ &\equiv G_0^{(\mathbf{A})}\left(\mathbf{r}_i(\bar{t}), \overline{\mathbf{z}}_i^{(\ell)}, \overline{\omega}\right) + G_0^{(\mathbf{B})}\left(\mathbf{r}_i(\bar{t}), \overline{\mathbf{z}}_i^{(\ell)}, \overline{\omega}\right) \ln(|\bar{t} - \bar{t}_\ell|) \end{aligned}$$

Then, the integral for a singular element becomes

$$\begin{aligned} \int_0^1 \Upsilon(\bar{t}) G_0(\mathbf{r}_i(\bar{t}), \overline{\mathbf{z}}_i^{(\ell)}, \overline{\omega})\, d\bar{t} &= \int_0^1 \Upsilon(\bar{t}) G_0^{(\mathbf{A})}\left(\mathbf{r}_i(\bar{t}), \overline{\mathbf{z}}_i^{(\ell)}, \overline{\omega}\right) d\bar{t} \\ &+ \int_0^1 \Upsilon(\bar{t}) G_0^{(\mathbf{B})}\left(\mathbf{r}_i(\bar{t}), \overline{\mathbf{z}}_i^{(\ell)}, \overline{\omega}\right) \ln(|\bar{t} - \bar{t}_\ell|)\, d\bar{t} \end{aligned} \tag{47}$$

The first integral on the right-hand-side of equation (47) is calculated using the Gauss-Legendre formula while the second integral is evaluated by Gaussian integration for integrands with a logarithmic singularity [1].

A similar approach is used for the singularity that arises in the normal derivative of the free-space Green's function when $j = i$. Denote $F = -E\left[\left(\mathbf{r}_i(\bar{t}) - \overline{\mathbf{z}}_i^{(\ell)}\right) \cdot \mathbf{n}\right] / \overline{r}$ so that equation (34) becomes

$$G_1(\mathbf{r}_i(\bar{t}), \overline{\mathbf{z}}_i^{(\ell)}, \overline{\omega}) = \frac{i\overline{\omega}F}{4\beta} H_1^{(1)}(\overline{\omega}\overline{r})$$

Again, applying the asymptotic expansion for the first order Hankel function of the first kind results in

$$\begin{aligned} G_1(\mathbf{r}_i(\bar{t}), \overline{\mathbf{z}}_i^{(\ell)}, \overline{\omega}) &= \frac{i\overline{\omega}F}{4\beta} \left[H_1^{(1)}(\overline{\omega}\overline{r}) - \frac{2i}{\pi} \ln(|\bar{t} - \bar{t}_\ell|)\, J_1(\overline{\omega}\overline{r}) \right] + \frac{i\overline{\omega}F}{4\beta} \frac{2i}{\pi} \ln(|\bar{t} - \bar{t}_\ell|)\, J_1(\overline{\omega}\overline{r}) \\ &\equiv G_1^{(\mathbf{A})}\left(\mathbf{r}_i(\bar{t}), \overline{\mathbf{z}}_i^{(\ell)}, \overline{\omega}\right) + G_1^{(\mathbf{B})}\left(\mathbf{r}_i(\bar{t}), \overline{\mathbf{z}}_i^{(\ell)}, \overline{\omega}\right) \ln(|\bar{t} - \bar{t}_\ell|) \end{aligned}$$

Any integrals on singular elements containing $G_1(\mathbf{r}_i(\bar{t}), \overline{\mathbf{z}}_i^{(\ell)}, \overline{\omega})$ are evaluated by quadratures as discussed previously for the case of the singularity in G_0.

Once the singularities are properly removed and the appropriate quadratures are applied, equation (33) can be solved for $G_B(\overline{\mathbf{z}}, \overline{\mathbf{y}}, \overline{\omega})$.

III.2 NUMERICAL SOLUTIONS OF THE CIRCULAR CYLINDER IN TWO DIMENSIONS

III.2.1 The Exact Green's Function and its Double Divergence

Once the expansion coefficients, $u_j^{(n)}$, in the linear system defined by equation (41) are found, the value of the exact Green's function at any field point $\bar{\mathbf{z}}$ located in the exterior domain is given by

$$\begin{aligned} G_B(\bar{\mathbf{z}},\bar{\mathbf{y}},\bar{\omega}) = G_0\left(\bar{\mathbf{y}},\bar{\mathbf{z}},\bar{\omega}\right) &- \sum_{j=1}^{N}\int_0^1 G_1(\mathbf{r}_j(\bar{t}),\bar{\mathbf{z}},\bar{\omega})\left[\sum_{n=0}^{P} u_j^{(n)}\phi_n(\bar{t})\right]\left|\mathbf{r}_j'(\bar{t})\right| d\bar{t} \\ &+\sum_{j=1}^{N}\int_0^1 i\omega U_n G_0(\mathbf{r}_j(\bar{t}),\bar{\mathbf{z}},\bar{\omega})\left[\sum_{n=0}^{P} u_j^{(n)}\phi_n(\bar{t})\right]\left|\mathbf{r}_j'(\bar{t})\right| d\bar{t} \\ &-\sum_{j=1}^{N}\int_0^1 U_n U_t G_0(\mathbf{r}_j(\bar{t}),\bar{\mathbf{z}},\bar{\omega})\left[\sum_{n=0}^{P} u_j^{(n)}\phi_n'(\bar{t})\right] d\bar{t} \end{aligned} \tag{48}$$

The double divergence of the exact Green's function is then calculated by taking spatial derivatives of equation (48). This results in

$$\begin{aligned} \frac{\partial^2}{\partial z_i \partial z_j} G_B(\bar{\mathbf{z}},\bar{\mathbf{y}},\bar{\omega}) &= \frac{\partial^2}{\partial z_i \partial z_j} G_0\left(\bar{\mathbf{y}},\bar{\mathbf{z}},\bar{\omega}\right) \\ &-\sum_{j=1}^{N}\int_0^1 \frac{\partial^2}{\partial z_i \partial z_j} G_1(\mathbf{r}_j(\bar{t}),\bar{\mathbf{z}},\bar{\omega})\left[\sum_{n=0}^{P} u_j^{(n)}\phi_n(\bar{t})\right]\left|\mathbf{r}_j'(\bar{t})\right| d\bar{t} \\ &+\sum_{j=1}^{N}\int_0^1 i\omega U_n \frac{\partial^2}{\partial z_i \partial z_j} G_0(\mathbf{r}_j(\bar{t}),\bar{\mathbf{z}},\bar{\omega})\left[\sum_{n=0}^{P} u_j^{(n)}\phi_n(\bar{t})\right]\left|\mathbf{r}_j'(\bar{t})\right| d\bar{t} \\ &-\sum_{j=1}^{N}\int_0^1 U_n U_t \frac{\partial^2}{\partial z_i \partial z_j} G_0(\mathbf{r}_j(\bar{t}),\bar{\mathbf{z}},\bar{\omega})\left[\sum_{n=0}^{P} u_j^{(n)}\phi_n'(\bar{t})\right] d\bar{t} \end{aligned} \tag{49}$$

Since $G_0\left(\mathbf{r}_j(\bar{t}),\bar{\mathbf{z}},\bar{\omega}\right)$ and $G_1(\mathbf{r}_j(\bar{t}),\bar{\mathbf{z}},\bar{\omega})$ are known functions, defined in equations (29) and (34) respectively, their spatial derivatives may be taken directly in order to calculate the double divergence. Equation (49) does not contain any logarithmic singularities because the field point, $\bar{\mathbf{z}}$, is not located on the boundary. Therefore, the integrals in equation (49) can theoretically be determined using Gaussian quadratures.

A problem arises, however, when dealing with a field point that is very close to the boundary of the circular cross-section. To illustrate this, consider the case where no mean flow is present, i.e., $M = 0$. Let $\overline{\mathbf{y}}$ denote $\mathbf{r}_j(\overline{t})$ for element j closest to the field point $\overline{\mathbf{z}}$. Then, the expression for G_0 given in equation (29) reduces to

$$G_0\left(\overline{\mathbf{y}}, \overline{\mathbf{z}}, \overline{\omega}\right) = \frac{i}{4} H_0^{(1)}(\overline{\omega}\overline{r}) \tag{50}$$

where

$$\overline{\omega} = \sqrt{\omega^2 - k_3^2}, \quad \overline{r} = \sqrt{(y_1 - z_1)^2 + (y_2 - z_2)^2} \equiv \sqrt{r_1^2 + r_2^2}$$

Using the Hankel function derivative defined in Appendix A, the partial second derivative of (50) with respect to z_1 is

$$\frac{\partial^2}{\partial z_1^2} G_0\left(\overline{\mathbf{y}}, \overline{\mathbf{z}}, \overline{\omega}\right) = -\frac{i\overline{\omega}^2}{8}\left[H_0^{(1)}(\overline{\omega}\overline{r}) - H_2^{(1)}(\overline{\omega}\overline{r})\right]\frac{r_1}{\overline{r}^2} - \frac{i\overline{\omega}}{4} H_1^{(1)}(\overline{\omega}\overline{r})\frac{r_2^2}{\overline{r}^3} \tag{51}$$

The other derivatives of G_0 and G_1 in equation (49) are similar to equation (51) in terms of the power of $\overline{r}$ in the denominator. When a field point is significantly close to the boundary, $\overline{r}$ is very small. This causes the integral kernels in equation (49) to become nearly singular on the element closest to the field point. To improve the accuracy of the double divergence, the interval of integration corresponding to the element closest to the field point is refined into subintervals that are grouped around the boundary point closest to the field point $\overline{\mathbf{z}}$. The integrals for each subinterval are then calculated using a 20-point Gaussian quadrature.

The nearly singular integral kernels caused by the small distance between field point and element increase the error in the solution $u_j^{(n)}$. Consequently, the order P of the basis functions used when calculating the double divergence must exceed the order of those used to calculate the exact Green's function to maintain the same accuracy. In the case of the two-dimensional circular cylinder, the exact solution for $M = 0$ is well known and therefore it is utilized in this chapter as the basis of comparison [5]. Fig. 4 compares the numerical results of the Green's function obtained when computed with basis functions of order $P = 2, 3, 5$ to the exact solution. Similar results are given in Fig. 5 for one component of the double divergence. Both figures show accurate numerical results except for the case of the double divergence term when $P = 2$ and $P = 3$ for field points close to the boundary. In order to retain the desired accuracy of the numerical results for these close points, Fig. 5 shows that the order of the basis polynomials must be increased, in this example, to $P = 5$. Since the basis polynomial order can easily be changed in the spectral collocation method, it is an advantageous method for this problem.

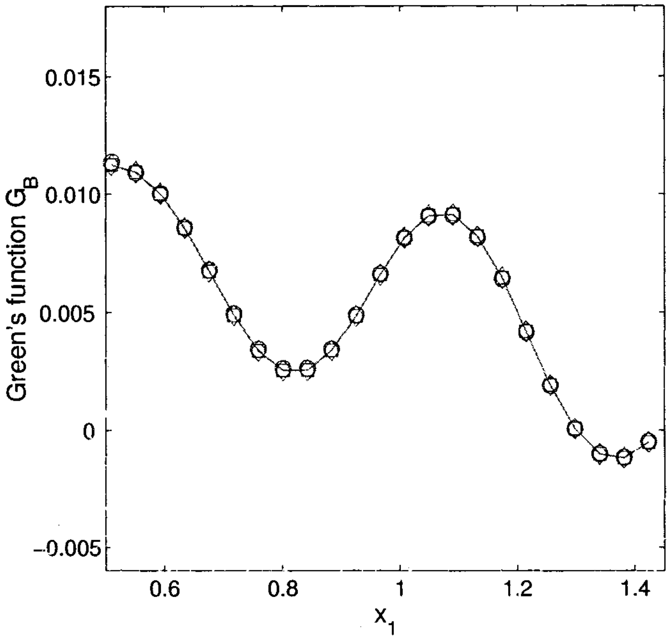

Fig. 4: The computed Green's function along line $x_2 = 0$. The order of basis functions is: Circles: $P = 2$; Squares: $P = 3$; Diamonds: $P = 5$. Solid line is exact solution, $\omega = 4\pi$, $N = 16$.

III.2.2 Demonstration of Exponential Convergence

Spectral methods are known to have exceptionally fast convergence rates when the solution is infinitely smooth [21]. As the order of basis polynomials is increased in the spectral collocation method, the interval between grid points becomes smaller. This interval is $O(1/P)$, where P is the number of collocation points. Hence the collocation error is approximately $O\left[(1/P)^P\right]$. This is called exponential convergence or spectral accuracy [7].

Table I demonstrates the spectral accuracy of the collocation method when $M = 0$ and $M = 0.2$. The relative errors are calculated by subtracting the exact solution from the numerical solution, then taking the modulus of this result and dividing by the modulus of the exact solution. Both the Green's function and its second derivative with respect to x_1 are included in Table I. Because an exact solution is not available for the case when $M = 0.2$, the basis of comparison was chosen to be the numerical results obtained when $P = 15$. A graphical representation of the data in Table I can be found in Fig. 6 and Fig. 7. It is clear from both figures that

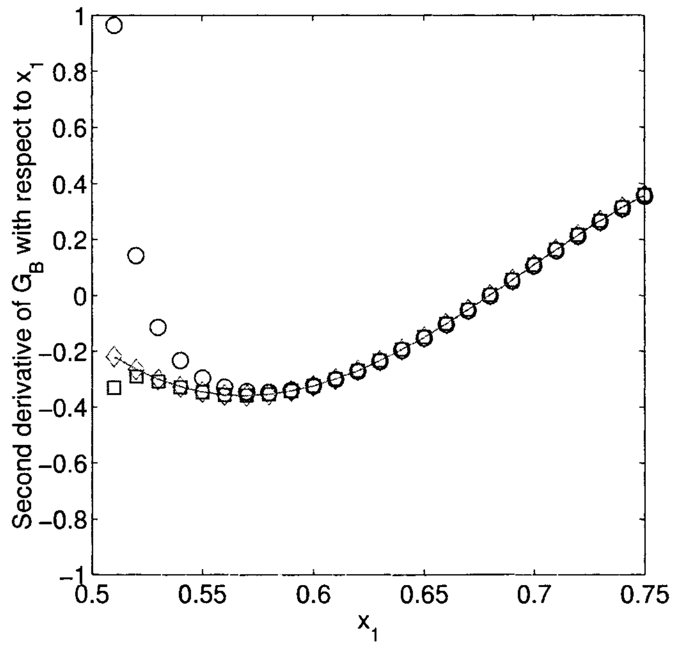

Fig. 5: The computed second derivative of Green's function with respect to x_1 along line $x_2 = 0$. The order of basis functions is: Circles: $P = 2$; Squares: $P = 3$; Diamonds: $P = 5$. Solid line is exact solution, $\omega = 4\pi$, $N = 16$.

exponential convergence is achieved as the order of the basis polynomials is increased. Table I also illustrates that for point A close to the boundary, the error in the second derivative of the Green's function is larger than that of the Green's function itself. This is a result of the nearly singular integral kernels discussed in section III.2.1.

III.3 ADVANTAGES OF THE SPECTRAL COLLOCATION BEM

III.3.1 Spectral Collocation Versus Traditional Boundary Element Methods

Some discussion of boundary element methods versus finite difference and finite element methods took place in section III.1.1. Because the spectral collocation BEM also requires only boundary discretization and uses an exact Green's function that satisfies the radiation condition at infinity, it enjoys the same advantages over FDM and FEM. The benefits of using the spectral collocation BEM instead of traditional boundary element methods are discussed in this section.

In most cases, either constant elements or linear elements are used to compute

Table I: Relative errors of exact Green's function and its second derivative with respect to x_1 as the order P increases. The number of elements is $N = 16$ and the frequency is 4π. The mean flow Mach number is (a) $M = 0$ and (b) $M = 0.2$.

(a)$M = 0$

Order P	Point A G_B	$\bar{\mathbf{z}} = (0.51, 0)$ $\frac{\partial^2 G_B}{\partial x_1^2}$	Point B G_B	$\bar{\mathbf{z}} = (0.75, 0)$ $\frac{\partial^2 G_B}{\partial x_1^2}$
1	0.103559	7.58349	0.0163570	0.0117968
2	0.00721318	4.14877	0.00685089	0.00848532
3	0.000238121	0.396582	0.000282042	0.000314223
5	$5.70406E-06$	0.00327423	$4.08753E-07$	$5.87232E-07$
7	$6.38074E-09$	$8.17761E-07$	$2.30121E-09$	$1.72398E-09$
9	$3.76160E-10$	$1.61418E-07$	$6.35161E-12$	$5.00634E-12$

(b) $M = 0.2$

Order P	Point A G_B	$\bar{\mathbf{z}} = (0.51, 0)$ $\frac{\partial^2 G_B}{\partial x_1^2}$	Point B G_B	$\bar{\mathbf{z}} = (0.75, 0)$ $\frac{\partial^2 G_B}{\partial x_1^2}$
1	0.152124	11.6325	0.0525078	0.168418
2	0.00177218	6.15391	0.0128685	0.00741143
3	0.000331913	0.615260	0.000615142	0.000514647
5	$4.63184E-06$	0.00642613	$3.89132E-06$	$6.72918E-06$
7	$1.07052E-08$	$1.69364E-05$	$6.10549E-08$	$1.08555E-07$
9	$2.41123E-09$	$1.89208E-06$	$7.79234E-10$	$2.30800E-09$

unknowns in the traditional BEM. In the constant element method, the "nodes" are taken to be in the middle of the element and the basis functions are assumed to be constant over each element. For linear elements, the nodes are at the ends of the element and the basis function is assumed to be linear over the element. If higher accuracy is desired, quadratic elements can be used, in which two nodes are at the ends of each element and one node is in the middle. In general, the accuracy of the method increases with the number of nodes per element. The spectral collocation BEM allows the use of high-order basis functions to approximate the unknown function. Since discontinuous boundary elements are used, the order of the basis functions can be changed easily, without reformulation of the problem. High-order basis functions are beneficial because they accurately approximate the tangential derivative of the unknown function in the presence of the mean flow.

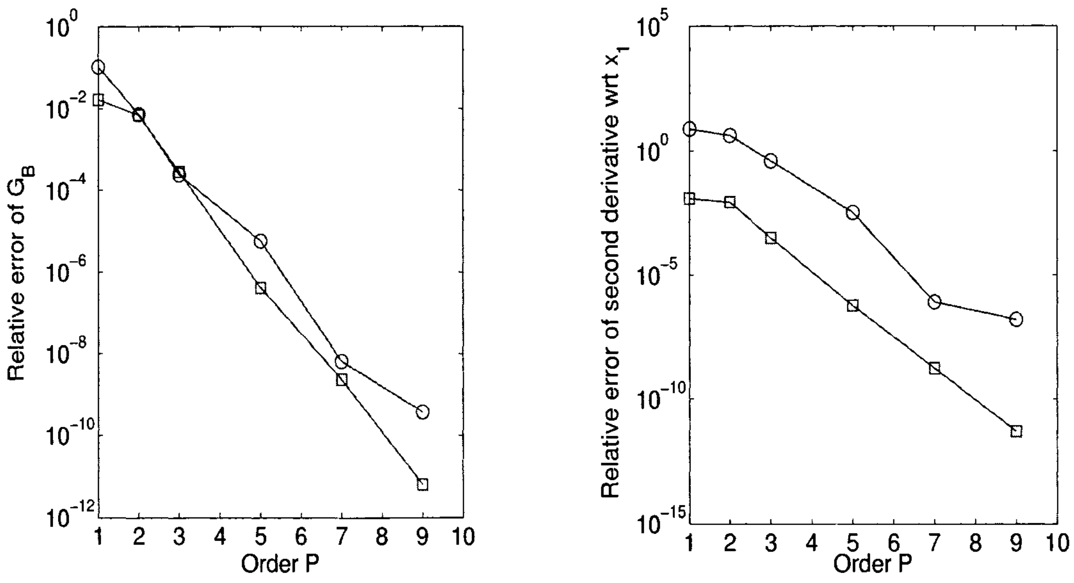

Fig. 6: Relative error as a function of the order of basis polynomials for $M = 0$. Circles: $\overline{\mathbf{z}} = (0.51, 0)$; Squares: $\overline{\mathbf{z}} = (0.75, 0)$.

By choosing Chebyshev polynomials as the basis functions along with the interior Gauss-Chebyshev collocation points, two more advantages arise. First, the accuracy of the solution can be assessed by the magnitudes of the expansion coefficients, $u_j^{(n)}$. The error approximating a function by its first N-terms using Chebyshev polynomials is bounded by the sum of the absolute values of the coefficients of the remaining terms in the series [7]. Also, since the Gauss-Chebyshev points are interior, no collocation point will fall on a corner as long as every corner lies on an element end-point. Therefore, evaluation of the BIE on corner points is avoided. With the correct choice of basis functions and collocation points, the spectral collocation BEM will always achieve spectral accuracy for smooth boundaries [7].

Compared to the traditional BEM, the spectral collocation BEM produces smaller matrices because it requires fewer nodal points to maintain the same accuracy [21]. As a result, the latter method requires less computation time. In both cases, the matrices generated are dense. Thus, the spectral collocation BEM is the better choice when dealing with smooth boundaries.

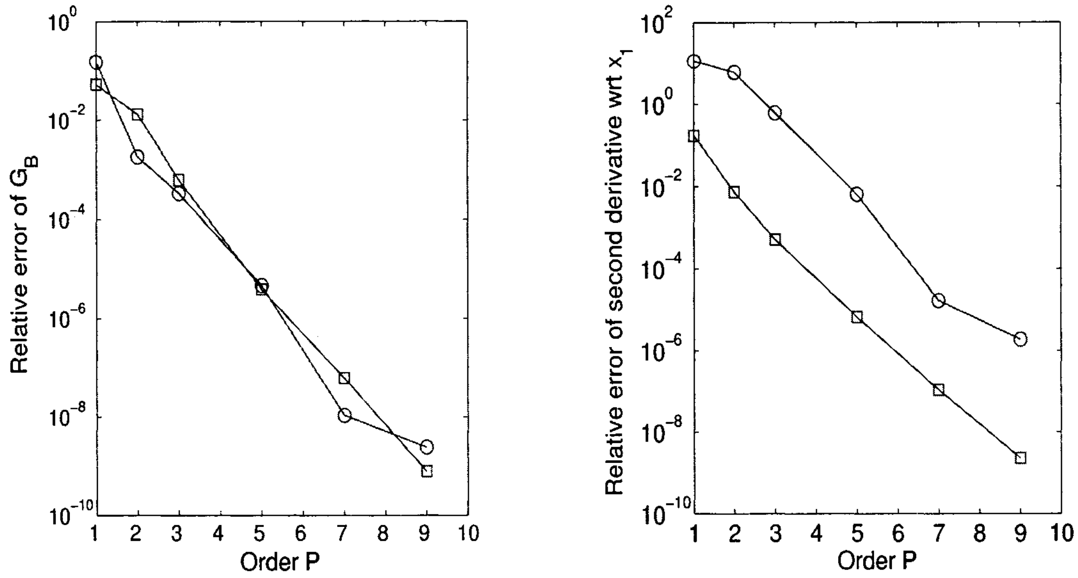

Fig. 7: Relative error as a function of the order of basis polynomials for $M = 0.2$. Circles: $\overline{\mathbf{z}} = (0.51, 0)$; Squares: $\overline{\mathbf{z}} = (0.75, 0)$.

III.3.2 Nodes per Wavelength Calculation

One way to demonstrate the benefit of using high-order basis functions is to perform a "nodes per wavelength" calculation. This is done by using the equation

$$NPW = \frac{\overline{N}}{N_w} \tag{52}$$

In equation (52), $\overline{N} = N(P+1)$ where N is the number of elements and P is the order of the basis functions. Hence, $\overline{N}$ is the total number of collocation points, or nodes, on arc length L. N_w is defined as the total number of waves on arc length L and is given by

$$N_w = \frac{L}{\lambda}$$

where $\lambda = \frac{2\pi}{\kappa}$ for a given wavenumber κ.

Consider again the circular cylinder with constant cross-section of radius 0.5, and choose twenty equally spaced field points for a given radius. For each basis function order, the number of elements is increased until a combined maximum allowable relative error of 0.005 is reached when compared with the exact solution for $M = 0$ and frequency 40π. Tables II and III contain required nodes per wavelength results for field points at radii 0.51 and 0.75 respectively. The computation time required for each calculation is also included in Tables II and III. According to Tables II and

Table II: Nodes per wavelength and computation time required for a maximum relative error of 0.005 as the order of the basis polynomial P increases. The frequency is 40π and the mean flow Mach number is $M = 0$. Results for 20 field points at radius 0.51 for (a) Green's function and (b) its second derivative with respect to x_1 are shown.

(a)Green's Function

Order P	Nodes per Wavelength	Computation Time (seconds)
1	60.4789	535.1094
2	13.6077	29.5313
3	6.8755	12.5156
5	5.7296	11.8281
7	4.9656	14.6406
9	4.7746	15.9375
11	4.3927	17.7813

(b)Second derivative of Green's Function with respect to x_1

Order P	Nodes per Wavelength	Computation Time (seconds)
1	66.8451	689.6875
2	14.2762	32.2813
3	7.8304	15.4219
5	6.3025	15.4063
7	5.0930	13.7188
9	4.9338	15.9531
11	4.5837	18.1563

III, the computation time for field points at radius 0.51 is always greater for the same order than that for field points at radius 0.75. This is due to the computation time necessary for refinement of the integration intervals for a field point located close to the boundary, as discussed in section III.2.1. Also, in each table there is an optimal order in terms of computation time that does not correspond to the highest order of basis functions. This is a result of the number of quadrature points, $2(P+1)$, required to compute each integral in equations (40), (48) and (49).

Table III: Nodes per wavelength and computation time required for a maximum relative error of 0.005 as the order of the basis polynomial P increases. The frequency is 40π and the mean flow Mach number is $M = 0$. Results for 20 field points at radius 0.75 for (a) Green's function and (b) its second derivative with respect to x_1 are shown.

(a)Green's Function

Order P	Nodes per Wavelength	Computation Time (seconds)
1	49.9747	314.8594
2	12.3186	17.3594
3	6.6845	6.7031
5	5.6341	7.3281
7	4.9656	7.8906
9	4.7746	9.3281
11	4.3927	9.9219

(b)Second derivative of Green's Function with respect to x_1

Order P	Nodes per Wavelength	Computation Time (seconds)
1	66.8451	665.8281
2	14.2285	22.7344
3	7.7031	8.5938
5	5.7296	7.2813
7	5.0929	7.9531
9	4.775	9.0156
11	4.5837	10.2656

III.4 COMPUTATION OF DOUBLE DIVERGENCE

III.4.1 Two Approaches

All spatial second derivative calculations of the exact Green's function thus far have been performed using direct differentiation. For most near-field points, direct differentiation is preferred over a finite difference approximation since the latter results in additional discretization errors. However, as previously discussed, the integral kernels in the double divergence equation are nearly singular for a field point very close to the boundary. For these close points, a finite difference approximation, which depends only on the values of the exact Green's function at and closely surrounding the field point, may yield better results. This section contains a comparison between the direct computation and a finite difference approximation of the double divergence.

III.4.2 Finite Difference Approach

Since the double divergence of the exact Green's function is already extremely accurate when using high-order basis functions with direct differentiation, the finite difference approach was applied only to basis function orders of $P = 2$ and $P = 3$. Indeed, finite difference calculations applied to orders $P = 5$ and $P = 7$ yielded much worse results than direct differentiation. Two finite difference stencils were applied to several field points located at a radius of 0.51 from the center of a circle of radius 0.5. The schemes used were a fourth-order central scheme given by

$$\begin{aligned}\frac{\partial^2 G_B}{\partial x_1^2}(x_1, x_2) = [&-G_B(x_1 + 2\Delta x, x_2) + 16G_B(x_1 + \Delta x, x_2) - 30G_B(x_1, x_2) \\ &+16G_B(x_1 - \Delta x, x_2) - G_B(x_1 - 2\Delta x, x_2)]/12\Delta x^2 \qquad (53)\end{aligned}$$

and a fourth-order forward scheme given by

$$\begin{aligned}\frac{\partial^2 G_B}{\partial x_1^2}(x_1, x_2) = [&11G_B(x_1, x_2) - 20G_B(x_1 + \Delta x, x_2) + 6G_B(x_1 + 2\Delta x, x_2) \\ &+4G_B(x_1 + 3\Delta x, x_2) - G_B(x_1 + 4\Delta x, x_2)]/12\Delta x^2 \qquad (54)\end{aligned}$$

In the central scheme, the finite difference approximation was computed using $\Delta x = 0.0005$. In the forward scheme, the computation was done using $\Delta x = 0.005$.

III.4.3 Results of Comparison

Tables IV and V contain direct differentiation and finite difference relative errors for the second derivative of the exact Green's function with respect to x_1 at seven field points close to the boundary for basis function orders $P = 2$ and $P = 3$ respectively. The Mach number is $M = 0$, the frequency is 4π and the source point is located at $\bar{\mathrm{y}} = (0, -20)$. The exact solution was used as the basis of comparison. The results in Tables IV and V show that the errors corresponding to the finite difference calculations are on the same order of magnitude as the errors corresponding to direct differentiation. There is no significant improvement when using either the central

Table IV: Comparison of relative errors of the exact Green's function second derivative with respect to x_1 using direct differentiation and finite difference schemes for basis function order $P = 2$. Results are for field points located at radius 0.51 from circle. The number of boundary elements is $N = 16$ and the frequency is 4π. The mean flow Mach number is $M = 0$.

Point Location $\bar{\mathbf{z}} = (x_1, x_2)$	Direct Differentiation Error	Central Scheme Error	Forward Scheme Error
$\bar{\mathbf{z}} = (0.3465, 0.375)$	0.992146	0.998845	0.889330
$\bar{\mathbf{z}} = (0.4445, 0.25)$	0.143219	0.148863	0.0885821
$\bar{\mathbf{z}} = (0.4944, 0.125)$	0.591835	0.598842	0.538544
$\bar{\mathbf{z}} = (0.51, 0)$	4.14877	4.16904	2.24344
$\bar{\mathbf{z}} = (0.4944, -0.125)$	1.77300	1.79780	1.52710
$\bar{\mathbf{z}} = (0.4445, -0.25)$	0.066288	0.0685527	0.0832171
$\bar{\mathbf{z}} = (0.3465, -0.375)$	0.249394	0.250747	0.225164

Table V: Comparison of relative errors of the exact Green's function second derivative with respect to x_1 using direct differentiation and finite difference schemes for basis function order $P = 3$. Results are for field points located at radius 0.51 from circle. The number of boundary elements is $N = 16$ and the frequency is 4π. The mean flow Mach number is $M = 0$.

Point Location $\bar{\mathbf{z}} = (x_1, x_2)$	Direct Differentiation Error	Central Scheme Error	Forward Scheme Error
$\bar{\mathbf{z}} = (0.3465, 0.375)$	0.0977817	0.102762	0.160943
$\bar{\mathbf{z}} = (0.4445, 0.25)$	0.194022	0.202099	0.151711
$\bar{\mathbf{z}} = (0.4944, 0.125)$	0.0236351	0.0319770	0.0612550
$\bar{\mathbf{z}} = (0.51, 0)$	0.396582	0.416727	0.280754
$\bar{\mathbf{z}} = (0.4944, -0.125)$	0.0639322	0.0909046	0.165914
$\bar{\mathbf{z}} = (0.4445, -0.25)$	0.0785330	0.0818204	0.0207737
$\bar{\mathbf{z}} = (0.3465, -0.375)$	0.0254311	0.0295269	0.0909827

or forward finite difference scheme for orders $P = 2$ and $P = 3$ in lieu of the direct differentiation results. Therefore, direct differentiation of the exact Green's function at all points, even those very close to the boundary, is preferred over finite difference calculations.

CHAPTER IV

APPLICATION OF SPECTRAL COLLOCATION BEM TO NON-SMOOTH BOUNDARIES

IV.1 GENERAL DISCUSSION OF CORNER SINGULARITIES

The spectral collocation boundary element method is very successful when applied to problems with smooth boundaries. However, when sharp angles or corners are introduced into the boundary, the spectral collocation method alone will not result in exponential convergence because of the solution singularities at these locations. The exact Green's function ceases to be analytic on corner elements, and therefore, it cannot be adequately represented by Chebyshev polynomials. In fact, most standard methods for solving boundary value problems provide slow convergence and inaccurate solutions in the neighborhood of a corner [31].

IV.1.1 Nature of Corner Singularities

In polar coordinates, the asymptotic expansion of a singular solution to an elliptic equation at a corner is given by

$$g_s(r,\theta) \sim \sum_{p=0}^{\infty} a_p g_p(r,\theta)$$

where

$$g_p(r,\theta) = \sum_{q=0}^{N} r^{\lambda+p} \left(\log^q r\right) \phi_{p,q}(\theta) \tag{55}$$

In equation (55), λ is a singularity exponent and $\phi_{p,q}(\theta)$ are smooth angular functions [31]. The singularity exponents depend on the boundary conditions prescribed at the corner. For the case of a two-dimensional exterior domain governed by a Helmoltz equation with homogeneous Neumann boundary conditions on the corner edges, the expansion shown in equation (55) becomes

$$g_s(r,\theta) \sim \sum_{p=0}^{\infty} a_p g_p(r,\theta) = \sum_{p=0}^{\infty} a_p J_{pv}\left(krf(\theta)\right) \cos(\sigma) \tag{56}$$

where $v = \frac{\pi}{\varphi}$, φ is related to the exterior angle of the corner and σ is a function of θ [31].

For $\mathrm{Re}(pv) \geq 0$, the Bessel function of the first kind in equation (56) can be approximated by its asymptotic expansion for $z \to 0$ as

$$J_{pv}(z) \sim \frac{1}{\Gamma(pv+1)}\left(\frac{z}{2}\right)^{pv} = C_p z^{pv} \tag{57}$$

where $z = krf(\theta)$. Since v is not always an integer, the singular solution given in equation (56) could contain irrational expressions of r, which are not analytic in the entire complex z-plane. The convergence of a spectral series for a function is controlled by the "singularities" of that function [7]. The term "singularities" includes poles, fractional powers, branch points, and discontinuities of the function or its derivatives.

IV.1.2 Techniques for Reducing Errors Caused by Corner Singularities

Numerous works have investigated methods for treating corner singularities in potential theory problems. Telukunta and Mukherjee [41] developed an Extended Boundary Node Method (EBNM), which is a combination of the Moving Least Squares approximation scheme and the standard BIE method. This method is successful in modeling corner singularities, however, approximations for the normal derivatives of the potential function must be made at each corner. These approximations depend on the interior angle of each corner. For an object with several different corners, such as the high-lift wing depicted in Fig. 1, this method may require much more computational effort when compared with standard BEM techniques. A more common approach involves the use of singular elements that require the orders of the singularities to be included at the corresponding singular nodes. Ong and Lim [33] successfully applied this method to three-dimensional potential problems, showing that singular elements can significantly improve the accuracy of solutions to some electrostatic problems. The drawback to this method is the development of singular shape functions that must closely approximate the actual singular fields. In a multi-cornered object, this may appreciably increase the computational effort involved in obtaining an accurate solution. Another technique used to alleviate corner singularities incorporates complex mapping into the BEM. This method has been explored by Wang and Tsay [42] as well as by Boyd [8]. Boyd applied a Mercator coordinate transformation to map corners to infinity and noted that any reasonable basis set applied to the infinite interval will yield a spectral series that converges exponentially. However, this convergence is subgeometric, meaning the error is proportional to $\exp(-q\sqrt{P})$ where P is the number of basis functions.

A fourth technique developed in recent years by Igarashi and Honma [24] and Marin et al. [31] entails subtracting the singularities from the original potential function, leaving a "regularized" potential function to be determined by a standard BEM. New boundary integral equations are formulated to determine the expansion coefficients at the singular points. For a unique solution of the regular problem, additional constraints equal in number to each singular solution must be specified. As in the previously discussed methods, the corner angle must be known for the application of this method. These singularities behave like $r^{(p\alpha)}$ for $p = 0, 1, 2, \ldots$, as shown in equation (57). Consider the case of the two-dimensional Helmholtz problem with singular solution expansion defined in equation (56) with $\alpha = \frac{1}{2}$. If, for example, a fourth-order accuracy is needed, i.e., $p = 0, 1, 2, 3, 4$, the Bessel function expansions give, in terms of r,

$$C_0, C_1 r^{\frac{1}{2}}, C_2 r, C_3 r^{\frac{3}{2}}, C_4 r^2 \text{ or } \mathrm{C_0, C_1 r^{\frac{1}{2}}, C_2 r, C_3 r^{\frac{1}{2}} r, C_4 r^2}$$

In this example, the second and fourth terms have in common a function "singularity" on the order of $r^{\frac{1}{2}}$ while the other three terms contain rational functions of r. Hence, only one singularity needs to be subtracted from the original problem. Next, consider a similar example where $\alpha = \frac{3}{4}$. Then, for fourth-order accuracy, the terms are

$$C_0, C_1 r^{\frac{3}{4}}, C_2 r^{\frac{3}{2}}, C_3 r^{\frac{9}{4}}, C_4 r^3$$

The fractional exponents in terms two through four cannot be manipulated so that these terms will have a common functional singularity. Therefore, each term must be subtracted individually, resulting in more computational effort due to the specification of more constraints.

One of the most successful techniques for treating corner singularities is the h-version refinement method. In this approach, the number of basis functions remains constant, while the number of elements in the neighborhood of the singularity is increased. Even though the total number of elements is increased in this method, the corner elements containing the function singularities become a smaller percentage of the boundary. In general, a power convergence rate is obtained when the h-version is applied in solving a Helmholtz equation problem, i.e., if h is the element size, the error decreases as $h^{(P+1)}$ for $h \to 0$, where P is the order of the basis functions [25]. One advantage of element refinement methods is that no prior knowledge of singularity behavior is required. Only the locations of the singularities must be known. This property, along with the convergence rate, makes the h-version refinement method a more robust approach for dealing with changes in geometry.

In subsequent sections, two methods of improving errors caused by corner singularities are applied to a square object: an exponential grading element refinement technique and a collocation method based on Sinc functions. Each approach is discussed in detail in subsequent sections of this paper.

IV.2 RESULTS OF SPECTRAL COLLOCATION BEM ON A SQUARE BOUNDARY

In order to illustrate the slow convergence of the spectral collocation BEM applied to non-smooth boundaries, consider a square centered at the origin with corners located at $(0.5, 0.5)$, $(0.5, -0.5)$, $(-0.5, -0.5)$ and $(-0.5, 0.5)$. The elements on the square boundary are configured so that all corners are located at element endpoints. Again, the collocation points are chosen to be the interior Gauss-Chebyshev points so there will be no evaluation of the BIE on the corner points. Each shape function, $\mathbf{r}_j(t)$, is approximated by a cubic spline connecting grid points on the boundary with continuous tangential derivatives on smooth boundaries. The two field points analyzed will be (A) $\overline{\mathbf{z}} = (0.51, 0)$ and (B) $\overline{\mathbf{z}} = (0.75, 0)$. The source point is located at $\overline{\mathbf{y}} = (0, -20)$, the frequency is $\omega = 4\pi$ and the number of elements is $N = 16$.

Table VI shows the relative errors for the Green's function, G_B, and its second derivative, $\frac{\partial^2 G_B}{\partial x_1^2}$, when compared with a high order ($P = 15$) solution. The data for Table VI are also plotted in Fig. 8.

Table VI and Fig. 8 show that a non-exponential rate of decay occurs as the order of the basis polynomials increases. In the attempt to improve these results, an exponential grading element refinement will be performed on all corner elements.

IV.3 EXPONENTIAL GRADING ELEMENT REFINEMENT

IV.3.1 Definition of Element Refinement

This section introduces an exponential grading element refinement that will be applied to the square boundary described in section IV.2. This refinement is illustrated in Fig. 9. The refinement ratio, ν, is defined as

Table VI: Relative errors of exact Green's function and its second derivative with respect to x_1 as the order P increases. The number of elements on the square's boundary is $N = 16$ and the frequency is 4π. The mean flow Mach number is $M = 0$.

Order	Point A	$\bar{\mathbf{z}} = (0.51, 0)$	Point B	$\bar{\mathbf{z}} = (0.75, 0)$
P	G_B	$\frac{\partial^2 G_B}{\partial x_1^2}$	G_B	$\frac{\partial^2 G_B}{\partial x_1^2}$
1	0.0973225	133.980	0.0353173	1.30873
2	0.0392499	120.398	0.0308039	1.09711
3	0.00272320	10.4763	0.00212314	0.0704248
5	0.000510972	0.183188	0.000371261	0.00917916
7	0.000231130	0.00350694	0.000170683	0.00394068
9	0.000119278	0.00197095	0.0000890705	0.00197641

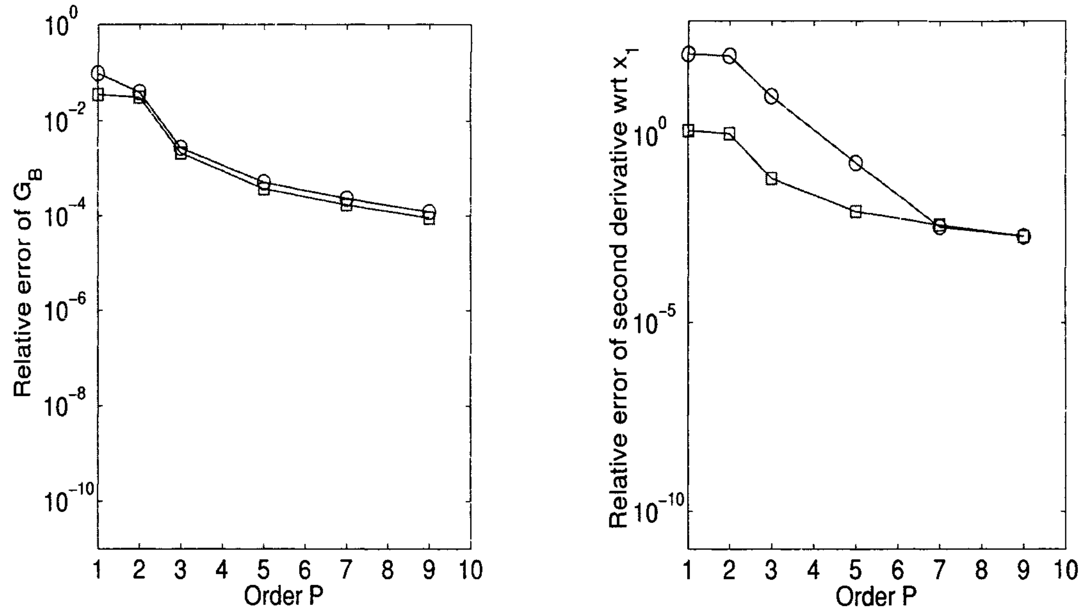

Fig. 8: Relative error as a function of the order of basis polynomials for square boundary with $M = 0$. Circles: $\bar{\mathbf{z}} = (0.51, 0)$; Squares: $\bar{\mathbf{z}} = (0.75, 0)$.

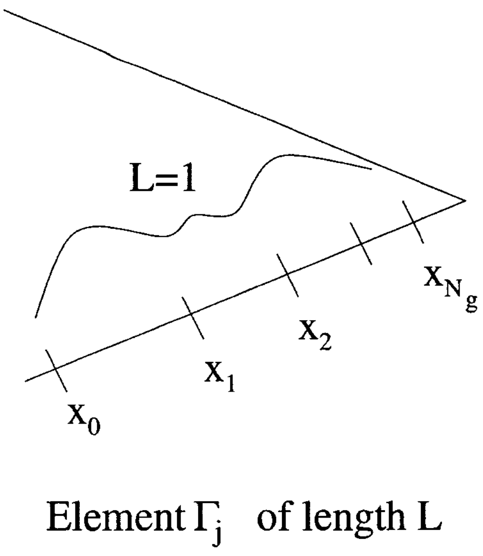

Fig. 9: Diagram showing definition of element refinement.

$$\nu = \frac{x_i}{x_{i-1}}$$

and N_g is the level of refinement, or number of refinements. The value of ν is in $(0, 1]$ where $\nu = 1$ would produce the original number of elements. This refinement is applied to each element containing a corner point.

IV.3.2 Results for a Fixed Refinement Ratio

Consider the 16-element square, and let the refinement ratio be a fixed value, $\nu = 0.35$. Although N_g does not depend on the order of the basis functions, P, for this example the refinement level was chosen to be $N_g = P + 2$. In order to compare the results of this refinement method with previous non-refinement results, the same field points, (A) $\overline{\mathbf{z}} = (0.51, 0)$ and (B) $\overline{\mathbf{z}} = (0.75, 0)$, are considered. The frequency is 4π and the source point location is $\overline{\mathbf{y}} = (0, -20)$. Table VII shows the relative errors for the Green's function, G_B, and its second derivative, $\frac{\partial^2 G_B}{\partial x_1^2}$, when compared with an order $P = 15$ solution for $M = 0$. The results of Table VII are plotted in Fig. 10. For a refinement of $\nu = 0.35$ and $N_g = P + 2$, exponential convergence is obtained.

IV.3.3 Optimal Refinement Strategy

To determine an optimal refinement strategy, many values of ν and N_g were tested. Clearly, for values of ν very close to one, the number of refinements would have to

Table VII: Relative errors of exact Green's function and its second derivative with respect to x_1 as the order P increases. The frequency is 4π, $\nu = 0.35$ and $N_g = P+2$. The mean flow Mach number is $M = 0$.

Order	Point A	$\bar{\mathbf{z}} = (0.51, 0)$	Point B	$\bar{\mathbf{z}} = (0.75, 0)$
P	G_B	$\frac{\partial^2 G_B}{\partial x_1^2}$	G_B	$\frac{\partial^2 G_B}{\partial x_1^2}$
1	0.0763597	132.533	0.0188810	1.23859
2	0.0584410	139.445	0.0300076	1.09480
3	0.000764934	21.4354	0.000255573	0.0510741
5	0.000161642	2.35153	0.0000276648	0.00172533
7	0.0000118897	0.0801876	$2.51755E-06$	0.000184259
9	$3.57358E-07$	0.0000460827	$3.91149E-08$	$3.45152E-06$
11	$7.31339E-09$	0.0000895887	$6.93006E-10$	$2.67518E-08$

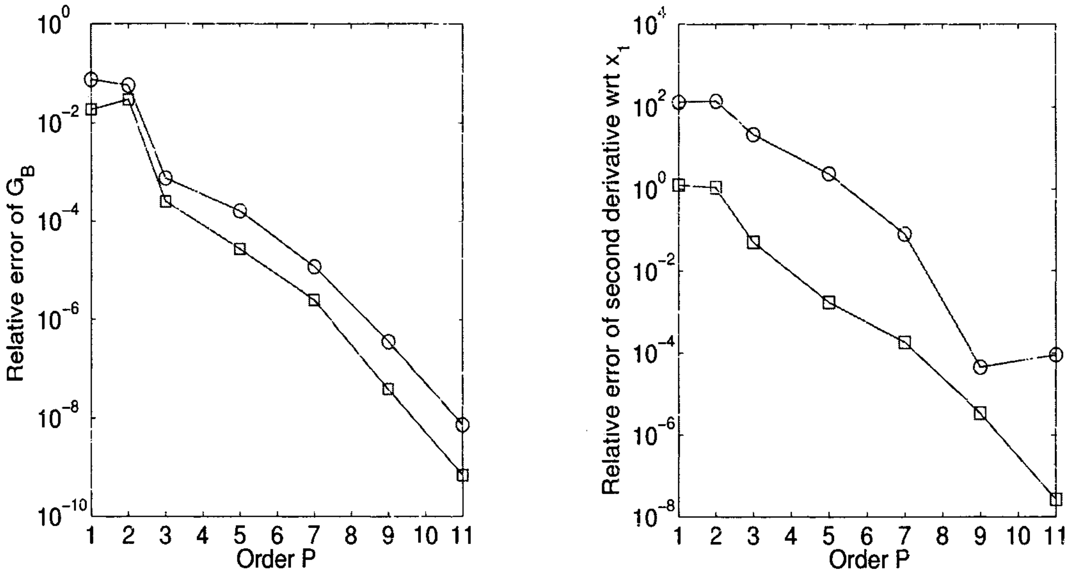

Fig. 10: Relative error as a function of the order of basis polynomials for square boundary with $M = 0$. Element refinement with $\nu = 0.35$ and $N_g = P + 2$. Circles: $\bar{\mathbf{z}} = (0.51, 0)$; Squares: $\bar{\mathbf{z}} = (0.75, 0)$.

Table VIII: Relative errors of the Green's function using exponential grading element refinement for the square boundary. The frequency is 4π, the mean flow Mach number is $M = 0$ and the source point is located at $\overline{\mathbf{y}} = (0, -20)$.

Level of Refinement	$\nu = 0.85$	$\nu = 0.5$	$\nu = 0.35$
$N_g = 2$	$6.30136E-05$	$2.01483E-05$	$1.07959E-05$
$N_g = 3$	$5.24537E-05$	$1.14010E-05$	$5.53004E-06$
$N_g = 4$	$4.39122E-05$	$7.59983E-06$	$3.73803E-06$
$N_g = 5$	$3.70199E-05$	$5.85945E-06$	
$N_g = 6$	$3.14598E-05$		
$N_g = 7$	$2.69720E-05$		

be large for the method to be effective. Since an increase in N_g causes an increase in the number of unknowns, this would not be computationally efficient. Therefore, lower levels of refinement are preferred.

Consider again the square boundary. Table VIII illustrates the effects of changing ν and N_g. The order of the basis functions was kept constant ($P = 7$) for this comparison. According to Table VIII, as the value of ν increases, more levels of refinement are required to obtain a specific accuracy. Another strategy to determine the best refinement is to keep the length of the refined corner elements constant. For an original corner element of length $L = 1$, the length of the refined corner element is given by ν^{N_g}. Two values for the length of the refined corner element were tested, (a) $\nu^{N_g} \approx 0.05$ and (b) $\nu^{N_g} \approx 0.008$. The results are shown in Fig. 11 and Fig. 12 for field point $\overline{\mathbf{z}} = (0.75, 0)$. Fig. 11 shows that for all values of ν and N_g, the results for both G_B and $\frac{\partial^2 G_B}{\partial x_1^2}$ are improved over the results of no refinement. Additionally, the element refinement relative errors given in Fig. 11 possess roughly equivalent orders of magnitude for each value of P. However, according to Fig. 12, $\nu = 0.09$ with $N_g = 2$ gives the largest errors for both the Green's function and its second derivative. In this case, the first level of refinement, $N_g = 1$, creates a new element with an endpoint too close to the corner, resulting in an inaccurate solution estimation on that element. This example clearly shows that there is a minimum as well as a maximum value for the refinement ratio.

Finally, to illustrate the applicability of the refinement strategy to any boundary with corners, consider an isosceles triangle boundary with corners located at $(0.5, 0.5)$,

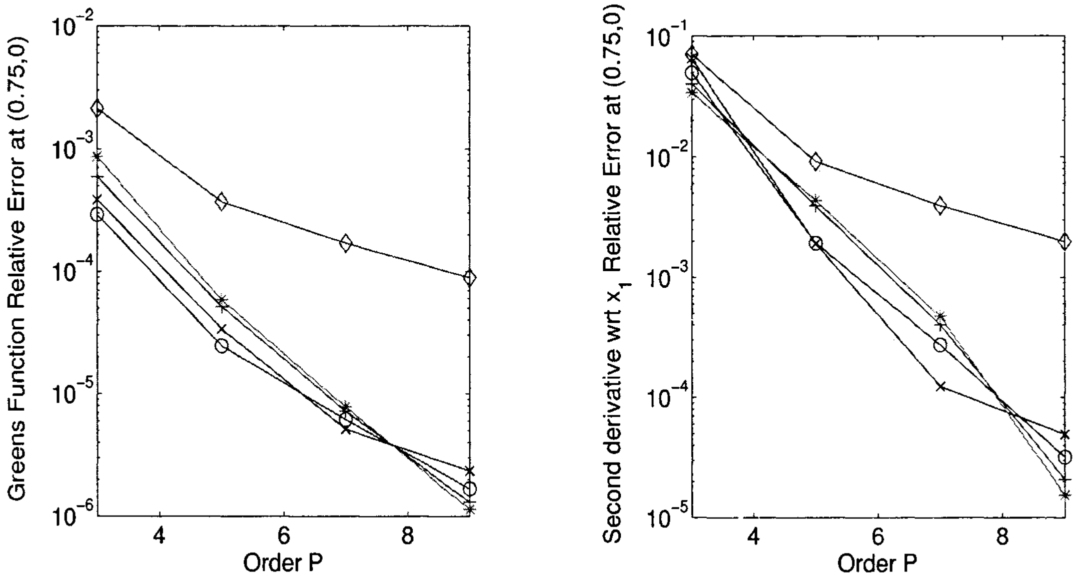

Fig. 11: Relative error as a function of the order of basis polynomials for square boundary with $M = 0$. Element refinement with $\nu^{N_g} \approx 0.05$. Cross: $\nu = 0.223$ and $N_g = 2$; Circle: $\nu = 0.37$ and $N_g = 3$; Plus: $\nu = 0.55$ and $N_g = 5$; Star: $\nu = 0.65$ and $N_g = 7$; Diamond: No element refinement.

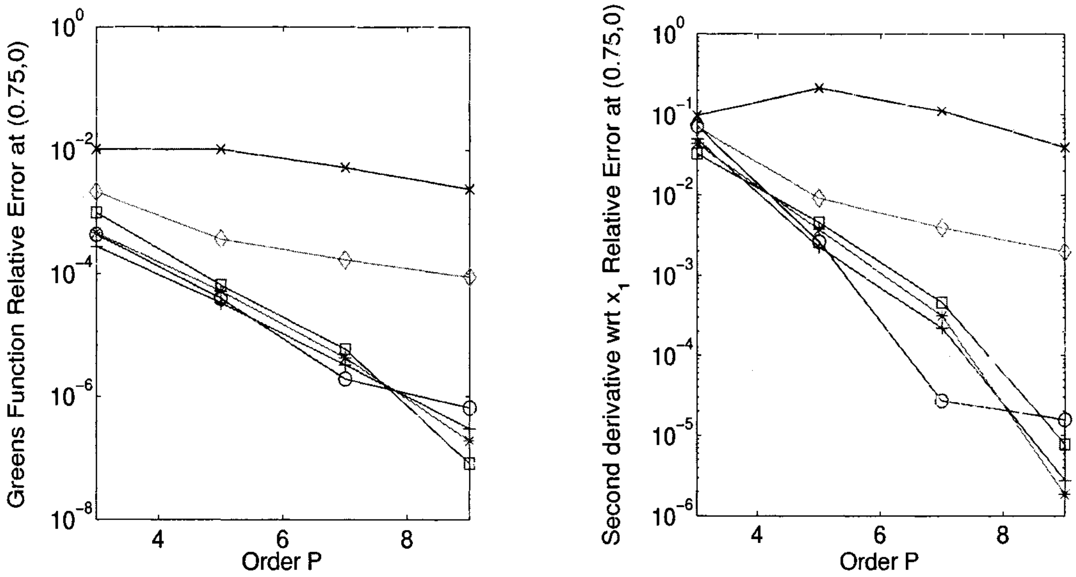

Fig. 12: Relative error as a function of the order of basis polynomials for square boundary with $M = 0$. Element refinement with $\nu^{N_g} \approx 0.008$. Cross: $\nu = 0.09$ and $N_g = 2$; Circle: $\nu = 0.2$ and $N_g = 3$; Plus: $\nu = 0.38$ and $N_g = 5$; Star: $\nu = 0.5$ and $N_g = 7$; Square: $\nu = 0.69$ and $N_g = 13$; Diamond: No element refinement.

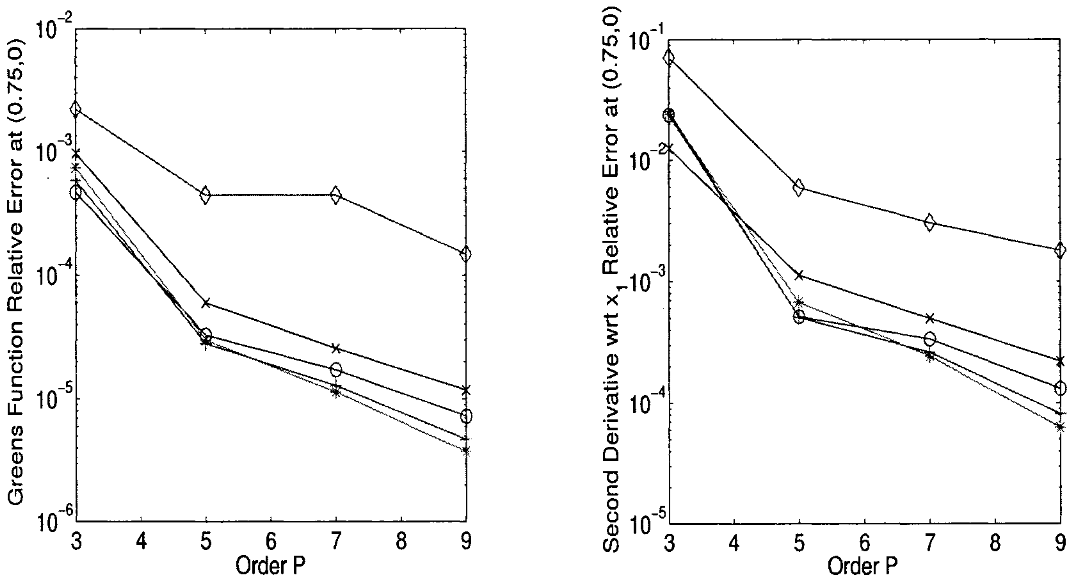

Fig. 13: Relative error as a function of the order of basis polynomials for triangular boundary with $M = 0$. Element refinement with $\nu^{N_g} \approx 0.05$. Cross: $\nu = 0.223$ and $N_g = 2$; Circle: $\nu = 0.37$ and $N_g = 3$; Plus: $\nu = 0.55$ and $N_g = 5$; Star: $\nu = 0.65$ and $N_g = 7$; Diamond: No element refinement.

$(0.5, -0.5)$ and $(-0.5, 0)$. Fig. 13 shows the results obtained for a refined corner element length of $\nu^{N_g} \approx 0.05$ at field point $\mathbf{z} = (0.75, 0)$. Again, for all combinations of ν and N_g, the relative errors for both G_B and $\frac{\partial^2 G_B}{\partial x_1^2}$ are on the same order of magnitude for each P. Therefore, this element refinement strategy can be easily and successfully applied to all boundaries, regardless of corner angles and locations.

IV.4 SINC FUNCTION COLLOCATION METHOD

IV.4.1 Properties of Sinc Functions

The second method studied for the improvement of errors caused by corner singularities involves a change from Chebyshev polynomial basis functions to Sinc basis functions (Appendix B) on all corner elements. In this method, Chebyshev basis functions are still applied to all elements not containing a corner point. The first step in the Sinc collocation method is to map the interval $[0, 1]$ onto $(-\infty, \infty)$ using the transformation

$$\zeta(t) = \ln(\tfrac{t}{1-t})$$

Next, a grid spacing, h, is chosen to approximate a function, $f(\bar{t})$, using a "Whittaker cardinal" approximation, given by

$$f(\bar{t}) \approx \sum_{k=-\infty}^{\infty} f(kh)Sinc(\frac{\bar{t}-kh}{h}) \tag{58}$$

where the Sinc function in the above equation is defined on $-\infty < \bar{t} < \infty$, by

$$Sinc(\bar{t}) = \begin{cases} \frac{\sin(\pi\bar{t})}{\pi\bar{t}} & \text{for } \bar{t} \neq 0 \\ 1 & \text{for } \bar{t} = 0 \end{cases} \tag{59}$$

The basis functions on $[0,1]$ are the composite translated Sinc functions (Appendix B), denoted $Sn_m(\bar{t})$ [37, 39]. The corresponding Sinc collocation points are also given in Appendix B.

Using the Sinc basis functions, the exact Green's function on any corner element can be approximated in the form of a series expansion as

$$f(\bar{t}) \approx \sum_{k=-\infty}^{\infty} f(kh)Sinc(\frac{\bar{t}-kh}{h}) \tag{60}$$

It is important to note here that Sinc expansions always vanish at the endpoints of the interval $[0,1]$. Therefore, equation (60) must be modified by adding a spline at each endpoint [32], resulting in the revised equation

$$G_B\left(\bar{\mathbf{x}}_s, \bar{\mathbf{y}}, \omega\right) = u_j^{(0)}(1-\bar{t}) + \sum_{m=1}^{2P-1} u_j^{(m)} Sn_m(\bar{t}) + u_j^{(2P)}\bar{t} \tag{61}$$

IV.4.2 Sinc Function Benefits

Sinc function approximation in the presence of corner singularities is beneficial for several reasons. First, the Sinc function collocation method effectively handles singularities by clustering more collocation points near the singularities [32]. Also, shifting from Chebyshev polynomials to Sinc basis functions on corner elements can be done easily [7]. The linear system of equations given by equation (40) in section III.1.2 will remain unchanged except for the substitution of Sinc basis functions on corner elements. Furthermore, for a step size of $h = \frac{\pi}{\sqrt{P}}$ and a Sinc basis function order of $2P$, where P is the order of the Chebyshev basis functions, approximation by Sinc functions yields errors of $O(e^{-c\sqrt{P}})$, where c is a constant, even in the presence of singularities [39]. Lastly, using a Sinc function expansion to approximate the solution to equation (40) is advantageous because the interval integrands are of the form $F(\bar{t})Sn_m(\bar{t})$ [37]. Due to the property given by

Table IX: Relative errors of exact Green's function and its second derivative with respect to x_1 as the order of Chebyshev basis functions, P, increases. The order of Sinc basis functions is $2P$. The frequency is 4π and the mean flow Mach number is $M = 0$.

Order	Point A	$\overline{\mathbf{z}} = (0.51, 0)$	Point B	$\overline{\mathbf{z}} = (0.75, 0)$
P	G_B	$\frac{\partial^2 G_B}{\partial x_1^2}$	G_B	$\frac{\partial^2 G_B}{\partial x_1^2}$
1	0.0451943	131.388	0.0163564	0.326271
2	0.0381091	119.749	0.0293117	0.908818
3	0.00376997	10.3568	0.00330225	0.0651904
5	0.000565250	0.194821	0.000814077	0.0195681
7	0.000172541	0.00525949	0.000215981	0.00533759
9	0.0000720711	0.00161089	0.0000725946	0.00172283
11	0.0000306075	0.000544329	0.0000272665	0.000604561

$$Sn_m(\bar{t}_k) = 0 \quad \text{for} \quad m \neq k$$

the Sinc quadrature rule evaluates the integrals for this special case by

$$\int_0^1 F(\bar{t}) Sn_m(\bar{t}) d\bar{t} = h \frac{F(\bar{t}_m)}{\zeta'(\bar{t}_m)} + O(e^{-c_2\sqrt{P}}) \tag{62}$$

where c_2 is a constant. Therefore, most of the integrals on corner elements in equation (40) are approximated by the first term on the right-hand-side of equation (62), reducing the computation to a single iteration.

IV.4.3 Results for the 2-D Square Boundary

Consider the 16-element square with a Sinc function expansion on the corner elements and a Chebyshev basis function expansion on all other elements. Table IX shows the relative errors for the Green's function, G_B, and its second derivative, $\frac{\partial^2 G_B}{\partial x_1^2}$, at points (A) $\overline{\mathbf{z}} = (0.51, 0)$ and (B) $\overline{\mathbf{z}} = (0.75, 0)$. The frequency is $\omega = 4\pi$, the source point is at $\overline{\mathbf{y}} = (0, -20)$, and the mean flow Mach number is $M = 0$. In each case, the order of the Sinc basis functions is $2P$ corresponding to order P for the Chebyshev expansion. The numerical solutions are compared with a high order ($P = 15$ for Chebyshev elements) basis function solution. The data for Table IX are plotted in Fig. 14. Table IX and Fig. 14 show that as the order of the Chebyshev and Sinc functions increases, exponential rate of decay is not achieved.

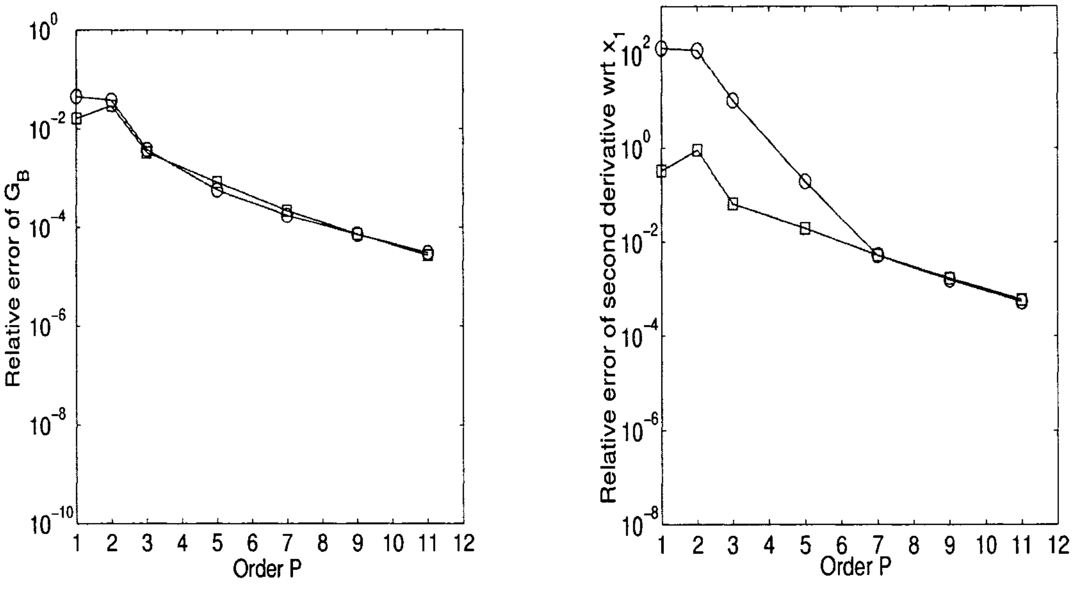

Fig. 14: Relative error as a function of the order of basis polynomials for square boundary with $M = 0$. Sinc basis function order is $2P$. Circles: $\overline{\mathbf{z}} = (0.51, 0)$; Squares: $\overline{\mathbf{z}} = (0.75, 0)$.

IV.4.4 Comparison of Sinc Collocation Method to Chebyshev Collocation Method with and without Element Refinement

In order to compare the results of the Sinc collocation method to the Chebyshev collocation method without element refinement, it is useful to recall the singular solution asymptotic expansion given in Section IV.1.1, which is

$$g_s(r,\theta) \sim \sum_{p=0}^{\infty} a_p g_p(r,\theta) = \sum_{p=0}^{\infty} a_p J_{pv}\left(krf(\theta)\right)\cos\left(\sigma\right)$$

where the approximation for $J_{pv}(z)$ is given by

$$J_{pv}(z) \sim \frac{1}{\Gamma\left(pv+1\right)}\left(\frac{z}{2}\right)^{pv} = C_p z^{pv}$$

As an example, consider the case where $v = 0.75$. Fig. 15 shows the errors resulting when the test function $f(z) = z^{0.75}$ is approximated using both Chebyshev and Sinc basis functions as the order of basis functions is increased. The error is calculated by taking the L_2-norm of the difference between the expansion solution and the exact solution. In this figure, the "order" corresponds to the number, P, of Chebyshev basis functions used in the approximation. The number of Sinc basis functions is twice the number of Chebyshev basis functions. According to Fig. 15, the Sinc approximation

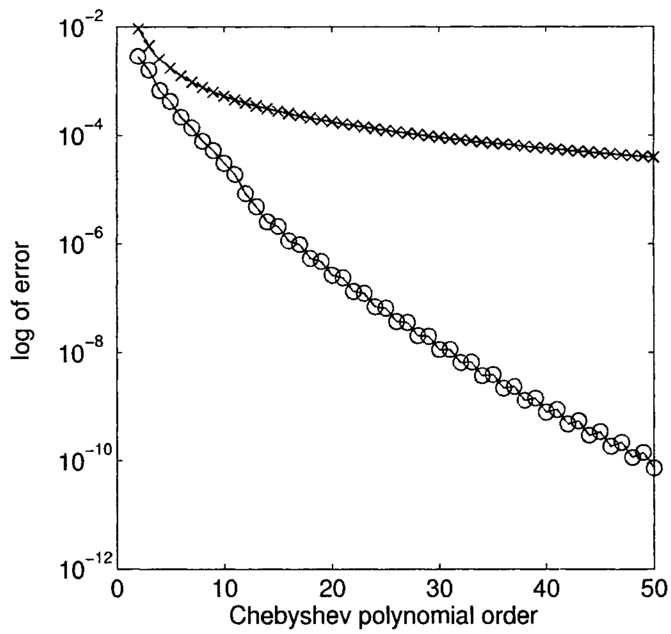

Fig. 15: Error as a function of Chebyshev polynomial order for test function $f(z) = z^{0.75}$. Cross: Chebyshev basis function approximation; Circles: Sinc basis function approximation.

yields better results than the Chebyshev approximation for all basis function orders. However, the singular solution expansion also contains terms with higher exponents, such as $2v = 1.50$ and $3v = 2.25$. Figs. 16 and 17 are similar to Fig. 15, except that they contain results for the test functions $f(z) = z^{1.50}$ and $f(z) = z^{2.25}$ respectively. It is clear from all three figures that the Chebyshev basis function approximation improves as the exponent increases, while the Sinc basis function approximation worsens. Since the singular solution at a corner is a summation of functions with varying exponents, the Sinc function approximation of this solution does not give much better results than the Chebyshev polynomial approximation.

When compared with the element refinement approach, the Sinc collocation method fails to achieve exponential convergence as the order of basis functions is increased. As a result, the element refinement method using Chebyshev polynomials gives a more accurate solution with fewer unknowns. In the element refinement method, the refinement ratio can be optimized so that the level of refinement can be reduced while still retaining exponential convergence under acceptable relative errors. Therefore, the exponential grading element refinement technique using Chebyshev polynomials is preferred over the Sinc function collocation method.

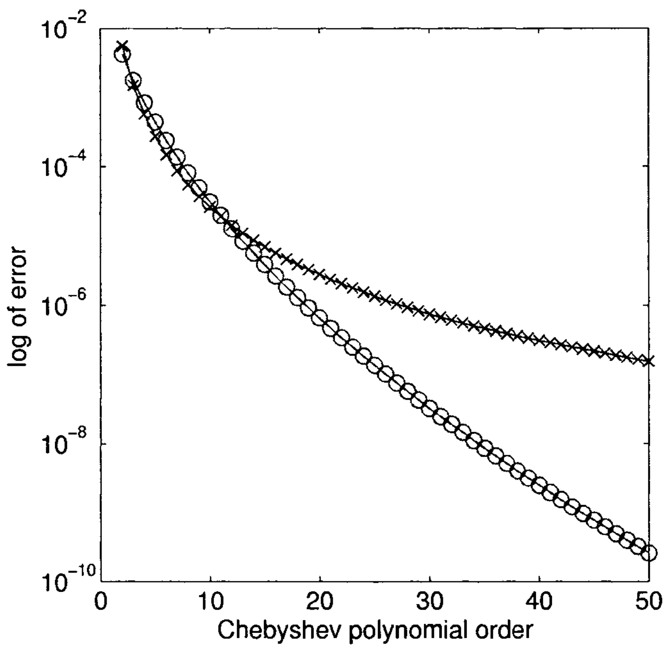

Fig. 16: Error as a function of Chebyshev polynomial order for test function $f(z) = z^{1.50}$. Cross: Chebyshev basis function approximation; Circles: Sinc basis function approximation.

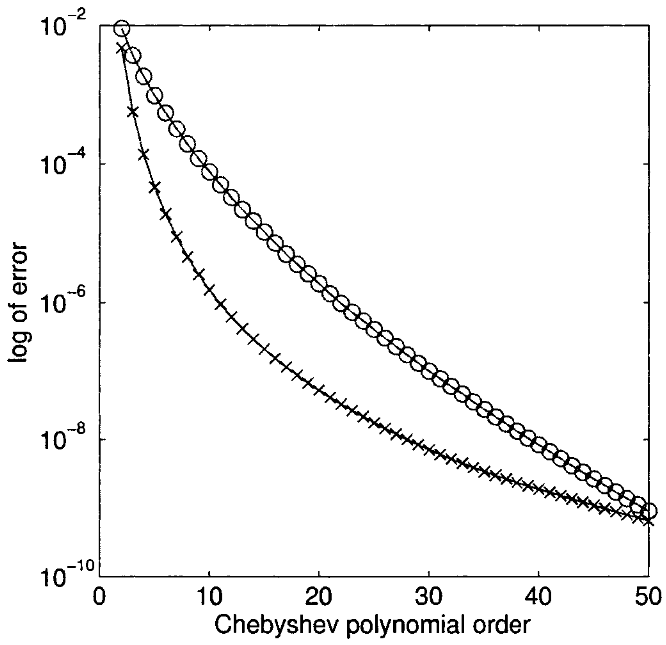

Fig. 17: Error as a function of Chebyshev polynomial order for test function $f(z) = z^{2.25}$. Cross: Chebyshev basis function approximation; Circles: Sinc basis function approximation.

CHAPTER V

TIME-DOMAIN BOUNDARY ELEMENT METHOD FOR 3D SURFACES

To this point, a spectral collocation boundary element method for solving the convective wave equation in the frequency domain has been developed and applied to arbitrary two-dimensional geometries. This chapter focuses on a time-domain boundary element method used to compute exact Green's functions for general three-dimensional surfaces. The time-domain BEM has several advantages over the frequency-domain BEM. First, the inversion of a large, dense matrix is not required. The system of equations in the time-domain BEM results in sparse matrices at all time steps. Next, only a single computation is needed to solve for the exact Green's functions at all frequencies. Finally, the computational complexity can be reduced to $O(N_t N \log^2 N)$ where N_t is the total number of time steps and N is the total number of spatial basis functions [16, 17]. This property makes the time-domain BEM potentially feasible for routine application at mid to high frequencies.

V.1 FORMULATION OF THE TIME-DOMAIN BEM

V.1.1 The March-On-Time Method

Consider again the time-domain convective wave equation

$$(\frac{\partial}{\partial t} + \mathbf{U} \cdot \nabla)^2 g(\mathbf{x}, \mathbf{y}, t, s) - \nabla^2 g(\mathbf{x}, \mathbf{y}, t, s) = \delta(t-s)\delta(\mathbf{x}-\mathbf{y}) \tag{63}$$

with boundary condition

$$\frac{\partial g}{\partial n} = 0 \tag{64}$$

on all solid surfaces. By using a free-space Green's function, equation (63) with boundary condition (64) can be cast into a boundary integral equation as

$$\begin{aligned} 4\pi C_s g(\mathbf{z}_s, \mathbf{y}, t, s) = \frac{q(t-s-|\mathbf{y}-\mathbf{z}_s|)}{|\mathbf{y}-\mathbf{z}_s|} &+ \int_S \left[\frac{1}{R^2}\left[\frac{\partial R}{\partial n} - U_n\left(\mathbf{U}\cdot\nabla R\right)\right] g(\mathbf{x}_s, \mathbf{y}, t_R, s)\right. \\ &+ \frac{1}{R}\left[\frac{\partial R}{\partial n} - 2U_n - U_n\left(\mathbf{U}\cdot\nabla R\right)\right]\frac{\partial g}{\partial t}(\mathbf{x}_s, \mathbf{y}, t_R, s) \\ &\left. - \frac{U_n}{R}\left[\mathbf{U}\cdot\nabla g\left(\mathbf{x}_s, \mathbf{y}, t_R, s\right)\right]\right] d\mathbf{x}_s \end{aligned} \tag{65}$$

where $R = |\mathbf{x}_s - \mathbf{z}_s|$ and $t_R = t - R$. In equation (65), $\mathbf{z}_s$ is a point on the body surface, S, and $C_s = 0.5$ for boundary points on smooth surfaces. For computational purposes, the time delta function, $\delta(t-s)$, has been replaced by a finite continuous function, $q(t-s)$, which has a spectrum of unity over the frequency range of interest (Appendix C). The boundary integral equation (65) represents a reduction in spatial dimensions from 3D to 2D and hence, only a surface mesh is required for discretization instead of a volume mesh. Once the exact Green's function, $g(\mathbf{x}, \mathbf{y}, t, s)$, is found, the frequency-domain solution, $\tilde{g}(\mathbf{x}, \mathbf{y}, \omega, s)$, for use in acoustic analogy can be obtained by a Fourier transform in time, for any frequency ω. To solve equation (65), the exact Green's function is represented in terms of N spatial basis functions and N_t temporal basis functions as

$$g\left(\mathbf{x}_s, \mathbf{y}, t, s\right) = \sum_{n=0}^{N_t} \sum_{i=1}^{N} u_i^n \phi_i\left(\mathbf{x}_s\right) \psi_n(t) \tag{66}$$

where u_i^n are the expansion coefficients. Both the spatial and temporal basis functions will be discussed in subsequent sections of this chapter.

A linear system of equations is formed by substituting (66) into equation (65) and then solved for the expansion coefficients, u_i^n, by a March-On-Time (MOT) method. Consider equation (65) in the absence of mean flow,

$$4\pi C_s g(\mathbf{z}_s, \mathbf{y}, t, s) = \frac{q(t-s-r)}{r} + \int_S \frac{1}{R^2} \frac{\partial R}{\partial n} [g]_{t_R} d\mathbf{x}_s + \int_S \frac{1}{R} \frac{\partial R}{\partial n} \left[\frac{\partial g}{\partial t}\right]_{t_R} d\mathbf{x}_s \tag{67}$$

where $R = |\mathbf{x}_s - \mathbf{z}_s|$ and $r = |\mathbf{y} - \mathbf{z}_s|$. By substituting (66) into (67) and forcing the equation to be satisfied at collocation points $\mathbf{x}_k$ and time level t_j, the linear system of equations becomes

$$\begin{aligned} 4\pi C_s \sum_{n=0}^{N_t} \sum_{i=1}^{N} u_i^n \phi_i\left(\mathbf{x}_k\right) \psi_n(t_j) = \frac{1}{r} q(t_j - s - r) + \int_S \frac{1}{R^2} \frac{\partial R}{\partial n} \sum_{n=0}^{N_t} \sum_{i=1}^{N} u_i^n \phi_i\left(\mathbf{x}_s\right) \psi_n(t_j - R) d\mathbf{x}_s \\ + \int_S \frac{1}{R} \frac{\partial R}{\partial n} \sum_{n=0}^{N_t} \sum_{i=1}^{N} u_i^n \phi_i\left(\mathbf{x}_s\right) \psi_n'(t_j - R) d\mathbf{x}_s \end{aligned} \tag{68}$$

for $k = 1, 2, ..., N$ and $j = 1, 2, ..., N_t$. In equation (68), $R = |\mathbf{x}_s - \mathbf{x}_k|$ and

$$\frac{\partial R}{\partial n} = \frac{\mathbf{n} \cdot (\mathbf{x}_s - \mathbf{x}_k)}{|\mathbf{x}_s - \mathbf{x}_k|}$$

By the property of causality,

$$\psi_n(t_j) \equiv 0 \quad \text{for } j > n$$

equation (68) can be written as a time marching scheme, given by

$$\mathbf{B}_0\mathbf{u}^j = \mathbf{q}^j - \sum_{m=1}^{j} \mathbf{B}_m\mathbf{u}^{j-m} \tag{69}$$

where $\mathbf{u}^j$ is a vector containing all unknown expansion coefficients at time level t_j,

$$\mathbf{u}^j = \begin{bmatrix} u_1^j \\ u_2^j \\ \cdot \\ \cdot \\ u_N^j \end{bmatrix}$$

Equation (69) relates the solution at the current time level $t = t_j$ to the solutions at all previous time levels. Specifically, at time level t_j, the rows and columns of matrix $\mathbf{B}_m$ are

$$\{\mathbf{B}_m\}_{ki} = -\int_S \frac{1}{R^2}\frac{\partial R}{\partial n}\phi_i(\mathbf{x}_s)\,\psi_{j-m}(t_j - R)\,d\mathbf{x}_s - \int_S \frac{1}{R}\frac{\partial R}{\partial n}\phi_i(\mathbf{x}_s)\,\psi'_{j-m}(t_j - R)\,d\mathbf{x}_s$$
$$+4\pi C_s\phi_i(\mathbf{x}_k)\,\psi_{j-m}(t_j) \tag{70}$$

and $\mathbf{B}_0$ is formed from $\mathbf{B}_m$ when $m = 0$. At each time level, t_j, the matrix $\mathbf{B}_0$ is a sparse matrix, which can be solved using iterative methods in order to improve computational efficiency.

V.1.2 Discussion of Temporal Basis Functions

The temporal basis functions chosen for the time-domain spectral collocation boundary element method are cubic interpolation functions defined as

$$\psi_j(t) = \Psi(t - t_j)$$

where $t_j = j\Delta t$ and the definition of $\Psi(t)$ is given in Appendix B. Then, the expression for the $\mathbf{B}$ matrices can be written as

$$\{\mathbf{B}_m\}_{ki} = -\int_S \frac{1}{R^2}\frac{\partial R}{\partial n}\phi_i(\mathbf{x}_s)\,\Psi(t_j - R - t_{j-m})\,d\mathbf{x}_s$$
$$-\int_S \frac{1}{R}\frac{\partial R}{\partial n}\phi_i(\mathbf{x}_s)\,\Psi'(t_j - R - t_{j-m})\,d\mathbf{x}_s$$
$$+4\pi C_s\phi_i(\mathbf{x}_k)\,\Psi(t_j - t_{j-m})$$

or

$$\{\mathbf{B}_m\}_{ki} = -\int_S \frac{1}{R^2}\frac{\partial R}{\partial n}\phi_i(\mathbf{x}_s)\,\Psi(m\Delta t - R)\,d\mathbf{x}_s - \int_S \frac{1}{R}\frac{\partial R}{\partial n}\phi_i(\mathbf{x}_s)\,\Psi'(m\Delta t - R)\,d\mathbf{x}_s + 4\pi C_s\phi_i(\mathbf{x}_k)\,\Psi(m\Delta t) \tag{71}$$

In equation (71), the **B** matrices are independent of time t. As a result, each **B** matrix is computed only once and stored in computer memory for future use. Furthermore, by the definition of the temporal basis functions, $\Psi(m\Delta t - R) = 0$ when

$$m\Delta t - R > 3\Delta t$$

or

$$m > \frac{R + 3\Delta t}{\Delta t}$$

This implies that all entries of a $\mathbf{B}_m$ matrix are zero when

$$m > \frac{R_{\text{max}}}{\Delta t} + 3$$

where R_{max} is the maximum dimension of the three-dimensional body. For the case when $m = 0$, the matrix $\mathbf{B}_0$ is given as

$$\{\mathbf{B}_0\}_{ki} = -\int_S \frac{1}{R^2}\frac{\partial R}{\partial n}\phi_i(\mathbf{x}_s)\,\Psi(-R)\,d\mathbf{x}_s - \int_S \frac{1}{R}\frac{\partial R}{\partial n}\phi_i(\mathbf{x}_s)\,\Psi'(-R)\,d\mathbf{x}_s + 4\pi C_s\phi_i(\mathbf{x}_k)\,\Psi(0) \tag{72}$$

If the time step is chosen such that

$$\Delta t < R_{min}$$

then

$$\Psi(-R) = 0$$

except when $R = 0$, i.e., $k = i$. Consequently, $\mathbf{B}_0$ will be a diagonal matrix when Δt is chosen to be less than the minimum distance between collocation points.

V.1.3 Triangular Boundary Elements

Any open or closed three-dimensional surface can be divided into flat or curved triangles [35]. Triangular boundary elements are therefore more robust when dealing with arbitrary geometries than quadrilateral elements. Let the body surface, S, be discretized into a grid of curved or flat triangular elements, E_α. Each element can be

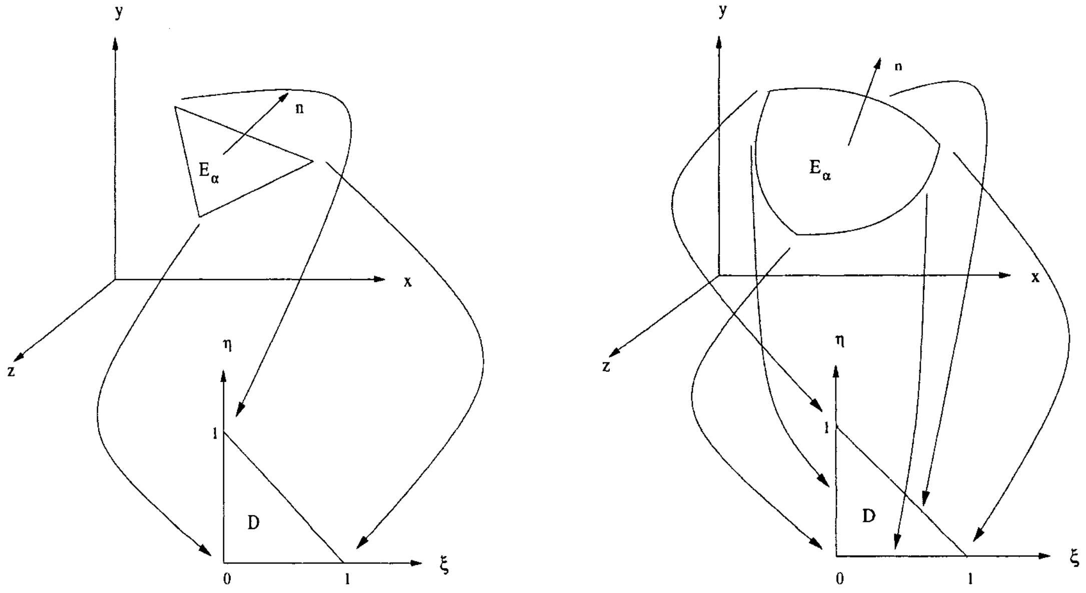

Fig. 18: A three-node (left) and a six-node (right) triangle in three-dimensional space mapped to a right isosceles triangle in the parametric plane.

mapped to a flat right isosceles element, D, in the parametric ξ, η-plane as shown in Fig. 18 [36]. The spectral node distribution over the triangle in the parametric plane is chosen to be the interior points proposed by Strang and Fix [40], with P being the number of collocation points or nodes on each element. Again, interior collocation points are chosen so that the scheme can be applied to any geometry. An inverse mapping from D onto each element E_α determines the location of each node i on the body surface, S.

The spatial basis function for node i, $\phi_i(\mathbf{x}_s)$, satisfies

$$\phi_i(\mathbf{x}_k) = \begin{cases} 1 & k = i \\ 0 & k \neq i \end{cases}$$

for $k = 1, ..., N$ and $i = 1, ..., N$ where N is the total number of spatial basis functions. Hence, $\phi_i(\mathbf{x}_s)$ is non-zero only on one element since i is an interior node. Let the quadrature formula for the surface integrals in the $\mathbf{B}$ matrices be

$$\int_{E_\alpha} F(\mathbf{x}_s) d\mathbf{x}_s = \sum_{\beta=1}^{N_p} w_\beta F(\mathbf{x}_\beta^\alpha)$$

Then, the integrals have the form

$$\int_S \frac{1}{R^2} \frac{\partial R}{\partial n} \phi_i(\mathbf{x}_s) \Psi(m\Delta t - R) d\mathbf{x}_s = \sum_\alpha \int_{E_\alpha} \frac{1}{R^2} \frac{\partial R}{\partial n} \phi_i(\mathbf{x}_s) \Psi(m\Delta t - R) d\mathbf{x}_s$$

$$= \sum_{\alpha} \sum_{\beta} w_\beta \frac{1}{R^2} \frac{\partial R}{\partial n} \phi_i(\mathbf{x}_\beta^\alpha) \Psi(m\Delta t - R) J_\alpha \tag{73}$$

where $R = \left|\mathbf{x}_\beta^\alpha - \mathbf{x}_k\right|$. In equation (73), E_α is the element that supports node i and β is the quadrature point index for the element after it has been mapped to the base right triangle, i.e., domain D. Also, J_α is the Jacobian for element E_α when it is mapped to the base right triangle. The basis function for each node corresponds to a linear combination of a set of independent polynomials in the parametric plane defined as

$$\phi_i(\mathbf{x}_k) = \chi_j(\xi_k, \eta_k) = \sum_{\ell=1}^{P} c_\ell^j T_\ell(\xi_k, \eta_k) \tag{74}$$

for $j = 1, ..., P$. In other words, if the node located at $\mathbf{x}_k$ is mapped to the point (ξ_k, η_k) in domain D, the corresponding basis function for that node depends only on its location in the parametric plane. One suitable basis set for the functions $T_\ell(\xi, \eta)$ is the set comprised of Proriol's orthogonal polynomials (Appendix B) [6, 36].

V.2 TREATMENT OF KERNEL SINGULARITIES

Consider the first integral in equation (71), given by

$$\int_S \frac{1}{R^2} \frac{\partial R}{\partial n} \phi_i(\mathbf{x}_s) \Psi(m\Delta t - R) \, d\mathbf{x}_s$$

and note that

$$\frac{1}{R^2} \frac{\partial R}{\partial n} = \frac{\mathbf{n}_s \cdot (\mathbf{x}_s - \mathbf{x}_k)}{\left|\mathbf{x}_s - \mathbf{x}_k\right|^3}$$

Hence, the integral kernel is singular when integration is being performed on the element containing $\mathbf{x}_k$. Let the element be parameterized as

$$\mathbf{x}(\xi, \eta) = \mathbf{a} + \mathbf{b}\xi + \mathbf{c}\eta + \mathbf{d}\xi^2 + \mathbf{e}\eta^2 + \mathbf{f}\xi\eta$$

so that

$$\mathbf{x}_k(\xi, \eta) = \mathbf{a} + \mathbf{b}\xi_k + \mathbf{c}\eta_k + \mathbf{d}\xi_k^2 + \mathbf{e}\eta_k^2 + \mathbf{f}\xi_k\eta_k$$

$$\mathbf{x}_s(\xi, \eta) = \mathbf{a} + \mathbf{b}\xi_s + \mathbf{c}\eta_s + \mathbf{d}\xi_s^2 + \mathbf{e}\eta_s^2 + \mathbf{f}\xi_s\eta_s$$

Then,

$$\int_S \frac{1}{R^2} \frac{\partial R}{\partial n} \phi_i(\mathbf{x}_s) \Psi(m\Delta t - R) d\mathbf{x}_s = \int \int \frac{\mathbf{n}_s \cdot (\mathbf{x}_s - \mathbf{x}_k)}{\left|\mathbf{x}_s - \mathbf{x}_k\right|^3} \phi_i(\mathbf{x}_s) \Psi(m\Delta t - \left|\mathbf{x}_s - \mathbf{x}_k\right|)$$

$$\cdot \left|\mathbf{x}_\xi \times \mathbf{x}_\eta\right| d\xi d\eta$$

where

$$\mathbf{x}_s - \mathbf{x}_k = \mathbf{b}\left(\xi_s - \xi_k\right) + \mathbf{c}\left(\eta_s - \eta_k\right) + \mathbf{d}\left(\xi_s^2 - \xi_k^2\right) + \mathbf{e}\left(\eta_s^2 - \eta_k^2\right) + \mathbf{f}\left(\xi_s\eta_s - \xi_k\eta_k\right)$$

Let

$$\xi_s - \xi_k = r\cos\theta, \quad \eta_s - \eta_k = r\sin\theta$$

so that

$$\begin{aligned}
\mathbf{x}_s - \mathbf{x}_k &= \mathbf{b}r\cos\theta + \mathbf{c}r\sin\theta + \mathbf{d}\left((r\cos\theta + \xi_k)^2 - \xi_k^2\right) + \mathbf{e}\left((r\sin\theta + \eta_k)^2 - \eta_k^2\right) \\
&\quad + \mathbf{f}\left((r\cos\theta + \xi_k)(r\sin\theta + \eta_k) - \xi_k\eta_k\right) \\
&= r\left(\mathbf{b}\cos\theta + \mathbf{c}\sin\theta\right) + \mathbf{d}\left(r^2\cos^2\theta + 2\xi_k r\cos\theta\right) + \mathbf{e}\left(r^2\sin^2\theta + 2\eta_k r\sin\theta\right) \\
&\quad + \mathbf{f}\left(r^2\cos\theta\sin\theta + \xi_k r\sin\theta + \eta_k r\cos\theta\right) \\
&= O(r)
\end{aligned}$$

With the above change of variables, $\mathbf{n}_s$ becomes

$$\mathbf{n}_s = \frac{\mathbf{x}_\xi \times \mathbf{x}_\eta}{\left|\mathbf{x}_\xi \times \mathbf{x}_\eta\right|} = \frac{\left(\mathbf{b} + 2\mathbf{d}\xi_s + \mathbf{f}\eta_s\right) \times \left(\mathbf{c} + \mathbf{f}\xi_s + 2\mathbf{e}\eta_s\right)}{\left|\left(\mathbf{b} + 2\mathbf{d}\xi_s + \mathbf{f}\eta_s\right) \times \left(\mathbf{c} + \mathbf{f}\xi_s + 2\mathbf{e}\eta_s\right)\right|} \tag{75}$$

For points $\mathbf{x}_s$ on the same element as $\mathbf{x}_k$, the numerator of equation (75) can be written as

$$\begin{aligned}
\left(\mathbf{b} + 2\mathbf{d}\xi_s + \mathbf{f}\eta_s\right) \times \left(\mathbf{c} + \mathbf{f}\xi_s + 2\mathbf{e}\eta_s\right) &= \left(\mathbf{b} + 2\mathbf{d}\xi_k + 2\mathbf{d}r\cos\theta + \mathbf{f}\eta_k + \mathbf{f}r\sin\theta\right) \\
&\quad \times \left(\mathbf{c} + \mathbf{f}\xi_k + \mathbf{c} + \mathbf{f}r\cos\theta + 2\mathbf{e}\eta_k + 2\mathbf{e}r\sin\theta\right)
\end{aligned}$$

Therefore, by the change in variables,

$$\left(\mathbf{x}_\xi \times \mathbf{x}_\eta\right) \cdot \left(\mathbf{x}_s - \mathbf{x}_k\right) = O(r^2)$$

$$\frac{1}{R^2}\frac{\partial R}{\partial n} = \frac{\mathbf{n}_s \cdot \left(\mathbf{x}_s - \mathbf{x}_k\right)}{\left|\mathbf{x}_s - \mathbf{x}_k\right|^3} = O\left(\frac{1}{r}\right)$$

Thus, the integrand is integrable when the first integral in equation (71) is written in polar coordinates centered at (ξ_k, η_k) as

$$\int_{\theta_1}^{\theta_2}\int_0^{r(\theta)} \frac{1}{R^2}\frac{\partial R}{\partial n}\phi_i(\mathbf{x}_s)\psi_{j-m}(t_j - R)\left|\mathbf{x}_\xi \times \mathbf{x}_\eta\right| r\,dr\,d\theta$$

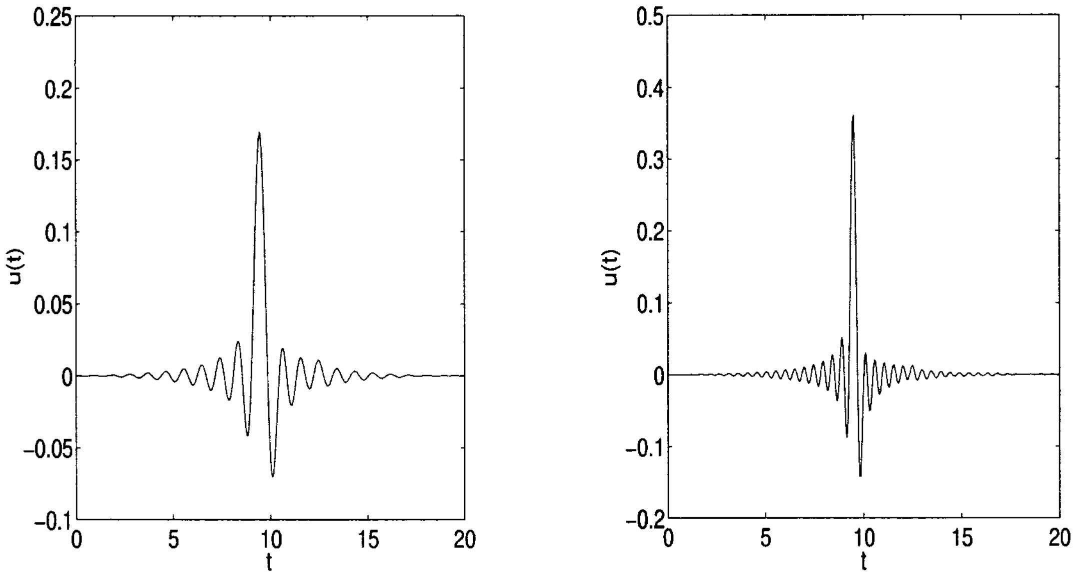

Fig. 19: Transient numerical solution $u(t)$ at $\mathbf{z}_s = (0.0514, 0.00814, 0.497)$. The source function frequency is $\omega_0 = 2\pi$ (left) and $\omega_0 = 4\pi$ (right).

V.3 RESULTS OF TIME-DOMAIN BEM

Consider a sphere of radius 0.5 with a boundary consisting of $N = 760$ curved triangular elements. Fig. 19 shows the expansion coefficient, u_1^j, corresponding to the node located at $\mathbf{z}_s = (0.0514, 0.00814, 0.497)$ versus time obtained by the time-domain boundary element method at two source function frequencies ω_0. The source point is located at $\mathbf{y} = (0, 0, 10)$ and the mean flow Mach number is $M = 0$. The basis function order is $P = 0$, therefore, there is only one interior collocation point associated with each element. The time step size is $\Delta t = 0.05$. A Fourier transform of the data plotted in Fig. 19 gives the solution at all frequencies ω. With 20 grid points in the longitudinal direction, comparison with the exact solution is shown in Fig. 20 for $\omega = 2\pi$ and $\omega = 4\pi$. Clearly, the time domain BEM calculations are in good agreement with the exact solution results.

Unfortunately, one well-known drawback of the MOT scheme formulated in Section V.1 is its tendency toward long-time instability [16, 10]. For example, consider again the sphere of radius 0.5. Fig. 21 illustrates the instability caused by the MOT scheme when $\omega_0 = 6\pi$. Long-time instabilities will eventually occur for all source function frequencies at varying times. Fig. 22 shows the instability beginning at

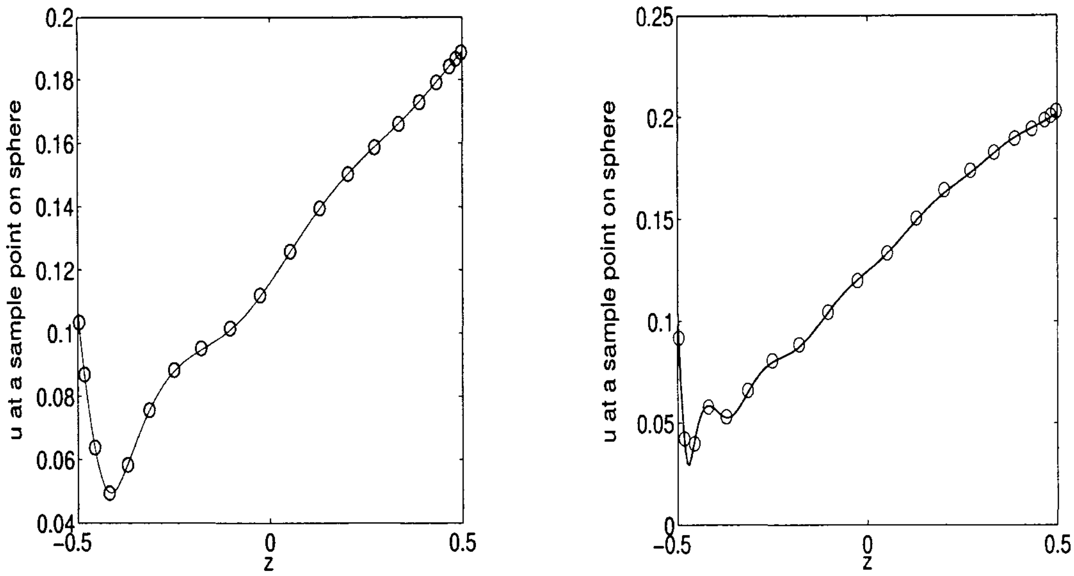

Fig. 20: Comparison with exact solution at $\omega = 2\pi$ (left) and $\omega = 4\pi$ (right). Circles: Time-domain BEM solution; Solid Line: Exact solution.

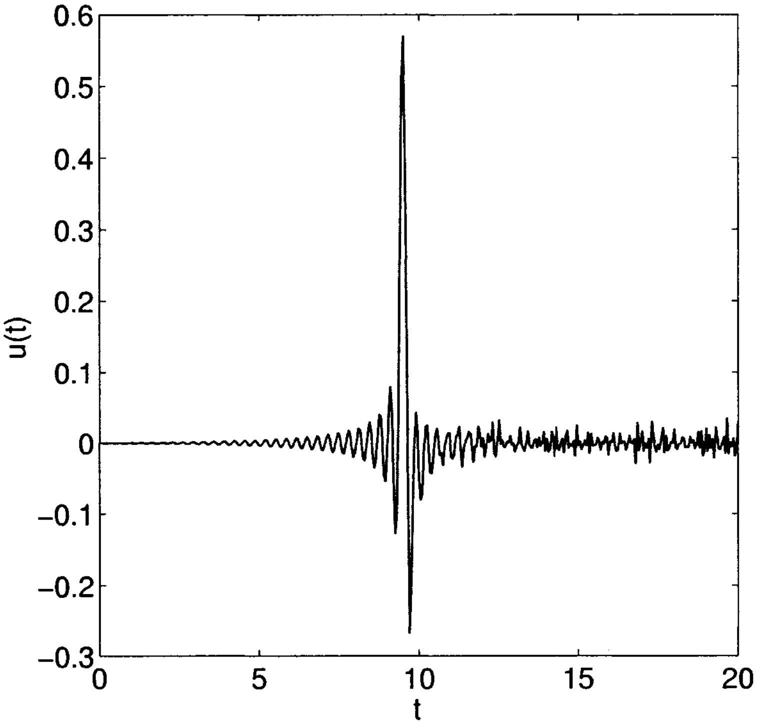

Fig. 21: Transient numerical solution $u(t)$ at $\mathbf{z}_s = (0.0514, 0.00814, 0.497)$. The source function frequency is $\omega_0 = 6\pi$.

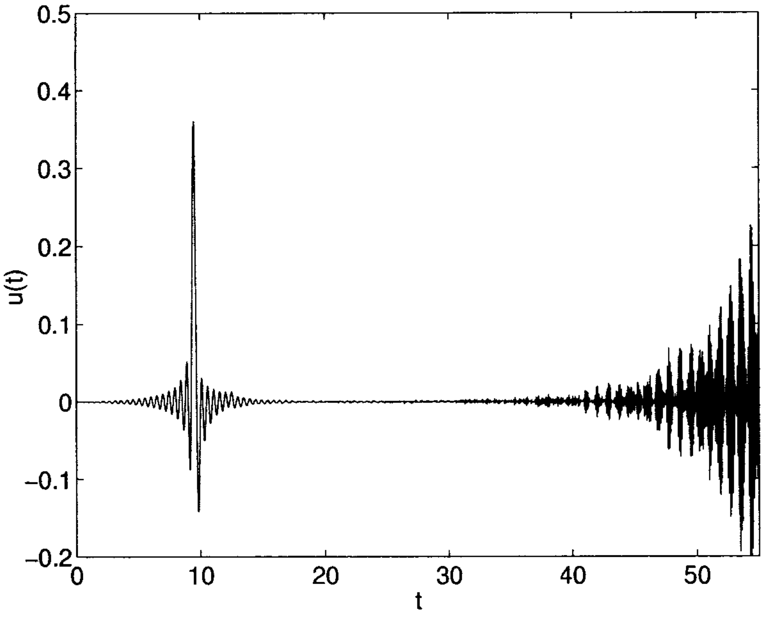

Fig. 22: Transient numerical solution $u(t)$ at $\mathbf{z}_s = (0.0514, 0.00814, 0.497)$. The source function frequency is $\omega_0 = 4\pi$.

approximately $t = 30$ when $\omega_0 = 4\pi$. It is common knowledge that the frequency-domain solutions to Helmholtz integral equations are not unique at certain resonance frequencies. The corresponding time-domain solutions are unique by the presence of initial conditions, but due to discretization inaccuracies, resonant modes of the scatter become excited causing these solutions to contain oscillations as time marches on [16]. The loss in accuracy is more severe for higher frequencies [10]. Several methods are available to overcome long-time instabilities in time-marching numerical solutions. Some examples are time-averaging, modified time stepping, implicit MOT schemes and Galerkin approaches. The method utilized in this thesis is based on Burton and Miller's formulation [9].

V.4 A BURTON-MILLER FORMULATION

One of the most successful and robust approaches for overcoming the non-uniqueness problem of the frequency-domain boundary element method was introduced by Burton and Miller in 1971 [9]. Their method produces a Combined Field Integral Equation (CFIE) made up of the Helmholtz integral equation and its normal derivative equation. The linear combination of the two equations ensures a unique solution at all frequencies [9, 44]. In this section, an extension of the Burton-Miller formulation is derived for the exact Green's function solution in the time-domain.

V.4.1 March-On-Time Formulation

Consider the boundary integral equation derived in Section VI.1.1, given by

$$4\pi C_s g(\mathbf{z}_s, \mathbf{y}, t, s) = \frac{q(t-s-r)}{r} + \int_S \frac{1}{R^2}\frac{\partial R}{\partial n}[g]_{t_R}\, d\mathbf{x}_s + \int_S \frac{1}{R}\frac{\partial R}{\partial n}\left[\frac{\partial g}{\partial t}\right]_{t_R} d\mathbf{x}_s$$

Since

$$\frac{1}{R^2}\frac{\partial R}{\partial n}[g]_{t_R} + \frac{1}{R}\frac{\partial R}{\partial n}\left[\frac{\partial g}{\partial t}\right]_{t_R} = -\frac{\partial}{\partial n}\left[\frac{1}{R}[g]_{t_R}\right]$$

the integral equation can be re-written as

$$4\pi C_s g(\mathbf{z}_s, \mathbf{y}, t, s) = \frac{1}{r} q(t-s-r) - \int_S \frac{\partial}{\partial n}\left[\frac{1}{R}[g]_{t_R}\right] d\mathbf{x}_s \qquad (76)$$

Noting that

$$R\frac{\partial(\frac{1}{R})}{\partial n} = -\frac{1}{R}\frac{\partial R}{\partial n}$$

equation (76) becomes

$$4\pi C_s g(\mathbf{z}_s, \mathbf{y}, t, s) = \frac{1}{r} q(t-s-r) - \int_S \frac{\partial}{\partial n}\left[\frac{1}{R}[g]_{t_R}\right] d\mathbf{x}_s \qquad (77)$$

A time derivative of equation (77) produces

$$4\pi C_s \frac{\partial g}{\partial t}(\mathbf{z}_s, \mathbf{y}, t, s) = \frac{1}{r}\frac{\partial q}{\partial t}(t-s-r) - \int_S \frac{\partial}{\partial n}\left[\frac{1}{R}\left[\frac{\partial g}{\partial t}\right]_{t_R}\right] d\mathbf{x}_s \qquad (78)$$

where $R = |\mathbf{x}_s - \mathbf{z}_s|$ and $r = |\mathbf{y} - \mathbf{z}_s|$. The Burton-Miller time-domain CFIE is a linear combination of equation (78) and the normal gradient at the boundary of equation (77), given by [29]

$$4\pi\frac{\partial}{\partial n_z}[C_s g(\mathbf{z}_s, \mathbf{y}, t, s)] = \frac{\partial}{\partial n_z}\left[\frac{1}{r} q(t-s-r)\right] - \frac{\partial}{\partial n_z}\int_S \frac{\partial}{\partial n}\left[\frac{1}{R}[g]_{t_R}\right] d\mathbf{x}_s \qquad (79)$$

In equation (79), $\frac{\partial}{\partial n_z}$ is the normal derivative with respect to $\mathbf{z}$ at boundary point $\mathbf{z}_s$. By the boundary condition involving the exact Green's function,

$$\frac{\partial}{\partial n_z} g(\mathbf{z}_s, \mathbf{y}, t, s) = 0$$

equation (79) reduces to

$$4\pi\frac{\partial C_s}{\partial n_z} g(\mathbf{z}_s, \mathbf{y}, t, s) = \frac{\partial}{\partial n_z}\left[\frac{1}{r} q(t-s-r)\right] - \frac{\partial}{\partial n_z}\int_S \frac{\partial}{\partial n}\left[\frac{1}{R}[g]_{t_R}\right] d\mathbf{x}_s \qquad (80)$$

A linear combination of equations (78) and (80) results in

$$(1-a)\,4\pi C_s\frac{\partial g}{\partial t}\left(\mathbf{z}_s,\mathbf{y},t,s\right)+ac4\pi\frac{\partial C_s}{\partial n_z}g(\mathbf{z}_s,\mathbf{y},t,s)=(1-a)\,\frac{1}{r}\frac{\partial q}{\partial t}\left(t-s-r\right)$$
$$+ac\frac{\partial}{\partial n_z}\left[\frac{1}{r}q\left(t-s-r\right)\right]-(1-a)\int_S\frac{\partial}{\partial n}\left[\frac{1}{R}\left[\frac{\partial g}{\partial t}\right]_{t_R}\right]d\mathbf{x}_s$$
$$-ac\frac{\partial}{\partial n_z}\int_S\frac{\partial}{\partial n}\left[\frac{1}{R}\left[g\right]_{t_R}\right]d\mathbf{x}_s \tag{81}$$

where $a\in(0,1)$ is a coupling parameter and c is chosen so that all terms in the equation have comparable orders of magnitude [10]. The Burton-Miller formulation yields unique solutions for all frequencies if ac is appropriately selected [44].

V.4.2 Treatment of Hypersingular Integrals

The main difficulty in using any Burton-Miller formulation is dealing with hypersingular integrals that arise when taking the normal derivative of the original boundary integral equation. With arguments written explicitly, equation (81) is

$$(1-a)\,4\pi C_s\frac{\partial g}{\partial t}\left(\mathbf{z}_s,\mathbf{y},t,s\right)+ac4\pi\frac{\partial C_s}{\partial n_z}g(\mathbf{z}_s,\mathbf{y},t,s)=(1-a)\,\frac{1}{r}\frac{\partial q}{\partial t}\left(t-s-r\right)$$
$$+ac\frac{\partial}{\partial n_z}\left[\frac{1}{r}q\left(t-s-r\right)\right]-(1-a)\int_S\frac{\partial}{\partial n}\left[\frac{1}{R}\left[\frac{\partial g}{\partial t}\left(\mathbf{x}_s,\mathbf{y},t-R,s\right)\right]\right]d\mathbf{x}_s$$
$$-ac\frac{\partial}{\partial n_z}\int_S\frac{\partial}{\partial n}\left[\frac{1}{R}\left[g\left(\mathbf{x}_s,\mathbf{y},t-R,s\right)\right]\right]d\mathbf{x}_s \tag{82}$$

In equation (82), the last term will involve a hypersingular integral because

$$\frac{\partial^2}{\partial n_z\partial n}\left[\frac{1}{R}\right]=O\left(\frac{1}{R^3}\right)$$

To reduce the singularity, the hypersingular integrals are regularized by an approach used by Liu et. al. [29] and Hwang [23] for the frequency-domain Burton-Miller formulation. Consider the relation for determining C_s [29]

$$4\pi C_s=4\pi-\int_S\frac{\partial(\frac{1}{R})}{\partial n}d\mathbf{x}_s \tag{83}$$

Multiplying both sides of equation (83) by $g\left(\mathbf{z},\mathbf{y},t,s\right)$ results in

$$4\pi C_s g\left(\mathbf{z},\mathbf{y},t,s\right)=4\pi g\left(\mathbf{z},\mathbf{y},t,s\right)-\int_S\frac{\partial(\frac{1}{R})}{\partial n}g\left(\mathbf{z},\mathbf{y},t,s\right)d\mathbf{x}_s$$

By taking the normal derivative with respect to $\mathbf{z}$ at the boundary, and using the boundary condition for g, the above becomes

$$4\pi \frac{\partial C_s}{\partial n_z} g\left(\mathbf{z}_s, \mathbf{y}, t, s\right) = -\frac{\partial}{\partial n_z} \int_S \frac{\partial(\frac{1}{R})}{\partial n} g\left(\mathbf{z}_s, \mathbf{y}, t, s\right) d\mathbf{x}_s \tag{84}$$

Equation (84) is substituted into equation (82) to get

$$\begin{aligned}
&(1-a)\, 4\pi C_s \frac{\partial g}{\partial t}\left(\mathbf{z}_s, \mathbf{y}, t, s\right) - ac \frac{\partial}{\partial n_z} \int_S g\left(\mathbf{z}_s, \mathbf{y}, t, s\right) \frac{\partial(\frac{1}{R})}{\partial n} d\mathbf{x}_s = (1-a) \frac{1}{r} \frac{\partial q}{\partial t}(t-s-r) \\
&\quad + ac \frac{\partial}{\partial n_z}\left[\frac{1}{r} q(t-s-r)\right] - (1-a) \int_S \frac{\partial}{\partial n}\left[\frac{1}{R}\left[\frac{\partial g}{\partial t}\left(\mathbf{x}_s, \mathbf{y}, t-R, s\right)\right]\right] d\mathbf{x}_s \\
&\quad - ac \frac{\partial}{\partial n_z} \int_S \frac{\partial}{\partial n}\left[\frac{1}{R}\left[g\left(\mathbf{x}_s, \mathbf{y}, t-R, s\right)\right]\right] d\mathbf{x}_s
\end{aligned}$$

or

$$\begin{aligned}
&(1-a)\, 4\pi C_s \frac{\partial g}{\partial t}\left(\mathbf{z}_s, \mathbf{y}, t, s\right) - ac \frac{\partial}{\partial n_z} \int_S g\left(\mathbf{z}_s, \mathbf{y}, t, s\right) \frac{\partial(\frac{1}{R})}{\partial n} d\mathbf{x}_s = (1-a) \frac{1}{r} \frac{\partial q}{\partial t}(t-s-r) \\
&\quad + ac \frac{\partial}{\partial n_z}\left[\frac{1}{r} q(t-s-r)\right] - (1-a) \int_S \frac{\partial(\frac{1}{R})}{\partial n}\left[g\left(\mathbf{x}_s, \mathbf{y}, t-R, s\right)\right. \\
&\quad \left. + R \frac{\partial g}{\partial t}\left(\mathbf{x}_s, \mathbf{y}, t-R, s\right)\right] d\mathbf{x}_s - ac \frac{\partial}{\partial n_z} \int_S \frac{\partial(\frac{1}{R})}{\partial n}\left[g\left(\mathbf{x}_s, \mathbf{y}, t-R, s\right)\right. \\
&\quad \left. + R \frac{\partial g}{\partial t}\left(\mathbf{x}_s, \mathbf{y}, t-R, s\right)\right] d\mathbf{x}_s
\end{aligned}$$

giving

$$\begin{aligned}
&(1-a)\, 4\pi C_s \frac{\partial g}{\partial t}\left(\mathbf{z}_s, \mathbf{y}, t, s\right) = (1-a) \frac{1}{r} \frac{\partial q}{\partial t}(t-s-r) + ac \frac{\partial}{\partial n_z}\left[\frac{1}{r} q(t-s-r)\right] \\
&\quad - (1-a) \int_S \frac{\partial(\frac{1}{R})}{\partial n}\left[g\left(\mathbf{x}_s, \mathbf{y}, t-R, s\right) + R \frac{\partial g}{\partial t}\left(\mathbf{x}_s, \mathbf{y}, t-R, s\right)\right] d\mathbf{x}_s \\
&\quad - ac \frac{\partial}{\partial n_z} \int_S \frac{\partial(\frac{1}{R})}{\partial n}\left[g\left(\mathbf{x}_s, \mathbf{y}, t-R, s\right) - g\left(\mathbf{z}_s, \mathbf{y}, t-R, s\right)\right. \\
&\quad \left. + R \frac{\partial g}{\partial t}\left(\mathbf{x}_s, \mathbf{y}, t-R, s\right)\right] d\mathbf{x}_s
\end{aligned} \tag{85}$$

The last term in equation (85) is

$$\begin{aligned}
&\frac{\partial}{\partial n_z} \int_S \frac{\partial(\frac{1}{R})}{\partial n}\left[g\left(\mathbf{x}_s, \mathbf{y}, t-R, s\right) - g\left(\mathbf{z}_s, \mathbf{y}, t, s\right) + R \frac{\partial g}{\partial t}\left(\mathbf{x}_s, \mathbf{y}, t-R, s\right)\right] d\mathbf{x}_s \\
&= \int_S \frac{\partial^2(\frac{1}{R})}{\partial n_z \partial n}\left[g\left(\mathbf{x}_s, \mathbf{y}, t-R, s\right) - g\left(\mathbf{z}_s, \mathbf{y}, t, s\right) + R \frac{\partial g}{\partial t}\left(\mathbf{x}_s, \mathbf{y}, t-R, s\right)\right]
\end{aligned}$$

$$
\begin{aligned}
&+\frac{\partial(\frac{1}{R})}{\partial n}\left[\frac{\partial g}{\partial t}(\mathbf{x}_s,\mathbf{y},t-R,s)\left(-\frac{\partial R}{\partial n_z}\right)+\frac{\partial}{\partial n_z}\left[R\frac{\partial g}{\partial t}(\mathbf{x}_s,\mathbf{y},t-R,s)\right]\right]d\mathbf{x}_s \\
&=\int_S \frac{\partial^2(\frac{1}{R})}{\partial n_z \partial n}\left[g(\mathbf{x}_s,\mathbf{y},t-R,s)-g(\mathbf{z}_s,\mathbf{y},t,s)+R\frac{\partial g}{\partial t}(\mathbf{x}_s,\mathbf{y},t-R,s)\right] \\
&\quad +\frac{\partial(\frac{1}{R})}{\partial n}\left[-\frac{\partial R}{\partial n_z}\frac{\partial g}{\partial t}(\mathbf{x}_s,\mathbf{y},t-R,s)+\frac{\partial R}{\partial n_z}\frac{\partial g}{\partial t}(\mathbf{x}_s,\mathbf{y},t-R,s)\right. \\
&\qquad \left. -R\frac{\partial R}{\partial n_z}\frac{\partial^2 g}{\partial t^2}(\mathbf{x}_s,\mathbf{y},t-R,s)\right]d\mathbf{x}_s \\
&=\int_S \frac{\partial^2(\frac{1}{R})}{\partial n_z \partial n}\left[g(\mathbf{x}_s,\mathbf{y},t-R,s)-g(\mathbf{z}_s,\mathbf{y},t,s)+R\frac{\partial g}{\partial t}(\mathbf{x}_s,\mathbf{y},t-R,s)\right] \\
&\qquad -R\frac{\partial(\frac{1}{R})}{\partial n}\frac{\partial R}{\partial n_z}\frac{\partial^2 g}{\partial t^2}(\mathbf{x}_s,\mathbf{y},t-R,s)\,d\mathbf{x}_s
\end{aligned}
\tag{86}
$$

The above hypersingular integral can be reformulated into a weakly singular integral by using a Taylor series expansion, given by

$$
\begin{aligned}
g(\mathbf{x}_s,\mathbf{y},t-R,s) &= g(\mathbf{z}_s+(\mathbf{x}_s-\mathbf{z}_s),\mathbf{y},t-R,s)=g(\mathbf{z}_s+\mathbf{R},\mathbf{y},t-R,s) \\
&= g(\mathbf{z}_s,\mathbf{y},t,s)+\nabla g(\mathbf{z}_s,\mathbf{y},t,s)\cdot\mathbf{R}+\frac{\partial g}{\partial t}(\mathbf{z}_s,\mathbf{y},t,s)(-R)+O\left(R^2\right)
\end{aligned}
$$

where $\mathbf{R}=\mathbf{x}_s-\mathbf{z}_s$. The first integrand in equation (86) becomes

$$
\begin{aligned}
&\frac{\partial^2(\frac{1}{R})}{\partial n_z \partial n}\left[g(\mathbf{x}_s,\mathbf{y},t-R,s)-g(\mathbf{z}_s,\mathbf{y},t,s)+R\frac{\partial g}{\partial t}(\mathbf{x}_s,\mathbf{y},t-R,s)\right] \\
&\qquad\qquad = \frac{\partial^2(\frac{1}{R})}{\partial n_z \partial n}\nabla g(\mathbf{z}_s,\mathbf{y},t,s)\cdot\mathbf{R}
\end{aligned}
$$

which renders the above integrable in a Cauchy principal value sense. Hence, the regularized integral equation is

$$
\begin{aligned}
&(1-a)4\pi C_s\frac{\partial g}{\partial t}(\mathbf{z}_s,\mathbf{y},t,s)=(1-a)\frac{1}{r}\frac{\partial q}{\partial t}(t-s-r)+ac\frac{\partial}{\partial n_z}\left[\frac{1}{r}q(t-s-r)\right] \\
&-(1-a)\int_S\frac{\partial}{\partial n}\left[\frac{1}{R}\left[\frac{\partial g}{\partial t}(\mathbf{x}_s,\mathbf{y},t-R,s)\right]\right]d\mathbf{x}_s-ac\int_S\frac{\partial^2(\frac{1}{R})}{\partial n_z\partial n}\left[g(\mathbf{x}_s,\mathbf{y},t-R,s)\right. \\
&\left.-g(\mathbf{z}_s,\mathbf{y},t,s)+R\frac{\partial g}{\partial t}(\mathbf{x}_s,\mathbf{y},t-R,s)\right]-R\frac{\partial(\frac{1}{R})}{\partial n}\frac{\partial R}{\partial n_z}\frac{\partial^2 g}{\partial t^2}(\mathbf{x}_s,\mathbf{y},t-R,s)\,d\mathbf{x}_s
\end{aligned}
\tag{87}
$$

or

$$
(1-a)4\pi C_s\frac{\partial g}{\partial t}(\mathbf{z}_s,\mathbf{y},t,s)=(1-a)\frac{1}{r}\frac{\partial q}{\partial t}(t-s-r)+ac\frac{\partial}{\partial n_z}\left[\frac{1}{r}q(t-s-r)\right]
$$

$$-(1-a)\int_S \frac{\partial(\frac{1}{R})}{\partial n}\frac{\partial g}{\partial t}(\mathbf{x}_s,\mathbf{y},t-R,s) + R\frac{\partial(\frac{1}{R})}{\partial n}\frac{\partial^2 g}{\partial t^2}(\mathbf{x}_s,\mathbf{y},t-R,s)\,d\mathbf{x}_s$$

$$-ac\int_S \frac{\partial^2(\frac{1}{R})}{\partial n_z\partial n}\left[g(\mathbf{x}_s,\mathbf{y},t-R,s) - g(\mathbf{z}_s,\mathbf{y},t,s) + R\frac{\partial g}{\partial t}(\mathbf{x}_s,\mathbf{y},t-R,s)\right]$$

$$-R\frac{\partial(\frac{1}{R})}{\partial n}\frac{\partial R}{\partial n_z}\frac{\partial^2 g}{\partial t^2}(\mathbf{x}_s,\mathbf{y},t-R,s)\,d\mathbf{x}_s \tag{88}$$

For collocation points $\mathbf{z}_k$ and time step t_j, equation (88) becomes

$$(1-a)\,4\pi C_s\sum_{n=0}^{N_t}\sum_{i=1}^{N}u_i^n\phi_i(\mathbf{z}_k)\psi_n'(t_j) = (1-a)\,\frac{1}{r}\frac{\partial q}{\partial t}(t_j-s-r)$$

$$+ac\frac{\partial}{\partial n_z}\left[\frac{1}{r}q(t_j-s-r)\right] - (1-a)\int_S \frac{\partial(\frac{1}{R})}{\partial n}\sum_{n=0}^{N_t}\sum_{i=1}^{N}u_i^n\phi_i(\mathbf{x}_s)\psi_n'(t_j-R)$$

$$+R\frac{\partial(\frac{1}{R})}{\partial n}\sum_{n=0}^{N_t}\sum_{i=1}^{N}u_i^n\phi_i(\mathbf{x}_s)\psi_n''(t_j-R)d\mathbf{x}_s - ac\int_S \frac{\partial^2(\frac{1}{R})}{\partial n_z\partial n}\left[\sum_{n=0}^{N_t}\sum_{i=1}^{N}u_i^n\phi_i(\mathbf{x}_s)\psi_n(t_j-R)\right.$$

$$\left.-\sum_{n=0}^{N_t}\sum_{i=1}^{N}u_i^n\phi_i(\mathbf{z}_k)\psi_n(t_j) + R\sum_{n=0}^{N_t}\sum_{i=1}^{N}u_i^n\phi_i(\mathbf{x}_s)\psi_n'(t_j-R)\right]d\mathbf{x}_s$$

$$+ac\int_S R\frac{\partial(\frac{1}{R})}{\partial n}\frac{\partial R}{\partial n_z}\sum_{n=0}^{N_t}\sum_{i=1}^{N}u_i^n\phi_i(\mathbf{x}_s)\psi_n''(t_j-R)d\mathbf{x}_s \tag{89}$$

Writing equation (89) as a time marching scheme, i.e.,

$$\mathbf{B}_0\mathbf{u}^j = \mathbf{q}^j - \sum_{m=1}^{j}\mathbf{B}_m\mathbf{u}^{j-m}$$

results in

$$\{\mathbf{B}_m\}_{ki} = (1-a)\,4\pi C_s\phi_i(\mathbf{z}_k)\psi_{j-m}'(t_j) + (1-a)\int_S \frac{\partial(\frac{1}{R})}{\partial n}\phi_i(\mathbf{x}_s)\psi_{j-m}'(t_j-R)d\mathbf{x}_s$$

$$+(1-a)\int_S R\frac{\partial(\frac{1}{R})}{\partial n}\phi_i(\mathbf{x}_s)\psi_{j-m}''(t_j-R)d\mathbf{x}_s + ac\int_S \frac{\partial^2(\frac{1}{R})}{\partial n_z\partial n}\left[\phi_i(\mathbf{x}_s)\psi_{j-m}(t_j-R)\right.$$

$$\left.-\phi_i(\mathbf{z}_k)\psi_{j-m}(t_j) + R\phi_i(\mathbf{x}_s)\psi_{j-m}'(t_j-R)\right]d\mathbf{x}_s$$

$$-ac\int_S R\frac{\partial(\frac{1}{R})}{\partial n}\frac{\partial R}{\partial n_z}\phi_i(\mathbf{x}_s)\psi_{j-m}''(t_j-R)d\mathbf{x}_s \tag{90}$$

Note that since $\phi_i(\mathbf{x}_s)$ is non-zero only when $\mathbf{x}_s \in S_i$, the terms belonging to the matrix $\mathbf{B}_m$ are

$$\{\mathbf{B}_m\}_{ki} = (1-a)\,4\pi C_s\phi_i(\mathbf{z}_k)\,\psi_{j-m}'(t_j) + (1-a)\int_{S_i}\frac{\partial(\frac{1}{R})}{\partial n}\phi_i(\mathbf{x}_s)\,\psi_{j-m}'(t_j-R)\,d\mathbf{x}_s$$

$$
\begin{aligned}
&+(1-a)\int_{S_i} R\frac{\partial(\frac{1}{R})}{\partial n}\phi_i(\mathbf{x}_s)\,\psi''_{j-m}(t_j-R)\,d\mathbf{x}_s \\
&+ac\int_{S_i}\frac{\partial^2(\frac{1}{R})}{\partial n_z\partial n}\left[\phi_i(\mathbf{x}_s)\,\psi_{j-m}(t_j-R)-\phi_i(\mathbf{z}_k)\,\psi_{j-m}(t_j)\right. \\
&\left.+R\phi_i(\mathbf{x}_s)\,\psi'_{j-m}(t_j-R)\right]d\mathbf{x}_s-ac\int_{S_i} R\frac{\partial(\frac{1}{R})}{\partial n}\frac{\partial R}{\partial n_z}\phi_i(\mathbf{x}_s)\,\psi''_{j-m}(t_j-R)\,d\mathbf{x}_s \\
&-ac\int_{S-S_i}\frac{\partial^2(\frac{1}{R})}{\partial n_z\partial n}\phi_i(\mathbf{z}_k)\,\psi_{j-m}(t_j)\,d\mathbf{x}_s
\end{aligned}
\tag{91}
$$

Because of the properties

$$\phi_i(\mathbf{z}_k)=\delta_{ik}$$

and

$$\psi_{j-m}(t_j)=\delta_{m0}$$

the last term in equation (91) is non-zero only for $i=k$ and $m=0$. By denoting

$$D_k=-\int_{S-S_i}\frac{\partial^2(\frac{1}{R})}{\partial n_z\partial n}d\mathbf{x}_s$$

equation (91) can be written as

$$
\begin{aligned}
\{\mathbf{B}_m\}_{ki}&=(1-a)\,4\pi C_s\phi_i(\mathbf{z}_k)\,\psi'_{j-m}(t_j)+acD_k\phi_i(\mathbf{z}_k)\,\psi_{j-m}(t_j) \\
&+(1-a)\int_{S_i}\frac{\partial(\frac{1}{R})}{\partial n}\phi_i(\mathbf{x}_s)\,\psi'_{j-m}(t_j-R)\,d\mathbf{x}_s \\
&+(1-a)\int_{S_i} R\frac{\partial(\frac{1}{R})}{\partial n}\phi_i(\mathbf{x}_s)\,\psi''_{j-m}(t_j-R)\,d\mathbf{x}_s \\
&+ac\int_{S_i}\frac{\partial^2(\frac{1}{R})}{\partial n_z\partial n}\left[\phi_i(\mathbf{x}_s)\,\psi_{j-m}(t_j-R)-\phi_i(\mathbf{z}_k)\,\psi_{j-m}(t_j)\right. \\
&\qquad\left.+R\phi_i(\mathbf{x}_s)\,\psi'_{j-m}(t_j-R)\right]d\mathbf{x}_s \\
&+ac\int_{S_i} R^3\frac{\partial(\frac{1}{R})}{\partial n}\frac{\partial(\frac{1}{R})}{\partial n_z}\phi_i(\mathbf{x}_s)\,\psi''_{j-m}(t_j-R)\,d\mathbf{x}_s
\end{aligned}
\tag{92}
$$

As in the original time-domain formulation, the matrix $\mathbf{B}_0$ is a sparse matrix.

V.5 RESULTS OF TIME-DOMAIN BEM USING BURTON-MILLER FORMULATION

Consider a sphere of radius 0.5 with a boundary consisting of $N = 760$ curved triangular elements. Fig. 23 and Fig. 24 represent the results obtained when the time-domain BEM is revised using the Burton-Miller formulation outlined in Section V.4 for $\omega_0 = 6\pi$ and $\omega_0 = 4\pi$ respectively. For comparison purposes, the expansion coefficient plotted corresponds to the node located at $\mathbf{z}_s = (0.0514, 0.00814, 0.497)$, the basis function order is $P = 0$, the source point is at $\mathbf{y} = (0, 0, 10)$ and the time step size is $\Delta t = 0.05$. All calculations involving the Burton-Miller formulation were performed with $c = -1$. Compared to Fig. 21 and Fig. 22, Fig. 23 and Fig. 24 show the effectiveness of the Burton-Miller formulation in dealing with long-time instabilities that arise in many March-On-Time schemes.

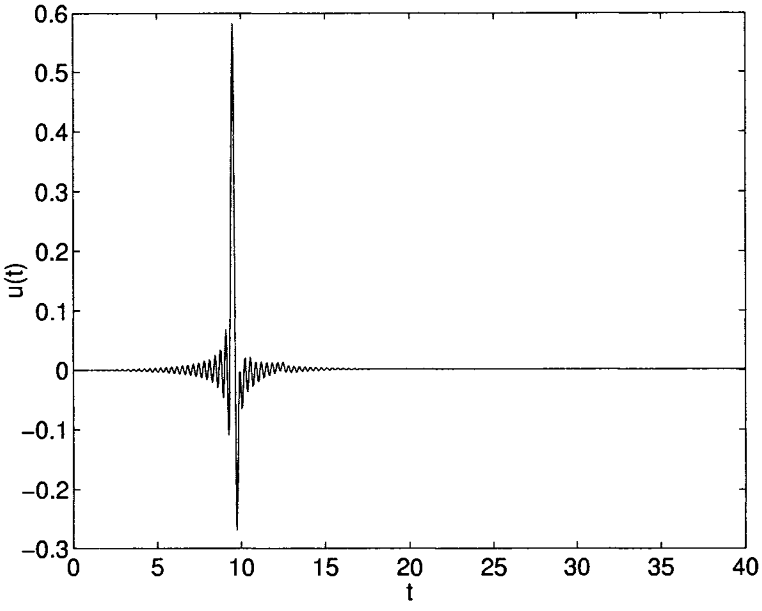

Fig. 23: Transient numerical solution $u(t)$ at $\mathbf{z}_s = (0.0514, 0.00814, 0.497)$ using Burton-Miller Formulation. The source function frequency is $\omega_0 = 6\pi$ and the coupling parameter is $a = 0.5$.

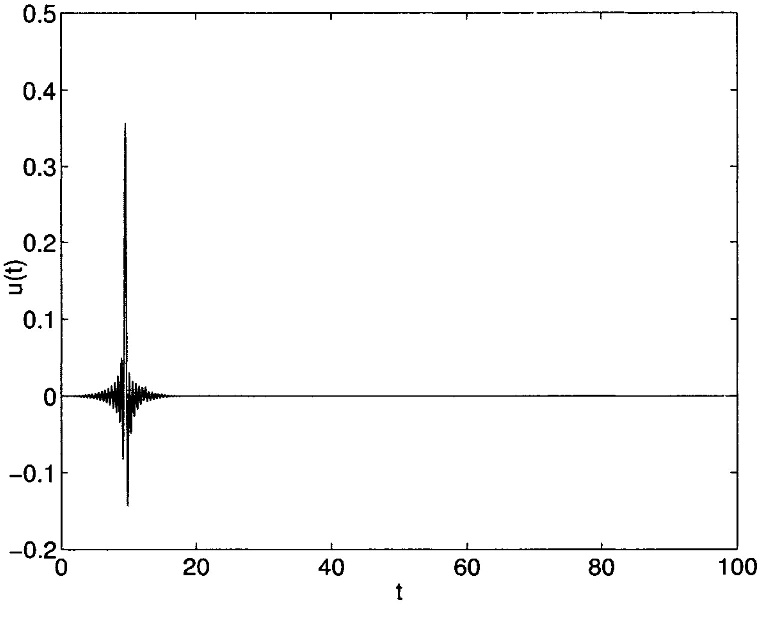

Fig. 24: Transient numerical solution $u(t)$ at $\mathbf{z}_s = (0.0514, 0.00814, 0.497)$ using Burton-Miller Formulation. The source function frequency is $\omega_0 = 4\pi$ and the coupling parameter is $a = 0.5$.

CHAPTER VI

APPLICATION OF THE EXACT GREEN'S FUNCTION IN SOUND PREDICTION

VI.1 SOUND GENERATED BY A VORTEX PASSING OVER A CIRCULAR CYLINDER

In most cases, exact solutions are not available for comparison with acoustic analogy calculations. Therefore, it is common practice to use experimental or simulated results to validate acoustic analogies. For this example, the predicted sound field from an acoustic analogy is compared with that of a direct time-domain finite difference solution for a vortex passing over a circular cylinder.

The continuity and momentum conservation equations in tensor form are

$$\frac{\partial \rho}{\partial t} + \frac{\partial \rho u_1}{\partial x_1} + \frac{\partial \rho u_2}{\partial x_2} = 0 \tag{93}$$

$$\frac{\partial \rho u_1}{\partial t} + \frac{\partial \rho u_1 u_1}{\partial x_1} + \frac{\partial \rho u_1 u_2}{\partial x_2} + \frac{\partial p}{\partial x_1} = 0 \tag{94}$$

$$\frac{\partial \rho u_2}{\partial t} + \frac{\partial \rho u_1 u_2}{\partial x_1} + \frac{\partial \rho u_2 u_2}{\partial x_2} + \frac{\partial p}{\partial x_2} = 0 \tag{95}$$

where effects of viscosity are ignored. Consider a perturbed flow

$$\rho = \bar{\rho} + \rho', \; u_1 = \bar{u}_1 + u_1', \; u_2 = \bar{u}_2 + u_2'$$

where the mean velocity field is given by the potential flow over a circular cylinder of radius 0.5 as

$$\bar{u}_1 = u_\infty \left(1 - \frac{r_0^2}{r^2}\cos(2\theta)\right), \;\; \bar{u}_2 = -u_\infty \frac{r_0^2}{r^2}\sin(2\theta) \tag{96}$$

where u_∞ is the far-field constant mean velocity in the x_1-direction. The perturbed flow is initialized with a vortex far away from the cylinder where the mean flow is approximately equal to u_∞. Hence, the initial conditions are given by

$$\rho' = 0, \; u_1' = (x_2 - 0.85)e^{-\ln(2)\left(\frac{(x_1+2.5)^2+(x_2-0.85)}{0.04}\right)}$$

$$u_2' = -(x_1 + 2.5)e^{-\ln(2)\left(\frac{(x_1+2.5)^2+(x_2-0.85)}{0.04}\right)} \tag{97}$$

VI.1.1 Direct Numerical Simulation Formulation

To obtain direct numerical simulation results, the perturbed flow is solved by linearized equations of (93)-(95) using a finite difference scheme. Assuming $p' = a_\infty^2 \rho'$, where a_∞ is the speed of sound, the linearized equations in perturbed variables are

$$\frac{\partial \rho'}{\partial t} + \bar{\rho}\frac{\partial u_1'}{\partial x_1} + \bar{\rho}\frac{\partial u_2'}{\partial x_2} + \frac{\partial \bar{\rho}}{\partial x_1}u_1' + \frac{\partial \bar{\rho}}{\partial x_2}u_2' + \bar{u}_1\frac{\partial \rho'}{\partial x_1} + \bar{u}_2\frac{\partial \rho'}{\partial x_2} + [\frac{\partial \bar{u}_1}{\partial x_1} + \frac{\partial \bar{u}_2}{\partial x_2}]\rho' = 0 \quad (98)$$

$$\frac{\partial u_1'}{\partial t} + \bar{u}_1\frac{\partial u_1'}{\partial x_1} + \bar{u}_2\frac{\partial u_1'}{\partial x_2} + \frac{\partial \bar{u}_1}{\partial x_1}u_1' + \frac{\partial \bar{u}_1}{\partial x_2}u_2' + \frac{1}{\bar{\rho}}[\bar{u}_1\frac{\partial \bar{u}_1}{\partial x_1} + \bar{u}_2\frac{\partial \bar{u}_1}{\partial x_2}]\rho' + \frac{a_\infty^2}{\bar{\rho}}\frac{\partial \rho'}{\partial x_1} = 0 \quad (99)$$

$$\frac{\partial u_2'}{\partial t} + \bar{u}_1\frac{\partial u_2'}{\partial x_1} + \bar{u}_2\frac{\partial u_2'}{\partial x_2} + \frac{\partial \bar{u}_2}{\partial x_1}u_1' + \frac{\partial \bar{u}_2}{\partial x_2}u_2' + \frac{1}{\bar{\rho}}[\bar{u}_1\frac{\partial \bar{u}_2}{\partial x_1} + \bar{u}_2\frac{\partial \bar{u}_2}{\partial x_2}]\rho' + \frac{a_\infty^2}{\bar{\rho}}\frac{\partial \rho'}{\partial x_2} = 0 \quad (100)$$

Fig. 25 shows the time-domain finite difference solution of the linearized Euler equations, (98)-(100). Initially, the vortex is in a translational motion without significant sound emission, as shown in 25 (a). As the vortex passes over the cylinder, a non-uniform mean flow field results, causing the generation of acoustic waves, shown in 25 (b)-(d). The streamlines of the non-uniform mean flow, given by equation (96), are illustrated in Fig. 26.

VI.1.2 Acoustic Analogy Formulation

To formulate the acoustic analogy equation with the convective effect of a far-field constant mean-flow included, equations (93)-(95) are rewritten as

$$\frac{\partial \rho}{\partial t} + u_\infty\frac{\partial \rho}{\partial x_1} + \frac{\partial \rho(u_1 - u_\infty)}{\partial x_1} + \frac{\partial \rho u_2}{\partial x_2} = 0 \quad (101)$$

$$\frac{\partial \rho u_1}{\partial t} + u_\infty\frac{\partial \rho u_1}{\partial x_1} + \frac{\partial \rho(u_1 - u_\infty)u_1}{\partial x_1} + \frac{\partial \rho u_1 u_2}{\partial x_2} + \frac{\partial p}{\partial x_1} = 0 \quad (102)$$

$$\frac{\partial \rho u_2}{\partial t} + u_\infty\frac{\partial \rho u_2}{\partial x_1} + \frac{\partial \rho(u_1 - u_\infty)u_2}{\partial x_1} + \frac{\partial \rho u_2 u_2}{\partial x_2} + \frac{\partial p}{\partial x_2} = 0 \quad (103)$$

By taking the operation $\left(\frac{\partial}{\partial t} + u_\infty\frac{\partial}{\partial x_1}\right)(101) - \frac{\partial}{\partial x_1}(102) - \frac{\partial}{\partial x_2}(103)$, the following acoustic analogy equation is obtained:

$$(\frac{\partial}{\partial t} + u_\infty\frac{\partial}{\partial x_1})^2\rho - a_\infty^2(\frac{\partial^2 \rho}{\partial x_1^2} + \frac{\partial^2 \rho}{\partial x_2^2}) = \frac{\partial^2 T_{11}}{\partial x_1^2} + 2\frac{\partial^2 T_{12}}{\partial x_1 \partial x_2} + \frac{\partial^2 T_{22}}{\partial x_2^2} \quad (104)$$

where

$$T_{11} = \rho(u_1 - u_\infty)(u_1 - u_\infty) + p - a_\infty^2\rho$$

$$T_{12} = \rho(u_1 - u_\infty)u_2$$

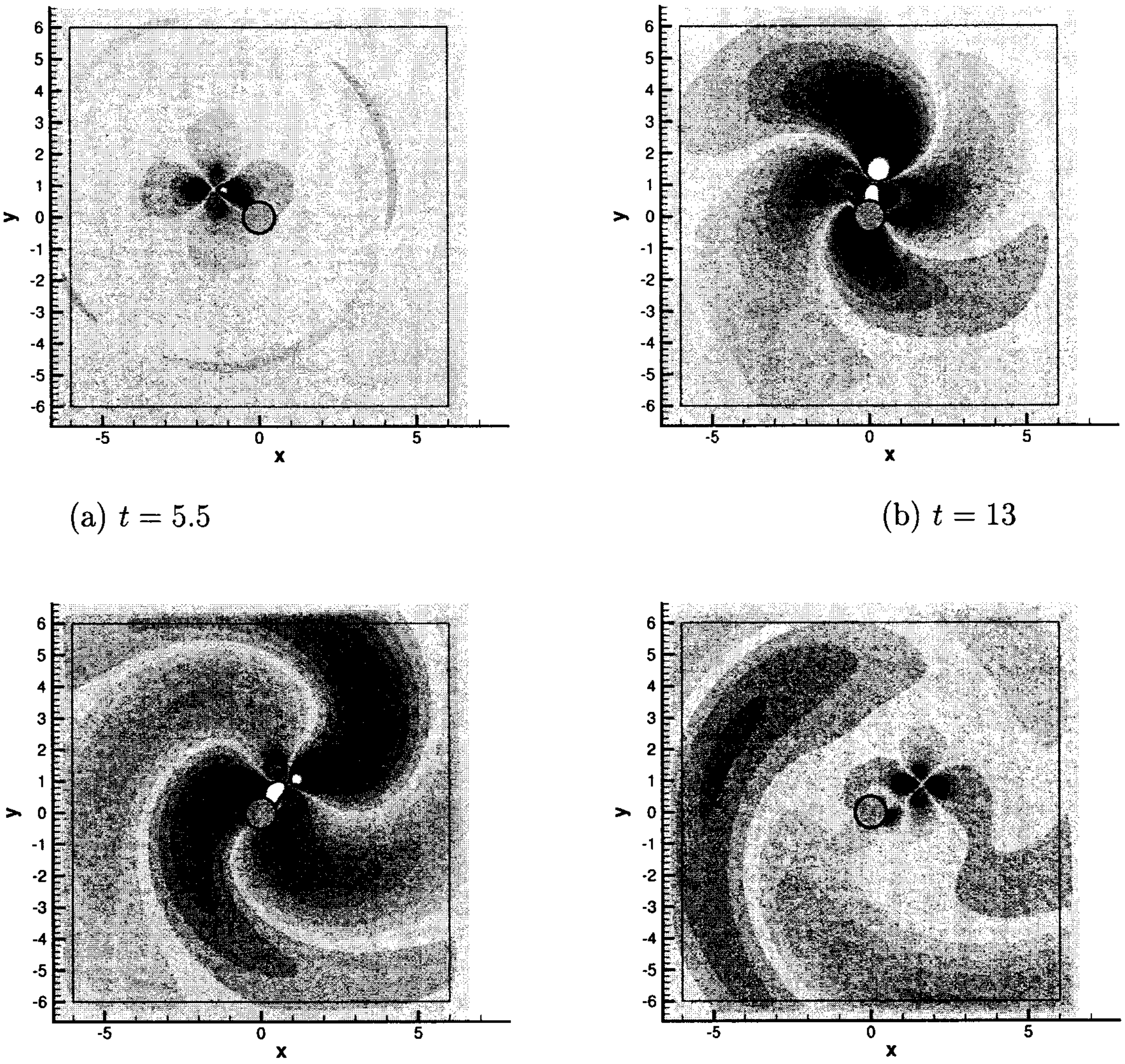

(a) $t = 5.5$

(b) $t = 13$

(c) $t = 16$

(d) $t = 20$

Fig. 25: Instantaneous density contours of the time-domain finite difference solution.

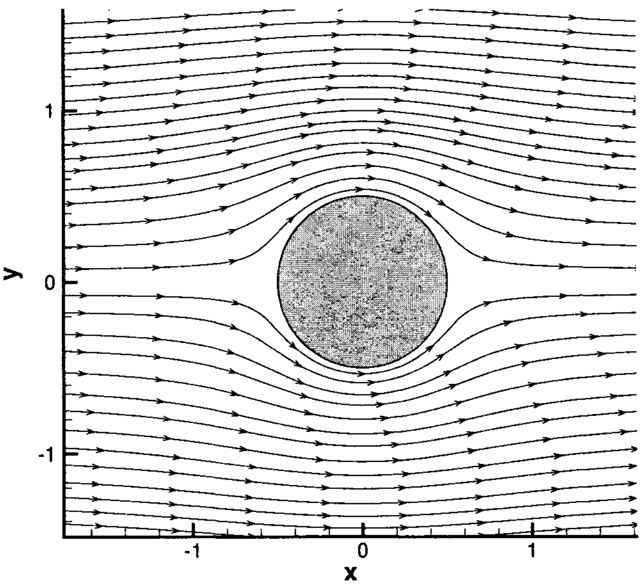

Fig. 26: Streamlines of the non-uniform flow.

$$T_{22} = \rho u_2 u_2 + p - a_\infty^2 \rho$$

The density perturbation satisfies the linearized acoustic analogy equation, given by

$$(\frac{\partial}{\partial t} + u_\infty \frac{\partial}{\partial x_1})^2 \rho' - a_\infty^2 (\frac{\partial^2 \rho'}{\partial x_1^2} + \frac{\partial^2 \rho'}{\partial x_2^2}) = \frac{\partial^2 T'_{11}}{\partial x_1^2} + 2\frac{\partial^2 T'_{12}}{\partial x_1 \partial x_2} + \frac{\partial T'_{22}}{\partial x_2^2} \tag{105}$$

which can be verified using equations (98)-(100). Here, T'_{11}, T'_{12}, and T'_{22} are the linearized stress tensors,

$$T'_{11} = 2\bar{\rho}(\bar{u}_1 - u_\infty)u'_1 + (\bar{u}_1 - u_\infty)(\bar{u}_1 - u_\infty)\rho'$$

$$T'_{12} = \bar{\rho}(\bar{u}_1 - u_\infty)u'_2 + \bar{\rho}\bar{u}_2 u'_1 + (\bar{u}_1 - u_\infty)\bar{u}_2 \rho'$$

$$T'_{22} = 2\bar{\rho}\bar{u}_2 u'_2 + \bar{u}_2 \bar{u}_2 \rho'$$

To find the far-field sound by acoustic analogy, equation (105) is solved in the frequency domain, giving

$$\rho'(\mathbf{y}, \omega) = \int_V T'_{ij}(\mathbf{x}, \omega) \frac{\partial^2 G_B(\mathbf{x}, \mathbf{y}, \omega)}{\partial x_i \partial x_j} dV \tag{106}$$

where $G_B(\mathbf{x}, \mathbf{y}, \omega)$ is the two-dimensional exact Green's function discussed in previous sections. In equation (106), $\mathbf{y}$ is the source (receiving) point and $\mathbf{x}$ represents a near-field point. The frequency domain stress tensors, $T'_{ij}(\mathbf{x},\omega)$, are obtained by the Fast Fourier Transform (FFT) of the time-domain simulation. One challenge in implementing equation (105) is determining the region of nonzero $T'_{ij}(\mathbf{x},\omega)$ and accurately specifying the stress tensor values within that region [43]. Fig. 27 illustrates the region around the cylinder where the $T'_{ij}(\mathbf{x},\omega)$ appear to make the most significant contribution, namely, $0.5 < r < 1.5$.

The volume integral in equation (106) was performed using 5100 near-field points, $\mathbf{x}$, located in the finite region $0.5 < r < 1.5$. Fig. 28 shows the density perturbation, $\rho'(\mathbf{y},\omega)$, versus frequency for two far-field points located at (A) $\mathbf{y} = (-6, 0)$ and (B) $\mathbf{y} = (0, -6)$ using both the acoustic analogy and direct numerical simulation. The order of the basis functions used to compute the exact Green's function is $P = 3$ and the Mach number is $M = 0.2$. In general, the acoustic analogy results for point (A) are consistent with the direct numerical simulation results. However, at point (B), the acoustic analogy results are not as accurate. In an attempt to improve the results for point (B), the region of integration was enlarged to $0.5 < r \leq 2.5$ and the number of near-field points used in the volume integral was 19,200. Improved results for both points (A) and (B) are shown in Fig. 29.

VI.2 SOUND GENERATED BY A TURBULENT FLOW OVER A CIRCULAR CYLINDER

For this example, the acoustic analogy formulation given by equation (104) is used to determine the acoustic radiation generated by a turbulent flow over a circular cylinder. With the use of the exact Green's function, the far-field acoustic solution for a density fluctuation, ρ', in the frequency domain can be expressed as

$$\rho'(\mathbf{y},\omega) = \int_V T_{ij}(\mathbf{x},\omega)\frac{\partial^2 \tilde{g}(\mathbf{x},\mathbf{y},\omega,s)}{\partial x_i \partial x_j} dV \tag{107}$$

where the T_{ij}'s represent the Lighthill Tensors defined in equation (104) with the density replaced by the mean density, ρ_0. The exact Green's function, $\tilde{g}(\mathbf{x},\mathbf{y},\omega,s)$, is formulated for a three-dimensional point source, but can be simplified to a single two-dimensional computation when the source point is located in the far-field, away from surface and unsteady flows [22]. To obtain the stress tensors in equation (107), a time dependent RANS (Reynolds Averaged Navier-Stokes) simulation is used through the CFL3D code developed at NASA Langley Research Center. The free stream Mach number is $M = 0.2$ and the Reynolds number based on the mean flow is $Re = 10,000$.

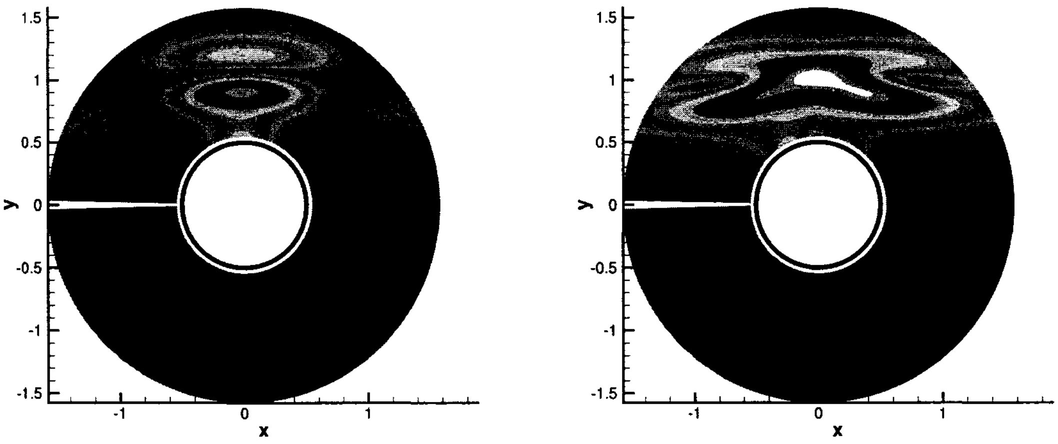

(a) T'_{11} (b) T'_{12}

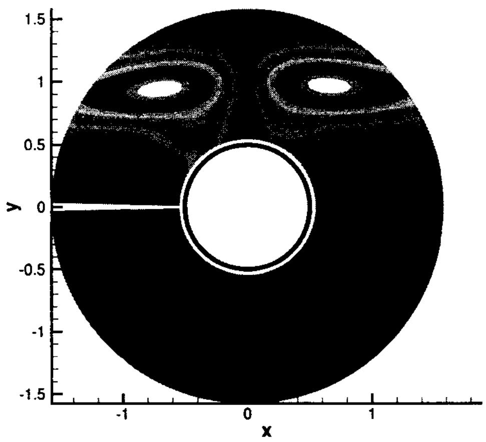

(c) T'_{22}

Fig. 27: Contours of the stress tensor T'_{ij} at frequency $\omega = 0.98$.

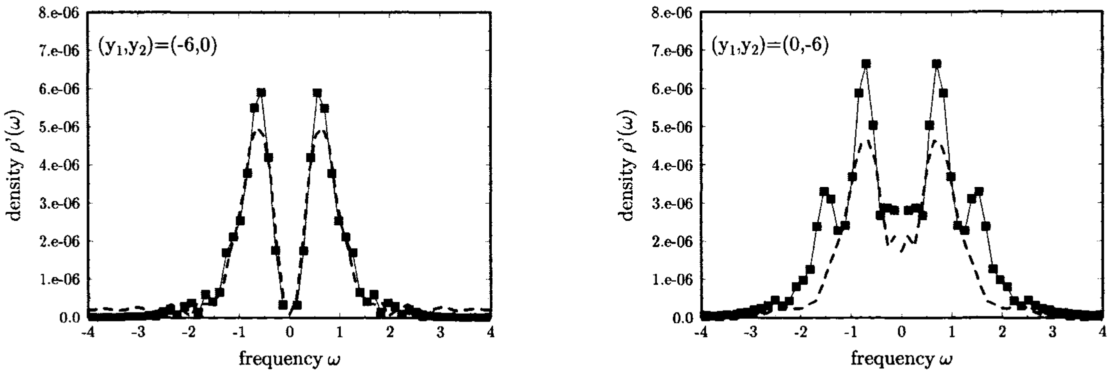

Fig. 28: Density, $\rho'(\omega)$, as a function of frequency, ω, at far-field points (A) $\mathbf{y} = (-6, 0)$ and (B) $\mathbf{y} = (0, -6)$. The number of near-field points used for volume integration is 5100 and the radius of integration is $0.5 < r < 1.5$. Squares: acoustic analogy results; dotted line: direct numerical simulation results.

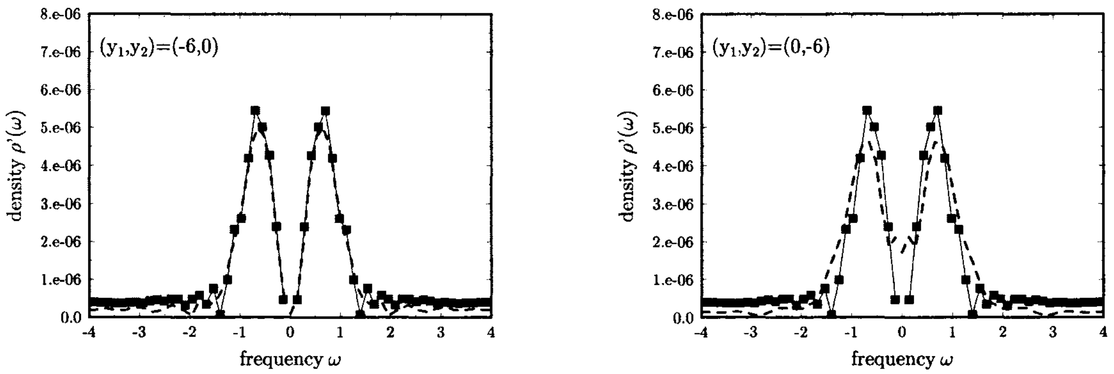

Fig. 29: Density, $\rho'(\omega)$, as a function of frequency, ω, at far-field points (A) $\mathbf{y} = (-6, 0)$ and (B) $\mathbf{y} = (0, -6)$. The number of near-field points used for volume integration is 19,200 and the radius of integration is $0.5 < r \leq 2.5$. Squares: acoustic analogy results; dotted line: direct numerical simulation results.

Fig. 30(a) shows the instantaneous flow streamlines generated by the turbulent flow passing over a circular cylinder of radius 0.5. Also shown in Fig. 30 are the contour maps of each maximum $T_{ij}(\mathbf{x}, \omega)$. The volume integral contained in equation (107) is carried out over a region of $0.51 \leq r \leq 2$ in order to cover the area of the most significant contributions by $T_{ij}(\mathbf{x}, \omega)$.

In Fig. 31, the density fluctuation spectrum is shown for 21 far-field points at a radius of $r = 20$. For each far-field point, the sound pressure was calculated at 135 frequencies ranging from zero to 2π, using 2816 near-field points clustered in the region of integration given above. Fig. 31 clearly illustrates the tonal variation caused by the vortex shedding due to the turbulent flow over the cylinder. The directivity of the acoustic radiation at the fundamental and first harmonic frequencies is given in Fig. 32. The fundamental frequency is at Strouhal number $St = 0.224$. The dashed line in the fundamental frequency plot represents a dipole. It is clear that the radiation pattern at the fundamental frequency closely resembles that of a dipole, which is the expected behavior according to Lighthill's theory [12, 28].

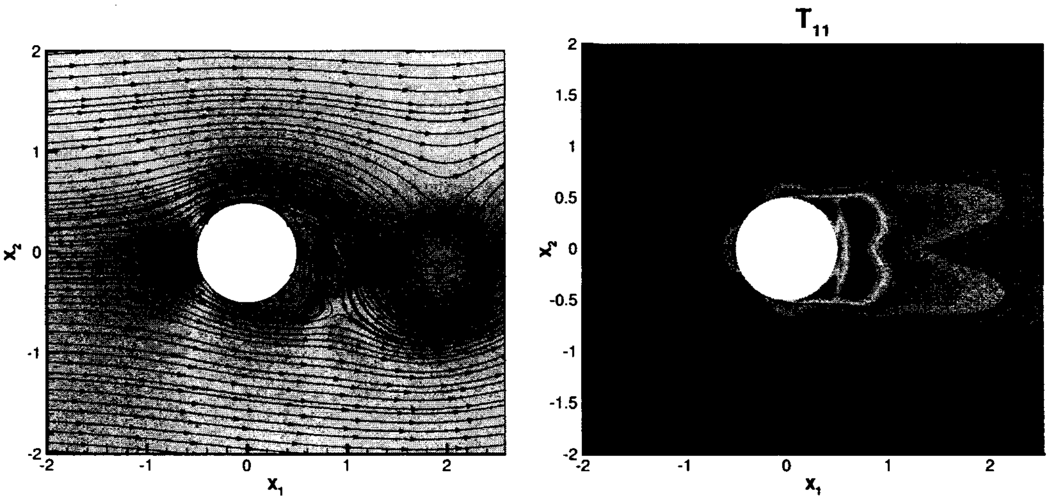

(a) Streamlines and density contours (b) T_{11}

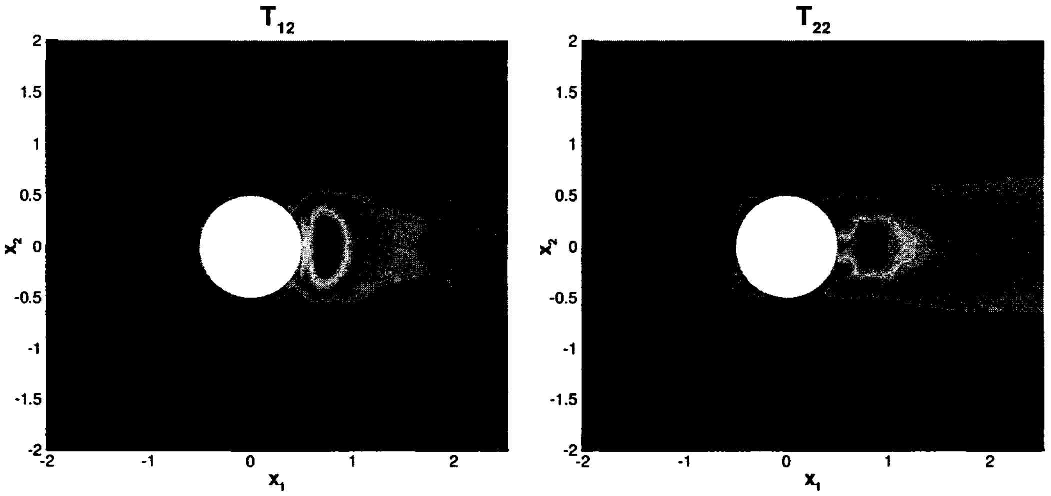

(c) T_{12} (d) T_{22}

Fig. 30: Contours of the maximum stress tensor, T_{ij}.

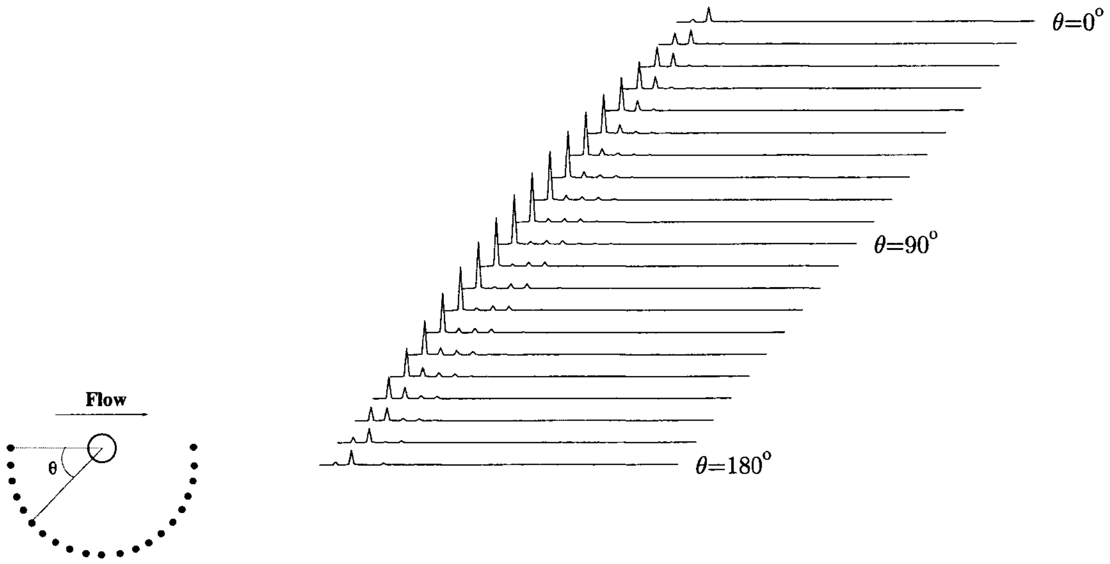

Fig. 31: Spectrum of density fluctuation at $r = 20$. Angle θ is measured from the forward direction.

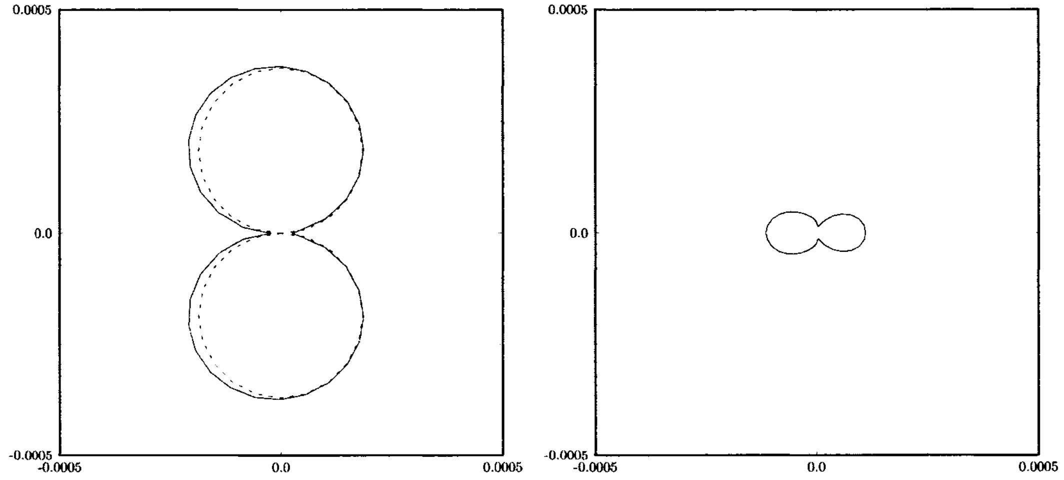

Fig. 32: Directivity of the far-field density at the fundamental frequency (left) and its harmonic frequency (right). The dotted line indicates the dipole directivity.

CHAPTER VII

CONCLUSIONS

Many current aircraft airframe noise prediction methods encounter difficulties when attempting to handle complex geometries. Hence, the main objective of this thesis was to develop and analyze a robust noise prediction method that could easily be applied to both smooth and non-smooth boundaries, resulting in acceptable relative errors. A spectral collocation boundary element method formulated in the frequency domain was first applied to smooth boundaries. The use of an exact Green's function satisfied the radiation condition at infinity as well as the wall boundary conditions on all solid surfaces. The spectral collocation method succeeded in achieving exponential convergence as the order of basis functions increased, when compared with the exact solution on a smooth, cylindrical body.

The spectral collocation BEM is advantageous because the order of the basis functions used to approximate the exact Green's function can be changed without reformulation of the problem. When computing the exact Green's function for a smooth boundary, the spectral collocation method gave accurate results for all basis function orders. However, the Green's function double divergence calculations at field points very close to the boundary were inaccurate for low basis function orders. For these close field points, higher order basis polynomials ($P \geq 5$) were needed to retain the desired accuracy. In order to further understand the benefits of using high-order basis functions, a Nodes per Wavelength calculation was performed. The results of this calculation showed that the number of nodes per wavelength required to attain a maximum allowable relative error decreased as the basis function order increased. The computation time for the calculation of the exact Green's function and one component of its double divergence also decreased until an "optimal" order was reached. None of the calculations resulted in an optimal order of less than $P = 3$. The Nodes per Wavelength calculation clearly shows the benefits of using the spectral collocation BEM with high-order basis functions.

When a field point is very close to the boundary, the second derivatives of the exact Green's function require the use of high-order basis functions. This is due to the nearly singular integral kernels in the double divergence equation, which is calculated by direct differentiation. In an attempt to improve the accuracy of the double divergence when using lower order basis functions, a comparative study was done between direct differentiation and several finite difference approximations. The relative errors corresponding to the finite difference calculations were on the same order of magnitude as the direct differentiation errors. Since the finite difference approximations did not significantly improve results, direct differentiation of the exact Green's function is preferred for all field points.

The application of the spectral collocation method to smooth boundaries results in exponential convergence. However, Chebyshev polynomials cannot adequately approximate the exact Green's function on corner elements due to the nature of the singularities at the corners. Therefore, the spectral collocation BEM applied to a non-smooth boundary using Chebyshev polynomials did not result in exponential convergence when the basis function order was increased. To improve these results, an exponential grading element refinement was introduced. Exponential convergence was obtained with proper refinement. The effects of changing the refinement ratio and level of refinement were studied, and it was shown that as the refinement ratio decreased, the level of refinement necessary for a desired accuracy also decreased. However, if the length of the refined corner element was too small, large errors resulted for low levels of refinement. Hence, the recommended refinement strategy is to use a small refinement ratio while making sure that the level of refinement is not too small. Refinement ratios between $\nu = 0.2$ and $\nu = 0.35$ gave the best results for the non-smooth boundaries discussed in this thesis. Next, the collocation method was reformulated using a Sinc function expansion on the corner elements. Although the Sinc function collocation method improved results over Chebyshev polynomials without element refinement, exponential convergence was not achieved. Both the element refinement method and the Sinc collocation method are robust methods for dealing with complex geometries. The element refinement method using Chebyshev polynomials gives a more accurate solution with fewer unknowns. Therefore, exponential grading element refinement is the preferred method for reducing errors caused by solution singularities at a corner.

A three-dimensional time-domain spectral collocation boundary element method was formulated in order to obtain exact Green's functions at all frequencies in a single computation. Triangular boundary elements were chosen for their ability to accommodate boundaries of any shape. Kernel singularities were dealt with via a polar coordinate transformation. The results of the time-domain BEM were in good agreement with the exact solution for $\omega_0 = 2\pi$ and $\omega_0 = 4\pi$. The March-On-Time scheme associated with the time-domain BEM resulted in solution instabilities, which occurred more rapidly at higher source function frequencies. In order to overcome this problem, the time-domain BEM was reformulated using a Burton-Miller Combined Field Integral Equation. Hypersingular integrals appearing in the Burton-Miller formulation were regularized and included in the time marching scheme. The results of the time-domain BEM using the Burton-Miller formulation did not exhibit any long-time instabilities.

Two examples of application were done to validate the acoustic analogy involving the exact Green's function in the frequency domain. The first example compared acoustic analogy results to direct numerical simulation results for a vortex passing over a circular cylinder. When the appropriate region of integration and number of field points were used, the acoustic analogy results were in good agreement with the simulated results. In the second example, the acoustic analogy was used to predict the sound generated by a turbulent flow over a circular cylinder. The directivity of the acoustic radiation at the fundamental frequency closely resembled a dipole. This behavior coincides with the predicted behavior according to Lighthill's theory. The results of both examples validate the acoustic analogy and show that the spectral collocation BEM is a successful method for computing exact Green's functions.

REFERENCES

[1] Abramowitz M, Stegun IA. Handbook of mathematical functions. New York: Dover; 1965.

[2] Agarwal A, Morris PJ. Broadband noise from the unsteady flow in a slat cove. AIAA paper 2004-0854, 2004.

[3] Amiet RK. Noise due to turbulent flow past a trailing edge. J Sound Vib 1976;47(3):387-393.

[4] Amiet RK. A note on edge noise theories. J Sound Vib 1981;78(4):485-488.

[5] Asvestas JS. Electromagnetic and acoustic scattering by simple shapes. In: Bowman JJ, Senior TBA, Uslenghi PLE, editors. The circular cylinder. Amsterdam: North-Holland Pub Co, 1969.

[6] Blyth MG, Pozrikidis C. A Lobatto interpolation grid over the triangle. IMA J Appl Math 2006;71:153-169.

[7] Boyd JP. Chebyshev and fourier spectral methods. 2nd ed. New York: Dover; 2000.

[8] Boyd JP. A Chebyshev/rational Chebyshev spectral method for the Helmholtz equation in a sector on the surface of a sphere: defeating corner singularities. J Comp Phys 2005;206(1):302-310.

[9] Burton AJ, Miller GF. The application of integral equation methods to the numerical solution of some exterior boundary-value problems. Proc R Soc Lond A 1971;323:201-210.

[10] Chappell DJ, Harris PJ, Henwood D, Chakrabarti R. A stable boundary element method for modeling transient acoustic radiation. J Acoust Soc Am 2006;120(1):74-80.

[11] Cheng AHD, Cheng DT. Heritage and early history of the boundary element method. Eng Anal Bound Elem 2005;29:268-302.

[12] Crighton DG. Basic principles of aerodynamic noise generation. Prog Aero Sci 1975;16(1):31-96.

[13] de Lacerda LA, Wrobel LC, Mansur WJ. A boundary integral formulation for two-dimensional acoustic radiation in a subsonic uniform flow. J Acoust Soc Am 1996;100(1):98-107.

[14] do Rego Silva JJ. Acoustic and elastic wave scattering using boundary elements. In: Brebbia CA, Connor JJ, editors. Topics in Engineering Vol. 18. Southampton, UK: Computational Mechanics Publications; 1994.

[15] Dowling AP, Ffowcs Williams JE. Sound and sources of sound. Westergate: Horwood Publishing; 1983.

[16] Ergin AA, Balasubramaniam S, Michielssen E. Analysis of transient wave scattering from rigid bodies using a Burton-Miller approach. J Acoust Soc Am 1999;106(5):2396-2404.

[17] Ergin AA, Balasubramaniam S, Michielssen E. Fast transient analysis of acoustic wave scattering from rigid bodies using a two-level plane wave time domain algorithm. J Acoust Soc Am 1999;106(5):2405-2416.

[18] Farassat F, Casper JH. Towards an airframe noise prediction methodology: survey of current approaches. AIAA paper 2006-210, 2006.

[19] Guo YP. Application of the Ffowcs Williams/Hawkings equation to two-dimensional problems. J Fluid Mech 2000;403:201-221.

[20] Howe MS. A review of theory of trailing edge noise. J Sound Vib 1978;61:437-465.

[21] Hu FQ. A spectral boundary integral equation method for the 2D Helmholtz equation. J Comp Phys 1995;120:340-347.

[22] Hu FQ, Guo YP, Jones AD. On the computation and application of exact Green's function in acoustic analogy. AIAA Paper 2005-2986, 2005.

[23] Hwang WS. Hypersingular boundary integral equations for exterior acoustic problems. J Acoust Soc Am 1997;101(6):3336-3342.

[24] Igarashi H, Honma T. A boundary element method for potential fields with corner singularities. Appl Math Model 1996;20:847-852.

[25] Juhl P. A note on the convergence of the direct collocation boundary element method. J Sound Vib 1998;212(4):703-719.

[26] Khorrami MR, Choudhari M, Singer BA, Lockard DP, Streett CL. In search of the physics: The interplay of experiment and computation in slat aeroacoustics. AIAA paper 2003-0980, 2003.

[27] Kirkup S. BEMHELM: BEM for Helmholtz problems. http://www.boundary-element-method.com/helmholtz/index.htm; 2004.

[28] Lighthill MJ. On sound generated aerodynamically I. General theory. Proc R Soc London Ser 1952;A 221:564-587.

[29] Liu GR, Cai C, Zhao J, Zheng H, Lam KY. A study on avoiding hyper-singular integrals in exterior acoustic radiation analysis. Appl Acoust 2002;63:643-657.

[30] Lockard DP. An efficient, two-dimensional implementation of the Ffowcs Williams and Hawkings equation. J Sound Vib 2000;229(4):897-911.

[31] Marin L, Lesnic D, Mantic V. Treatment of singularities in Helmholtz-type equations using the boundary element method. J Sound Vib 2004;278(1-2):39-62.

[32] Narasimhan S, Majdalani J, Stenger F. A first step in applying the sinc collocation method to the nonlinear Navier-Stokes equations. Num Heat Trans Part B 2002;41:447-462.

[33] Ong ET, Lim KM. Three-dimensional singular boundary elements for corner and edge singularities in potential problems. Eng Anal Bound Elem 2005;29:175-189.

[34] Power H, Wrobel LC. Boundary integral methods in fluid mechanics. Southampton, UK: Computational Mechanics Publications; 1995.

[35] Pozrikidis C. A practical guide to boundary element methods with the software library BEMLIB. Boca Raton, FL: Chapman & Hall/CRC; 2002.

[36] Pozrikidis C. A spectral collocation method with triangular boundary elements. Eng Anal Bound Elem 2006;30:315-324.

[37] Saadatmandi A, Razzaghi M, Dehghan M. Sinc-collcation methods for the solution of Hallen's integral equation. J Electromagn 2005;19(2):245-256.

[38] Stakgold I. Boundary value problems of mathematical physics. Vol II. Philadelphia: SIAM, 2000.

[39] Stenger F. Numerical methods based on Whittaker cardinal, or sinc functions. SIAM Review 1981;23(2):165-224.

[40] Strang G, Fix G. An analysis of the finite element method. Englewood Cliffs, NJ: Prentice-Hall, Inc., 1973.

[41] Telukunta S, Mukherjee S. An extended boundary node method for modeling normal derivative discontinuities in potential theory across edges and corners. Eng Anal Bound Elem 2004;28:1099-1110.

[42] Wang J, Tsay T. Analytical evaluation and application of the singularities in boundary element method. Eng Anal Bound Elem 2005;29:241-256.

[43] Wells VL, Renaut RA. Computing aerodynamically generated noise. Annu Rev Fluid Mech 1997;29:161-199.

[44] Wu TW, Seybert AF, Wan GC. On the numerical implementation of a Cauchy principal value integral to insure a unique solution for acoustic radiation and scattering. J Acoust Soc Am 1991;90(1):554-560.

[45] Wu TW, Lee L. A direct boundary integral formulation for acoustic radiation in a subsonic uniform flow. J Sound Vib 1994;175(1):51-63.

APPENDIX A

PROPERTIES OF HANKEL FUNCTIONS

A.1 DEFINITION

The nth order Hankel function of the first kind is defined as

$$H_n^{(1)}(x) = J_n(x) + iY_n(x)$$

where $J_n(x)$ and $Y_n(x)$ are nth order Bessel functions of the first and second kind, respectively.

A.2 ASYMPTOTIC EXPANSIONS

For sufficiently small x, the asymptotic series of the zeroth order Bessel functions are

$$J_0(x) = 1 - \frac{x^2}{4} + \frac{x^4}{64} - \ldots$$

and

$$Y_0(x) = \frac{2}{\pi} \ln\left(\frac{x}{2}\right) J_0(x) + \frac{2\gamma}{\pi} J_0(x) + \frac{x^2}{2\pi} - \ldots$$

where γ is a fixed constant. Therefore, the asymptotic series of the zeroth order Hankel function of the first kind is

$$H_0^{(1)}(x) = \frac{2i}{\pi} \ln(x) J_0(x) + \text{ smooth terms}$$

A.3 DERIVATIVES OF HANKEL FUNCTIONS

The derivative of an nth order Hankel function of the first kind is defined as

$$\frac{d}{dx} H_n^{(1)}(x) = \frac{1}{2}\left[H_{n-1}^{(1)}(x) - H_{n+1}^{(1)}(x)\right]$$

Using the above definition with the property

$$H_{-n}^{(1)}(x) = -H_n^{(1)}(x)$$

gives

$$\frac{d}{dx} H_0^{(1)}(x) = \frac{1}{2}\left[H_{-1}^{(1)}(x) - H_1^{(1)}(x)\right] = -H_1^{(1)}(x)$$

APPENDIX B

BASIS FUNCTIONS

B.1 CHEBYSHEV POLYNOMIALS

The basis functions are

$$\phi_n(\bar{t}) = T_n(2\bar{t} - 1)$$

where $T_n(\bar{\xi})$ are the Chebyshev polynomials defined by

$$T_n(\bar{\xi}) = \cos\left(n \arccos \bar{\xi}\right)$$

The Gauss-Chebyshev collocation points are

$$\bar{t}_\ell = \frac{\bar{\xi}_\ell + 1}{2}, \bar{\xi}_\ell = \cos\left(\frac{2\ell + 1}{2P + 2}\pi\right), \quad \ell = 0, 1, 2, ..., P$$

B.2 SINC FUNCTION POLYNOMIALS

The basis functions are

$$Sn_m(\bar{t}) = \frac{\sin\left[\left(\frac{\pi}{h}\right)\left(\zeta(\bar{t}) - (m - P)h\right)\right]}{\left(\frac{\pi}{h}\right)\left(\zeta(\bar{t}) - (m - P)h\right)}, \quad m = 0, ..., 2P$$

where

$$\zeta(\bar{t}) = \log\left(\frac{\bar{t}}{1 - \bar{t}}\right)$$

The Sinc collocation points are

$$\bar{t}_k = \frac{e^{kh}}{1 + e^{kh}}, \quad k = -P, ..., P$$

For both the basis functions and collocation points,

$$h = \frac{\pi}{\sqrt{P}}$$

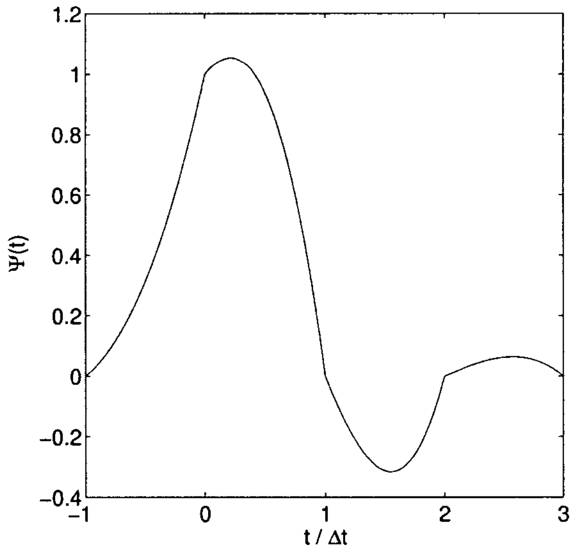

Fig. 33: Temporal Basis Function $\Psi(t)$.

B.3 PRORIOL POLYNOMIALS

The Proriol polynomials are

$$P_{k\ell} = L_k(\xi')(1-\eta)^k J_\ell^{(2k+1,0)}(\eta')$$

where

$$\xi' = \frac{2\xi}{1-\eta} - 1, \qquad \eta' = 2\eta - 1,$$

L_k are the Legendre polynomials and $J_\ell^{(2k+1,0)}$ are the Jacobi polynomials.

B.4 TEMPORAL BASIS FUNCTIONS

The basis functions are

$$\Psi(t) = \begin{cases} 1 + \frac{11}{6}(\frac{t}{\Delta t}) + (\frac{t}{\Delta t})^2 + \frac{1}{6}(\frac{t}{\Delta t})^3 & \text{for } -\Delta t \le t \le 0 \\ 1 + \frac{1}{2}(\frac{t}{\Delta t}) - (\frac{t}{\Delta t})^2 - \frac{1}{2}(\frac{t}{\Delta t})^3 & \text{for } 0 < t \le \Delta t \\ 1 - \frac{1}{2}(\frac{t}{\Delta t}) - (\frac{t}{\Delta t})^2 + \frac{1}{2}(\frac{t}{\Delta t})^3 & \text{for } \Delta t < t \le 2\Delta t \\ 1 - \frac{11}{6}(\frac{t}{\Delta t}) + (\frac{t}{\Delta t})^2 - \frac{1}{6}(\frac{t}{\Delta t})^3 & \text{for } 2\Delta t < t \le 3\Delta t \\ 0 & \text{elsewhere} \end{cases}$$

APPENDIX C

TIME-DOMAIN SOURCE FUNCTION

Consider the Fourier transform in time

$$\widehat{q}(\omega) = \frac{1}{2\pi}\int_{-\infty}^{\infty} q(t)e^{i\omega t}dt$$

with inverse

$$q(t) = \int_{-\infty}^{\infty} \widehat{q}(\omega)\, e^{-i\omega t}d\omega$$

Let

$$\widehat{q}(\omega) = \begin{cases} 1 & |\omega| \leq \omega_0 \\ 0.5 + 0.5\cos\left(\frac{\omega-\omega_0}{2h}\pi\right) & \omega_0 \leq \omega \leq \omega_0 + 2h \\ 0.5 + 0.5\cos\left(\frac{\omega+\omega_0}{2h}\pi\right) & -\omega_0 - 2h \leq \omega \leq -\omega_0 \end{cases}$$

Then,

$$q(t) = \frac{2\pi^2}{t\left(\pi^2 - 4h^2t^2\right)}\sin\left(\omega_0 t + ht\right)\cos(ht)$$

VITA

Andrea D. Jones
Department of COMPUTATIONAL AND APPLIED MATHEMATICS
Old Dominion University
Norfolk, VA 23529

Education

- Ph.D. Computational and Applied Mathematics, Old Dominion University, 2007
- M.S. Computational and Applied Mathematics, Old Dominion University, 2006
- B.S. Chemical Engineering, Virginia Polytechnic Institute & State University, 1996

Presentations and Publications

- **A.D. Jones** and F.Q. Hu, "A three-dimensional time-domain boundary element method for the computation of exact Green's functions in acoustic analogy", AIAA-2007-3479. Will be presented at 13th AIAA/CEAS Aeroacoustics Conference, Rome, Italy, May 2007.
- **A.D. Jones** and F.Q. Hu, "An investigation of spectral collocation boundary element method for the computation of exact Green's functions in acoustic analogy", AIAA-2006-2636. Presented at 12th AIAA/CEAS Aeroacoustics Conference, Cambridge, Massachusetts, May 2006.
- F.Q. Hu and **A.D. Jones**, "On the computation and application of exact Green's functions in acoustic analogy", AIAA-2005-2986.

Honors and Activities

- ODU College of Sciences Dissertation Fellowship, 2006-2007.
- Secretary of ODU Math & Stat Club, 2005-2006.

Typeset using LaTeX.